UNIVERSITY OF SOUTHAMPTON

Physics Beyond the Standard Model: Moduli Stabilisation and Neutrino Physics

by

Salima Boudjemaa

A thesis submitted in partial fulfillment for the
degree of Doctor of Philosophy

in the
Faculty of Engineering, Science and Mathematics
School of Physics and Astronomy

November 2009

UNIVERSITY OF SOUTHAMPTON

ABSTRACT

FACULTY OF ENGINEERING, SCIENCE AND MATHEMATICS
SCHOOL OF PHYSICS AND ASTRONOMY

Doctor of Philosophy

by Salima Boudjemaa

We look at models of neutrino mass and mixing which represent an important aspect of physics beyond the Standard Model (SM). We derive approximate analytic formulae for the neutrino mixing angles in general SD involving NLO and NNLO corrections. These expressions, which are given in terms of input see-saw parameters, provide a useful guide for unified model building. We then evaluate these formulae in the cases of CSD and PCSD for two numerical GUT inspired models in order to measure the effect of NLO and NNLO corrections. In addition to this, we analyse the effects of charged lepton corrections and Renormalisation Group (RG) running on neutrino mixing angles and various sum rules, in models where tri-bimaximal mixing is exactly achieved at high energy scale. We find the RG corrections to neutrino sum rules to be typically small for the case of hierarchical neutrinos.

Another aspect of physics beyond the Standard Model concerns the search for viable four dimensional string models. We look at moduli stabilisation in the framework of four dimensional models arising from heterotic and type IIA string theories. The superpotentials in these models involve flux and non-perturbative terms. We consider a set of conditions which lead to moduli solutions for Minkowski minima of the scalar potential. Following this procedure, we correct models presented in the literature and uplift the flat directions. We also study inflation in the framework of these models. We find that it is successfully achieved along the axionic directions of the moduli fields for values of the initial conditions within substantial regions of parameter space. A very interesting structure of the potential is obtained when considering the evolution of two axionic directions in one of the models in the presence of a gaugino condensate term. This structure, which involves the existence of multiple local minima surrounding the global one, represents a perfect background for realising inflation.

Contents

List of Figures

List of Tables

Preface

The work described in this thesis was carried out in collaboration with Dr. Stefan Antusch and my supervisors Prof. Steve King and Dr. Beatriz de Carlos.

- Parts of Chapter 2 and Chapter 4 contain original work which appears in the following reference:

  S. Boudjemaa and S. F. King, Phys. Rev. D 79 2009, 033001, [arXiv:0808.2782 [hep-ph]].

- Chapter 3, with the exception of the background sections, contains original results which appear in the following paper:

  S. Antusch, S. Boudjemaa and S. F. King, "Neutrino Mixing Angles in Sequential Dominance to NLO and NNLO."

- Parts of Chapter 6 and Chapter 7, excluding the background sections, contain original work which will soon appear in publication.

No claims to originality are made for the remaining chapters. These were compiled using a variety of other sources.

Acknowledgements

Firstly, I would like to thank my supervisors Prof. Steve King and Dr. Beatriz de Carlos for their advice, encouragement and patience. I would also like to thank Dr. Stefan Antusch for his help and the University of Southampton for providing a comfortable environment to work in.

My gratitude naturally extends to members of the High Energy Physics group, particularly to Ed Threlfall, Richard Howl and George Weatherill for their help and mostly for making the whole experience interesting and stimulating. I would also like to thank the Algerian Ministry of Higher Education and Scientific Research for their financial support.

Finally, I am grateful to my wonderful husband Issam, for his love and support throughout this work. Most of all, I would like to thank my parents for their love, help and encouragement.

Dedicated to my parents, Issam, and the rest of my family.

Chapter 1

General Introduction

1.1 Motivation

The Standard Model (SM) of particle physics is one of the most successful theories of the last century. However, although its predictions have been confirmed by experimental data, it falls short of being a complete theory of all the fundamental interactions observed in nature. One of the problems that the SM suffers from is the fact that it predicts massless neutrinos which is in disagreement with the most recent experimental results.

Evidence for neutrino mass and neutrino flavour oscillation came from various experimental data from solar, atmospheric and reactor experiments. The first one was the Raymond Davis experiment which detected a deficit in the number of electron neutrinos emitted by the sun [1]. This result suggested that electron neutrinos were changing to other flavours such as muon or tau neutrinos. The compelling evidence for neutrino oscillation came from The Super-Kamiokande experiment where a deficit in the muon neutrino flux, reaching the Earth, was observed [2]. Other experiments such as Sudbury Neutrino Observatory (SNO), KamLAND, K2K and MINOS have all confirmed the results of neutrino oscillation [3, 4].

Neutrino flavour oscillation generally means that one type of neutrino can be converted over time to a different type. For example, an electron neutrino turning into a muon neutrino or a muon neutrino oscillating to a tau neutrino. The mixing between the different neutrino flavours is controlled by the lepton mixing matrix, U, which relates the neutrino flavour states ν_e, ν_μ, ν_τ to the neutrino mass states

ν_1, ν_2, ν_3 with masses m_1, m_2, m_3. This great discovery of neutrino oscillation led to an increase, not only in the amount of experimental data, but also in the interest in neutrino phenomenology research.

The existence of neutrino mass requires us to look for possible extensions of the SM in order to provide a description that fits with experimental observations. Studying models of neutrino mass and mixing opens an important window in the search of possible theories of physics beyond the SM. One of the main neutrino mixing patterns that fits with current experimental data is the so called tri-bimaximal (TB) mixing [5, 6] described by the following matrix,

$$U_{TB} \approx \begin{pmatrix} \sqrt{\frac{2}{3}} & \frac{1}{\sqrt{3}} & 0 \\ -\frac{1}{\sqrt{6}} & \frac{1}{\sqrt{3}} & \frac{1}{\sqrt{2}} \\ \frac{1}{\sqrt{6}} & -\frac{1}{\sqrt{3}} & \frac{1}{\sqrt{2}} \end{pmatrix}. \tag{1.1}$$

TB mixing predicts maximal mixing for both the atmospheric, θ_{23}, and the solar, θ_{12}, angles while it assumes the reactor angle θ_{13} to be zero. There are many models that attempt to reproduce this as a theoretical prediction [7, 8, 9, 10, 11]. One way to achieve this type of mixing is by considering Constrained Sequential Dominance (CSD).

Part I of this thesis is concerned with deriving analytic formulae for the neutrino mixing angles in the presence of NLO and NNLO terms. We also study numerical estimates of the effects of these NLO and NNLO corrections on the mixing parameters using two GUT inspired models. In addition, we look at the model of Tri-bimaximal-Reactor Mixing (TBR) which predicts a non zero reactor angle while preserving TB solar mixing and maximal atmospheric mixing. The theoretical prediction of large reactor angle is in agreement with the most recent experimental data [12].

Although TB mixing can be achieved accurately in the neutrino sector, it usually exhibits deviations in the flavour basis when considering models arising from Grand Unified Theories (GUTs). One source of these deviations is the presence of charged lepton corrections. This gives rise to a variety of sum rules relating neutrino mixing parameters together; for example, $\theta_{12} - \theta_{13}\cos\delta \approx 35.26^o$. These sum rules represent an important tool not only for testing predictions of different neutrino mixing models but also for comparing these predictions to future high precision experiments.

Another source of deviations is Renormalisation Group (RG) running of neutrino quantities (including mixing angles, phases and masses) from high energy scale (the GUT scale) to the electroweak scale (M_Z scale). We expect future neutrino experiments to be more sensitive to deviations from TB mixing compared to the current situation. Therefore, it is of great importance to theoretically measure the uncertainty in these deviations. This represents one of the main motivations for Part I of this thesis where we study a set of neutrino sum rules at both high energy and M_Z scales. We also provide the first numerical study of TB deviations arising from both charged lepton corrections and RG running.

The quest for finding a unified theory of all interactions also suggests looking at physics beyond the SM. Such a theory would relate the forces of the SM: the strong force, the weak force and the electromagnetic force to gravity. Many extensions of the SM were proposed by physicists in order to incorporate other theories such as Supersymmetry. Perhaps the simplest one is the Minimal Supersymmetric Standard Model (MSSM). The pursuit of unifying the SM with gravity, however, takes us to ten and eleven dimensions where string and M-theory exist. Since these theories exist in far more dimensions than what is observed in our universe, we need to find a way of hiding the extra dimensions in order to compare the resulting physics to that of the SM. This mechanism is known as compactification.

Compactification is achieved when the extra dimensions are curled up to a very small radius (smaller than what we can observe by today's experiments). For the case of string theory, we have six extra space dimensions that can all be compactified. However in doing so, we get a four dimensional theory with undesirable side effects. These are massless scalar fields (moduli fields) that are not observed in nature and therefore would modify our laws of physics if left massless. Generating a potential for these fields and stabilising them at their Vacuum Expectation Values (Vevs) is extremely vital in order to have phenomenologically viable models. This is the main subject of Part II of this thesis, where we analyse some models from the literature, using a set of conditions including Supersymmetry breaking constraints. We also present new solutions for these models and uplift the flat directions. Stabilising moduli fields is also important for studying inflation since, without stabilisation, a particular modulus direction becomes flat and therefore can evolve forever leading to many problems such as decompactification of space dimensions. This represents another important motivation for studying moduli stabilisation as it would shed some light on the origin of structure formation and help us better understand the history of our universe.

Inflation, which is the dominant theory for the origin of structure, describes a period of exponential expansion which is introduced prior to the standard Big Bang theory. It is driven by the fluctuation of one or more scalar fields known as the inflaton fields. Inflation not only provides solutions for the classical problems of the Big Bang model including the flatness, horizon and monopole problems, but it also provides a natural explanation for the spectrum of density perturbation. During the inflationary period, small inhomogeneities in the energy density occur due to quantum fluctuations which generate temperature anisotropies in the cosmic microwave background radiation (CMB). These inhomogeneities were predicted in the literature [13, 14] and are in excellent agreement with recent observational data from the Wilkinson Microwave Anisotropy Probe (WMAP) [15]. WMAP data presents many constraints on inflation and its parameters in order to allow scientists to select between the different inflationary models. The WMAP also provides maps of the temperature fluctuations of the CMB radiation with very high accuracy and therefore it offers an opportunity to shed light on some of the key questions in cosmology and better understand the large structure of our universe.

In part II of this thesis, we aim to study inflation within the framework of models originating from string theory. There were many problems facing the implementation of inflationary models within string theory including the runaway moduli problem and also flat directions. With the development of flux compactification and moduli stabilisation, this field is undergoing promising progress. In this thesis, we present successful inflationary scenarios, achieved for realistic models of type IIA and heterotic theories. We also comment on a special structure obtained for models of type IIA string theories in the presence of gaugino condensation. These models give rise to unbounded potentials which constitute a prefect environment for realising eternal inflation.

1.2 Thesis structure

This thesis is divided into two parts. Part I is concerned with studying neutrino masses and mixing while Part II covers mainly the subjects of moduli stabilisation and cosmological inflation in the framework of string theory.

The first part is organised as follows. In Chapter 2, we give a brief overview of the nature of neutrinos and the history behind the discovery of neutrino mass. We then outline the different types of neutrino mass which leads us to an elegant

mechanism for explaining the smallness of neutrino masses, known as the see-saw mechanism. Finally, we review neutrino mixing including TB mixing and charged lepton corrections and present the derivation of a variety of neutrino sum rules.

Chapter 3 aims to review SD with the special case of CSD, which is a very powerful tool for obtaining TB mixing. We first discuss the diagonalisation procedure of the effective left-handed mass matrix resulting from the see-saw mechanism. We then use this approach to derive analytic expressions of the mixing angles in the presence of NLO and NNLO corrections. We conclude the chapter by evaluating these analytic formulae using two numerical examples in the simplified case of CSD, as well as PCSD involving non-zero 1-1 Yukawa coupling.

Chapter 4, which is the final chapter in Part I, involves studying neutrino mixing angles and a set of sum rules numerically, at both the high energy scale (GUT scale) and the electroweak scale (M_Z scale). The results were obtained using a Mathematica package known as REAP [16] which solves RG equations of different neutrino quantities. The numerical analysis presented in this chapter represents cases with zero and non-zero Majorana phases. We also study two different models with light (LSD) and heavy sequential dominance (HSD). We conclude the chapter by giving justifications for our numerical approach.

The second part of this thesis involves studying the stabilisation of moduli fields resulting from string compactifications and their contribution to driving cosmological inflation. Similarly to the first part, this part is also divided into three chapters as described below.

Chapter 5 gives a brief introduction to string compactification starting with a review of Kaluza Klein reduction. We then discuss flux compactification and review the nature of moduli fields that result from such compactifications. We also state the importance of generating a potential for these moduli so that they can be trapped and stabilised at their Vevs. Finally, we present the four dimensional content of heterotic and type IIA string compactifications on $T^6/(Z_2 \times Z_2)$ orientifolds which represent the background of the models considered in the following chapters.

Chapter 6 considers four dimensional models originating from type IIA and heterotic string compactifications on $T^6/(Z_2 \times Z_2)$ orientifolds. The resulting superpotentials are combinations of a flux term and a condensate term, both of which are given in terms of moduli fields. Extremisation and Supersymmetry breaking conditions are derived and studied for each model in order to find a minimum of

the potential along the directions of the relevant moduli. The process of uplifting the flat directions, in these models, is also presented.

Chapter 7 is the final chapter in part II and considers inflation within the framework of the models discussed in Chapter 6. A brief introduction to the theory of inflation is given. We then outline the main conditions for achieving slow-roll inflation. This is followed by a detailed analysis of some of the models presented in the previous chapter to see whether inflation is successfully achieved along all moduli directions. Finally, we comment on an important structure of the potential obtained when considering type IIA models. This interesting structure involves the existence of a global minimum surrounded by a set of local minima (false vacua) along certain axionic directions.

We end the thesis with a short chapter giving some concluding remarks. We also provide three appendices where we describe the diagonalisation procedure of the left-handed neutrino matrix, the derivation of neutrino mass terms which are considered in Chapter 3, as well as the numerical calculations of the Hessian matrices for the models presented in Chapter 6.

Part I

Neutrino Mixing

Chapter 2

Neutrino Mass and Mixing: An Overview

In this chapter, we give a brief review of neutrino mixing. We also discuss the different types of neutrino mass that can be generated, which then leads us to the introduction of the see-saw mechanism. A non-exhaustive list of useful reviews on neutrino mass and mixing is [17, 18, 19, 20, 21].

2.1 Neutrinos in the Standard Model

The Standard Model [22] is one of the most successful theories in particle physics. It describes all the particles that are observed in nature and their interactions. The latter are namely: the strong force, the weak force and the electromagnetic force. The particle content of the model is classified in three generations of fermions, each containing a quark pair and lepton pair (u, d, e, ν_e), (c, s, μ, ν_μ) and (t, b, τ, ν_τ). The gauge group of the SM is $G_{SM} = SU(3)_C \times SU(2)_L \times U(1)_Y$. It contains spin-1 particles associated with the fundamental interactions. These particles include gluons which are responsible for the strong force, the photon for electromagnetic interactions and massive vector bosons responsible for mediating weak interactions.

So far, we have only considered the particle content of the SM without introducing any mass terms. These mass terms are extremely essential according to experimental results which show that all particles have masses, for instance we know that the electron has a mass of 511 eV. A mechanism known as the Higgs mechanism is responsible for generating masses for the gauge bosons as well as the fermions

present in the SM. This is characterised by adding a Higgs scalar doublet to the spectrum of the Standard Model. Introducing the Higgs mechanism breaks the electroweak symmetry down to the electromagnetic symmetry.

$$SU(2)_L \times U(1)_Y \rightarrow U(1)_{EM}$$

The basic idea of this mechanism is that the Higgs interacts with the SM particles which causes the breaking of this symmetry (also known as spontaneous electroweak symmetry breaking (EWSB)) and the particles to acquire masses. This symmetry is broken due to the fact that the potential of the Higgs field develops a non-trivial vacuum expectation value (VEV). We will see later how this process, when applied in the SM, generates mass terms for the massive gauge bosons W^+, W^- and Z. The most general form for the Lagrangian density is,

$$\mathcal{L}_{Yukawa} = -\overline{Q}_{iL}\phi d_{jR}Y^d_{ij} - \overline{Q}_{iL}\phi^c u_{jR}Y^u_{ij} - \overline{L}_{iL}\phi e_{jR}Y^e_{ij} + h.c. \tag{2.1}$$

where $\phi^c \equiv (-i\tau_2\phi^*)$, Y^u_{ij}, Y^d_{ij}, Y^e_{ij} are 3×3 Yukawa matrices and the indices $i, j = \{1, 2, 3\}$ refer to the three different families. Q_{iL} and L_{iL} are left-handed quark lepton doublets while d_{jR}, u_{jR} and e_{jR} are $SU(2)_L$ singlet fields of down quarks, up quarks and charged leptons respectively. To see how the masses for fermions and gauge bosons are generated in the SM, we consider an isospin doublet of scalar fields with weak hypercharge $Y = 1/2$

$$\phi = \begin{pmatrix} \phi^+ \\ \phi^0 \end{pmatrix} \tag{2.2}$$

where the complex scalar fields ϕ^+, ϕ^0 are given by,

$$\phi^+ \equiv (\phi_1 + i\phi_2)/\sqrt{2}, \quad \phi^0 \equiv (\phi_3 + i\phi_4)/\sqrt{2}$$

The Lagrangian of the Higgs doublet must be invariant under $SU(2)_L \times U(1)_Y$ symmetry. The simplest choice can be written as

$$\mathcal{L}_{Higgs} = (D_\mu\phi)^\dagger(D^\mu\phi) - \mu^2\phi^\dagger\phi - \lambda(\phi^\dagger\phi)^2 \tag{2.3}$$

where μ^2 and λ are real parameters with $\lambda > 0$. In order to have massless photon, the electromagnetic symmetry $U(1)_{EM}$ must remain unbroken. This can be achieved by taking the coefficient μ^2 to be negative. As a result, the Higgs potential ($V = \mu^2\phi^\dagger\phi + \lambda(\phi^\dagger\phi)^2$) develops a non zero minimum at $\langle\phi^\dagger\phi\rangle = -\mu^2/2\lambda$

By expanding around this vacuum, the Higgs vacuum expectation value (Vev) can be written as

$$\phi(x) = \frac{1}{\sqrt{2}} \begin{pmatrix} 0 \\ v + h(x) \end{pmatrix} \tag{2.4}$$

where $v = \sqrt{\frac{-\mu^2}{\lambda}}$ and $h(x)$ is the physical Higgs field. After the Higgs field acquires its Vev, The gauge boson mass terms can be identified as given by the following Higgs Lagrangian,

$$(D_\mu \phi)^\dagger (D^\mu \phi) = \frac{v^2}{4} g^2 W_\mu^+ W^{-\mu} + \frac{v^2}{8}(g^2 + g'^2) Z_\mu Z^\mu + ... \tag{2.5}$$

where

$$W_\mu^\pm = \frac{1}{\sqrt{2}}(A_\mu^1 \pm i A_\mu^2)$$

The masses of $W^\pm$ and Z bosons can be given respectively as

$$M_W = \frac{gv}{2}, \quad M_Z = \sqrt{g^2 + g'^2} = \frac{gv}{2\cos\theta_W} \tag{2.6}$$

where $\theta_W = tan^{-1}(g'/g)$ is the weak mixing angle.

We have seen how the mass terms for the gauge bosons are generated after introducing the Higgs mechanism into the SM. All fermions present in the SM, except neutrinos, acquire mass terms through the same process. After spontaneous symmetry breaking, these masses are generated by substituting the Higgs VEV into the Yukawa Lagrangian, in Eq.(2.1), to give masses of the form,

$$m_{ij}^{u,d,e} = \frac{v}{\sqrt{2}} Y_{ij}^{u,d,e} \tag{2.7}$$

When the Standard Model was first formulated, neutrinos were thought to be massless for many reasons, including the absence of right-handed neutrinos. However, in recent years neutrino experiments have shown convincing evidence that neutrinos are massive as a consequence of their oscillations. As a result, the study of the physics of neutrino mass and mixing became one of the leading candidates in the field of physics beyond the Standard Model. One way of generating neutrino masses in the SM is by introducing right-handed neutrinos, which gives rise to neutrino Dirac mass term of the form $m_{\mathrm{D}}^{\nu} \overline{\nu_{\mathrm{L}}} \nu_{\mathrm{R}}$ when a right handed neutrino field ν_R interacts with a left handed field ν_L. This type of mass is forbidden in the SM without the Higgs doublet since only the left handed neutrinos transform under $SU(2)$ and therefore the mass term is not invariant under the electroweak

symmetry. In the next section, we will briefly review the main experimental results supporting neutrino oscillations and also the different types of neutrino mass that can be generated.

2.2 Evidence of neutrino oscillations

Neutrinos are electrically neutral particles of spin 1/2, which play an important role in the $SU(2)_L \times U(1)_Y$ electroweak theory. They appear in at least three different flavours, which are all left-handed, meaning that their spins point in opposite directions from their momenta. These three flavours are known respectively as the electron neutrino ν_e, the muon neutrino ν_μ and the tau neutrino ν_τ. Their anti-particles, on the other-hand are right-handed.

There are many sources of neutrinos, the most important one is the Sun which emits around 2×10^{38} electron neutrinos per second. Other sources include relic neutrinos, which are left over from the early stages of evolution of the universe and nuclear plants producing mainly electron-antineutrinos. Type II Supernovae are also a good source of neutrinos emitting nearly 6×10^{58} of neutrinos with different flavours every ten seconds.

Neutrino oscillations were first discussed in 1957 by Pontecorvo. In his study, he mainly looked at oscillations between neutrinos and anti-neutrinos in analogy with the oscillations of Kaons and their anti-particles. Mixing between two massive neutrinos was only studied after the discovery of muon neutrinos. It was first discussed by Maki, Nakagawa and Sakata in 1962.

The first experimental evidence of neutrino oscillation came from the Raymond Davis experiment [1], when a deficit in the number of solar neutrinos ν_e, reaching the earth, was observed (only 1/3 of the total number predicted by solar models). The discrepancy between the theoretical models and the results of this experiment led to the conclusion that the electron neutrino is in fact oscillating into other flavours such as muon or tau neutrinos.

Another compelling evidence for neutrino oscillations was the data presented by Super-Kamiokande laboratory in 1998 [2]. The results showed a deficit in the number of muon neutrinos reaching Earth when they had travelled a significant distance. These results were interpreted as evidence that muon neutrinos oscillate into tau neutrinos which shows that at least one neutrino flavour has a non-zero

mass. The Super-Kamiokande experiment has also confirmed the results of Davis's experiment and a deficit in the flux of electron neutrinos originating from the sun was observed. Sudbury Neutrino Observatory (SNO), KamLAND, K2K and MINOS are other experiments which confirmed neutrino flavour oscillation [3, 4]. In summary, we see that there is strong evidence from different experimental sources that supports neutrino flavour oscillation. The existence of these oscillations means that neutrinos are not massless as predicted by the SM. In the next section, we discuss the different types of neutrino masses that can be generated after introducing right-handed neutrinos to the Standard Model.

2.3 Neutrino masses

The smallness of neutrino masses, compared to other fermions in the Standard Model, has been a good description of nature for a long time. However, these particles appear to be massive according to experimental results. So to resolve this problem, we have to find a way of introducing these masses in the SM. There is also a problem of defining the nature of neutrino masses which raises the question: are neutrino masses Majorana or Dirac masses? If we have a close look at the nature of neutrinos in order to answer this question, we find that they have no charge and no colour compared to the other fermions. This evidently means that they can be their own anti-particles or what is known as Majorana fermions. For the remainder of this part, we will assume that neutrinos are Majorana.

In the SM, we can have left-handed Majorana masses which are achieved when a left-handed neutrino field ν_L couples to its own charge and parity conjugated state ν_L^c, in other words it couples to a right handed antineutrino field,

$$m_L^{\nu}\overline{\nu_{\mathrm{L}}}\nu_{\mathrm{L}}^{\mathrm{C}}, \tag{2.8}$$

where the charge conjugate of the left-handed neutrino ν_L^c can be written as,

$$\nu_L^c = C\overline{\nu}_L^T,$$

and C is a unitary matrix of charge conjugation which satisfies the following relations:

$$C\gamma_\alpha^T C^{-1} = -\gamma_\alpha, \quad C^\dagger = C^{-1}, \quad C^T = -C$$

Such Majorana masses do not conserve lepton number (L) and since the combination $\overline{\nu}_L^c \nu_L$ belongs to a triplet, these masses are strictly forbidden in the SM assuming only Higgs doublets are present. Another obvious way of generating neutrino masses in the SM is by introducing right-handed neutrino fields ν_R. This gives rise to Dirac masses of the form,

$$m_{\mathrm{D}}^{\nu} \overline{\nu_{\mathrm{L}}} \nu_{\mathrm{R}} \tag{2.9}$$

which are achieved when the right-handed neutrino field ν_R interacts with the left-handed neutrino field ν_L. The Dirac mass terms mimic the mass terms of quarks and charged leptons by conserving the lepton number and therefore this type of masses is allowed by the symmetries of the SM as they are generated through the Higgs mechanism.

Adding right-handed neutrinos ν_R to the SM generates another type of Majorana masses called right-handed Majorana masses which result from the right-handed neutrino field ν_R coupling to its CP conjugate field ν_R^c. These masses are also allowed in the SM and have the following form:

$$M_{\mathrm{R}} \overline{\nu_{\mathrm{R}}} \nu_{\mathrm{R}}^{\mathrm{C}} \ , \tag{2.10}$$

We now return to our previous question of defining the nature of neutrinos. Since left-hand Majorana masses do not conserve lepton number, future experiments may confirm whether this lepton number violation is mainly caused by the presence of such mass terms, through a very promising approach known as Neutrinoless double beta decay. In this process, a nucleus consisting of N neutrons decays to N+2 neutrinos by emitting two electrons. If this process is observed, it will confirm that neutrinos are different from the other fermions in the SM and that they are indeed Majorana fermions.

So far, we have summarised three types of neutrino masses which are possible after introducing right-handed neutrino fields. While the left-handed Majorana masses are zero in the SM, the magnitude of the right-handed Majorana masses can be very large since, in principal, there is nothing that prevents the right-handed neutrino field from coupling to its CP conjugate. This leads to very small effective left-handed Majorana masses which is explained by an appealing and simple mechanism known as the see-saw mechanism [23].

2.4 The see-saw mechanism

In the SM, the right-handed Majorana masses M_R can be very heavy compared to very small effective left-handed neutrino masses. The smallness of these effective masses is explained by an elegant mechanism known as the see-saw mechanism. Both Dirac and Majorana masses are present in this mechanism and the main idea is to assume that left-handed Majorana masses are zero to start with as predicted by the SM, but are effectively generated after introducing the right-handed neutrino ν_R [23]. Once this is done then the right handed Majorana masses and the Dirac masses are permitted and we have the following mass matrix,

$$M = \begin{pmatrix} \overline{\nu}_{\mathrm{L}}^{c} & \overline{\nu}_{R} \end{pmatrix} \begin{pmatrix} 0 & m_D \\ m_D^T & M_R \end{pmatrix} \begin{pmatrix} \nu_L \\ \nu_R^c \end{pmatrix}. \tag{2.11}$$

The application of this mechanism means that half of neutrinos are the familiar light neutrinos while the other half are extremely heavy right-handed Majorana neutrinos with masses, M_R. The right-handed Majorana masses may be orders of magnitude larger than the electroweak scale, or possibly as large as the GUT scale. One can diagonalize the matrix in Eq.(2.11) to give effective Majorana masses of the type in Eq.(2.8) in the approximation that $M_R \gg m_D$,

$$m_L = -m_D M_R^{-1} m_D^T \,. \tag{2.12}$$

Diagonalising the above matrix M gives rise to two different masses. One of them is M_R and the other one is $(m_D)^2/M_R$ which is equivalent to the effective Majorana mass m_L. We can see that $m_L \ll m_D$ since it is suppressed with respect to m_D by the small ratio m_D/m_R given that m_R can be very large. For example, taking m_D of order of the weak scale and M_R of order close to the GUT scale, we find $m_L \sim 10^{-3}$ eV which looks good for solar neutrinos.

We have seen how the smallness of the effective neutrino Majorana masses is explained by the see-saw mechanism. However, we still cannot explain the assumption that the right-handed Majorana mass M_R is so large compared to the electroweak scale and the Dirac mass. It is believed that this is mainly due to the fact that M_R is generated at very high energies by the symmetry breaking of the theory beyond the SM.

The version of the see-saw mechanism discussed so far is known as type I see-saw mechanism, which is illustrated in Fig.(2.1). Type I see-saw mechanism is often generalized to a type II see-saw, in Pati-Salam models or GUTs based on $SO(10)$,

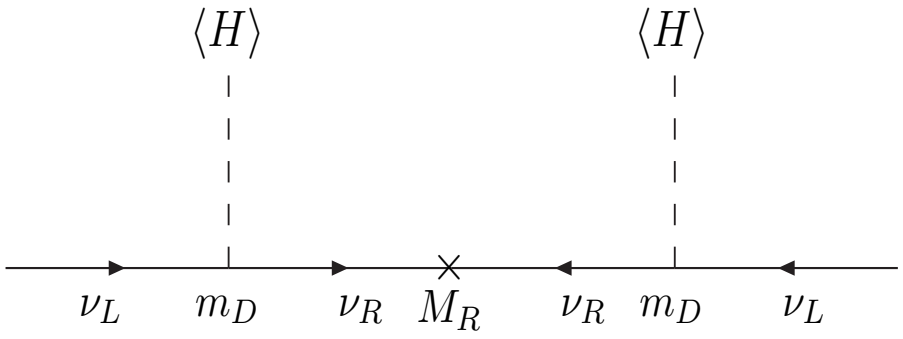

FIGURE 2.1: Type I see-saw mechanism.

where an additional mass term m_L^{II} for the light neutrinos is present [24]. We will not discuss type II see-saw mechanism here as it is not within the scope of this thesis.

2.5 Neutrino mixing

As discussed in previous sections, there is strong experimental evidence that neutrinos change from one flavour to another which leads us to the subject of "neutrino mixing". Neutrino mixing is described by the so called "lepton mixing matrix" U (this is also known as the Pontecorvo-Maki-Nakagawa-Sakata matrix U_{PMNS} or just U_{MNS}). For the remainder of this part, we will assume the name U_{PMNS} unless stated otherwise. This is a unitary matrix connecting the neutrino flavour fields $\nu_f \equiv \{\nu_e, \nu_\mu, \nu_\tau\}$ to the neutrino mass fields $\nu_m \equiv \{\nu_1, \nu_2, \nu_3\}$ with masses m_1, m_2, m_3 respectively as presented in Eq.(2.13),

$$\nu_f = U_{PMNS}\ \nu_m \tag{2.13}$$

Current data shows that the state ν_1 comprises mostly ν_e while the state ν_2 includes nearly equal amounts of ν_e, ν_μ and ν_τ. On the other hand, the state ν_3 consists mainly of ν_μ and ν_τ. The difference between the mass eigenstates and the neutrino flavour eigenstates is what causes neutrinos to oscillate from one flavour to another.

Mixing between neutrino flavours may involve two states as well as three families. According to experimental data, the simplest case of neutrino mixing occurs when muon neutrinos oscillate into tau neutrinos, which is known atmospheric mixing.

$$\begin{pmatrix} \nu_\mu \\ \nu_\tau \end{pmatrix} = \begin{pmatrix} c_{23} & s_{23} \\ -s_{23} & c_{23} \end{pmatrix} \begin{pmatrix} \nu_2 \\ \nu_3 \end{pmatrix}, \tag{2.14}$$

here and in the remainder of this part, we will take $s_{ij} \equiv \sin\theta_{ij}$ and $c_{ij} \equiv \cos\theta_{ij}$, where θ_{ij} are the neutrino mixing angles. In this mixing, only two mass eigenstates and two flavour eigenstates are relevant. The current experimental data supports maximal mixing with,

$$\sin^2 2\theta_{23} = 1$$

As discussed earlier, the three-flavour mixing is governed by a 3×3 unitary matrix presented in Eq.(2.13). Assuming the light neutrinos are Majorana, this matrix can be parameterised by three mixing angles θ_{ij} and three complex phases as follows:

$$U = \begin{pmatrix} 1 & 0 & 0 \\ 0 & c_{23} & s_{23} \\ 0 & -s_{23} & c_{23} \end{pmatrix} \begin{pmatrix} c_{13} & 0 & s_{13}e^{-i\delta} \\ 0 & 1 & 0 \\ -s_{13}e^{i\delta} & 0 & c_{13} \end{pmatrix} \begin{pmatrix} c_{12} & s_{12} & 0 \\ -s_{12} & c_{12} & 0 \\ 0 & 0 & 1 \end{pmatrix} P_M, \tag{2.15}$$

where $P_M = diag(e^{i\frac{\alpha_1}{2}}, e^{i\frac{\alpha_2}{2}}, 0)$ is the matrix containing the Majorana phases α_1, α_2. These phases do not affect neutrino oscillation and have physical consequences only if neutrinos are Majorana particles. They can be eliminated in the case of massive neutrinos being Dirac particles and not Majorana. This is done by rephasing the massive neutrino fields which will leave the Dirac term invariant. The first matrix in the above equation corresponds to Atmospheric neutrino mixing that we discussed earlier. The second matrix describes Reactor neutrino oscillations, which are assiciated with the detection of anti-electron neutrinos. Solar neutrino oscillations are described by the third matrix in Eq.(2.15). Recent experimental data from KamLAND [25] have confirmed these oscillations specifying the large mixing angle (LMA) solar solution with the value,

$$\sin^2\theta_{12} \approx 0.30$$

three flavour mixing also involves studying neutrino masses. In the standard Particle Data Group (PDG) parametrization, the PMNS matrix can be written as

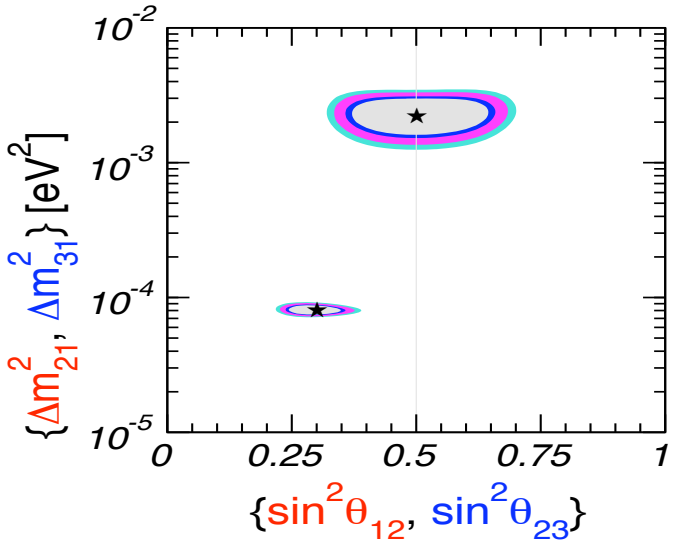

FIGURE 2.2: Experimental allowed regions for the atmospheric and solar mixing angles as well as the mass difference squared terms [26].

$$U_{PMNS} = \begin{pmatrix} c_{12}c_{13} & s_{12}c_{13} & s_{13}e^{-i\delta} \\ -c_{23}s_{12} - s_{13}s_{23}c_{12}e^{i\delta} & c_{23}c_{12} - s_{13}s_{23}s_{12}e^{i\delta} & s_{23}c_{13} \\ s_{23}s_{12} - s_{13}c_{23}c_{12}e^{i\delta} & -s_{23}c_{12} - s_{13}c_{23}s_{12}e^{i\delta} & c_{23}c_{13} \end{pmatrix} P_M, \tag{2.16}$$

where δ is the Dirac phase and P_M is the Majorana phase matrix. From the above mixing matrix, we can see that the presence the phase δ is related to the appearance of the mixing angle θ_{13}, which means that the size of CP violation will depend on this angle. This is one of the main reasons why exact measurement of this angle is so important in neutrino physics.

Experimental values and errors for the three neutrino oscillation parameters are summarised in Tab.(2.1) [26, 27, 28]. Experimental allowed regions for the atmospheric and solar mixing angles are shown in Fig.(2.2) [26].

Parameter	Best fit ($^\circ$)	2 σ ($^\circ$)	3 σ ($^\circ$)
θ_{12}	34.44	31.94- 37.46	30.65- 39.23
θ_{23}	45	38.05 - 52.53	35.66 - 54.93
θ_{13}	4.79	$\leq$ 10.46	$\leq$ 12.92

TABLE 2.1: Best fit values, 2 σ and 3 σ intervals for the three- flavour neutrino oscillation parameters from global data including accelerator (K2K and MINOS) and solar, atmospheric, reactor (Kam LAND and CHOOZ) experiments [27].

2.6 Tri-bimaximal mixing

Tri-bimaximal mixing (TB) [5, 6] is achieved in the framework of three-family mixing with $\sin^2\theta_{23} = 1/2, \quad \sin^2\theta_{12} = 1/3, \quad \theta_{13} = 0$. The lepton mixing matrix is then given by,

$$U_{PMNS} \approx \begin{pmatrix} \sqrt{\frac{2}{3}} & \frac{1}{\sqrt{3}} & 0 \\ -\frac{1}{\sqrt{6}} & \frac{1}{\sqrt{3}} & \frac{1}{\sqrt{2}} \\ \frac{1}{\sqrt{6}} & -\frac{1}{\sqrt{3}} & \frac{1}{\sqrt{2}} \end{pmatrix}. \tag{2.17}$$

We can explain tri-bimaximal mixing in terms of flavours and mass eigenstates. It corresponds to the state ν_1 having a sixth of both ν_μ and ν_τ and two thirds of ν_e. As can be seen from the above matrix, only ν_τ and ν_μ feature in the third state ν_3 corresponding to the third column of U_{PMNS}, with equal amounts. On the other hand, all the flavours are involved in the state ν_2 with equal parts as shown by the middle column of the mixing matrix.

The latest data from neutrino oscillation experiments is consistent with this TB pattern. With the advancement of technology, future neutrino experiments will be extremely sensitive to small deviations from TB mixing and therefore it is of great importance to study the theoretical uncertainty in such type of mixing. With this in mind, constructing a new parameterisation of the $PMNS$ matrix, in which these deviations feature explicitly, might be very useful for both experiments and theoretical studies of neutrino oscillation. Such parameterisation was developed in [29]. It was achieved by taking an expansion about the tri-bimaximal matrix in analogy with Wolfenstein parameterisation of quark mixing. Three small parameters r, s and a are introduced to describe the deviations of the reactor, solar and atmospheric angles from their tri-bimaximal values,

$$s_{13} = \frac{r}{\sqrt{2}}, \quad s_{12} = \frac{1}{\sqrt{3}}(1+s), \quad s_{23} = \frac{1}{\sqrt{2}}(1+a). \tag{2.18}$$

Global fits of the corresponding mixing angles can be translated into the ranges [26],

$$0 < r < 0.22, \quad -0.11 < s < 0.04, \quad -0.12 < a < 0.13. \tag{2.19}$$

Considering an expansion of the lepton mixing matrix in powers of r, s, a about the tri-bimaximal form. One gets the following form for the mixing matrix to first

order in r, s, a,

$$U_{MNS} \approx \begin{pmatrix} \sqrt{\frac{2}{3}}(1-\frac{1}{2}s) & \frac{1}{\sqrt{3}}(1+s) & \frac{1}{\sqrt{2}}re^{-i\delta} \\ -\frac{1}{\sqrt{6}}(1+s-a+re^{i\delta}) & \frac{1}{\sqrt{3}}(1-\frac{1}{2}s-a-\frac{1}{2}re^{i\delta}) & \frac{1}{\sqrt{2}}(1+a) \\ \frac{1}{\sqrt{6}}(1+s+a-re^{i\delta}) & -\frac{1}{\sqrt{3}}(1-\frac{1}{2}s+a+\frac{1}{2}re^{i\delta}) & \frac{1}{\sqrt{2}}(1-a) \end{pmatrix} P_M \tag{2.20}$$

2.7 Charged lepton corrections

Lepton mixing can originate entirely from the neutrino sector or from the charged lepton sector depending on the chosen basis. It can also be generated in both sectors and, in this case, the Lagrangian is written in terms of mass matrices of charged leptons M_e and neutrinos m_ν as,

$$\mathcal{L} = -\bar{e}_L M_e e_R - \frac{1}{2}\bar{\nu}_L m_L \nu_L^c + H.c, \tag{2.21}$$

The change in basis from flavour to eigenbasis is performed by,

$$V_{e_L} M_e V_{e_R}^\dagger = \begin{pmatrix} m_e & 0 & 0 \\ 0 & m_\mu & 0 \\ 0 & 0 & m_\tau \end{pmatrix}, \quad V_{\nu_L} m_{LL} V_{\nu_L}^T = \begin{pmatrix} m_1 & 0 & 0 \\ 0 & m_2 & 0 \\ 0 & 0 & m_3 \end{pmatrix}. \tag{2.22}$$

The PMNS matrix is constructed as a product of a unitary matrix from the charged lepton sector V_{e_L} and a unitary matrix from the neutrino sector V_{ν_L},

$$U_{PMNS} = V_{e_L} V_{\nu_L}^\dagger \tag{2.23}$$

Now that we have discussed tri-bimaximal mixing in the framework of neutrino oscillations, we need to look into how this mixing is actually achieved and in what basis. There have been many theoretical speculations about the best way to construct this pattern. Most of the proposed models consider two particular bases. The first basis is the flavour basis in which the charged lepton mass matrix is diagonal, while the neutrino mass matrix takes a particular form such that is results in TB mixing. The second basis is a particular basis first introduced by Cabibbo and Wolfenstein in which both the neutrino and charged lepton mass matrices are non-diagonal, but in which the charged lepton mass matrix is diagonalised by

a "democratic unitary matrix" involving elements of equal magnitude but differing by a phase $\omega = 2\pi/3$. Such a Cabibbo-Wolfenstein basis is particularly well suited to models of TB mixing based on the discrete group A_4 [30]. However in other classes of models, one attempts to work in the flavour basis and to derive TB mixing purely from the neutrino sector with the charged lepton matrix being diagonal, for example using constrained sequential dominance (CSD) [7].

2.8 Charged lepton corrections and sum rules

Tri-bimaximal mixing may be accurately achieved in the neutrino sector for models arising from Grand Unified Theories (GUTs). However the charged lepton mass matrix is never accurately diagonal in the flavour basis. Instead, in such models, the charged lepton mass matrix often resembles the down quark mass matrix, and involves an additional Cabibbo-like rotation in order to diagonalize it. In these models, TB mixing arises in the neutrino sector, but with charged lepton corrections giving deviations [31]. Such Cabibbo-like charged lepton corrections lead to well defined corrections to TB mixing which can be cast in the form of sum rules. In this section, we review the derivations of different types of these sum rules, involving neutrino mixing angles as well as TB deviation parameters.

2.8.1 Cabibbo-like corrections and sum rules

We consider the case where TB mixing applies quite accurately only to the neutrino mixing in some basis where the charged lepton mass matrix is not exactly diagonal [32, 33]. This is a situation often encountered in realistic models [7]. Furthermore in GUT models it is often the case that, in the basis where the neutrino mixing is of the TB form, the charged lepton mixing matrix has a Cabibbo-like structure rather similar to the quark mixing and is dominated by a 1-2 mixing θ_{12}^E [34],

$$V_{e_L} = \begin{pmatrix} c_{\theta_{12}^E} & -s_{\theta_{12}^E} e^{-i\lambda_{12}^E} & 0 \\ s_{\theta_{12}^E} e^{i\lambda_{12}^E} & c_{\theta_{12}^E} & 0 \\ 0 & 0 & 1 \end{pmatrix}, \tag{2.24}$$

where $c_{\theta_{12}^E} \equiv \cos\theta_{12}^E$, $s_{\theta_{12}^E} \equiv \sin\theta_{12}^E$, and λ_{12}^E is a phase required for the diagonalisation of the charged lepton mass matrix [7]. The physical PMNS oscillation phase

δ turns out to be related to λ_{12}^E by [34],

$$\delta = \lambda_{12}^E + \pi. \tag{2.25}$$

We assume that the neutrino mixing is accurately of the TB form,

$$V_{\nu_L}^\dagger = \begin{pmatrix} \sqrt{\frac{2}{3}} & \frac{1}{\sqrt{3}} & 0 \\ -\frac{1}{\sqrt{6}} & \frac{1}{\sqrt{3}} & \frac{1}{\sqrt{2}} \\ \frac{1}{\sqrt{6}} & -\frac{1}{\sqrt{3}} & \frac{1}{\sqrt{2}} \end{pmatrix} P_M. \tag{2.26}$$

The physical mixing matrix, given by Eq.(2.23), can then be expressed using Eqs.(2.24, 2.26). The standard PDG form of the PMNS mixing matrix in Eq.(2.16) requires real elements $(U_{PMNS})_{11}$ and $(U_{PMNS})_{12}$ and this may be achieved by use of the phases in $P_M = diag(e^{i\frac{\alpha_1}{2}}, e^{i\frac{\alpha_2}{2}}, 0)$.

It follows that $(U_{PMNS})_{31}$, $(U_{PMNS})_{32}$ and $(U_{PMNS})_{33}$ are unaffected by the Cabibbo-like charged lepton corrections and are hence given by:

$$|(U_{PMNS})_{31}| = |(V_{\nu_L}^\dagger)_{31}| = \frac{1}{\sqrt{6}}, \tag{2.27}$$

$$|(U_{PMNS})_{32}| = |(V_{\nu_L}^\dagger)_{32}| = \frac{1}{\sqrt{3}}, \tag{2.28}$$

$$|(U_{PMNS})_{33}| = |(V_{\nu_L}^\dagger)_{33}| = \frac{1}{\sqrt{2}}. \tag{2.29}$$

Since these relations are all on the same footing, it is sufficient to discuss one of them only and in the following we choose to focus on Eq.(2.27). Using Eq.(2.16), Eq.(2.27) can be expanded in terms of the standard mixing angles leading to the following sum rule,

$$\Gamma_1 \equiv \arcsin\left(\sqrt{2}\ |s_{23}s_{12} - s_{13}c_{23}c_{12}e^{i\delta}|\right) = 35.26^o, \tag{2.30}$$

where we have assumed $s_{23}^\nu \equiv \sin\theta_{23}^\nu = \frac{1}{\sqrt{2}}$. This sum rule can be simplified further to leading order in s_{13},

$$\Gamma_2 \equiv \arcsin\left(\sqrt{2}\ (s_{23}s_{12} - s_{13}c_{23}c_{12}\cos\delta)\right) \approx 35.26^o. \tag{2.31}$$

From Eq.(2.29) and using $s_{23} = c_{23} = 1/\sqrt{2}$, we can express the above sum rule to leading order as,

$$\Gamma_3 \equiv \theta_{12} - \theta_{13}\cos(\delta) \approx 35.26^o. \tag{2.32}$$

The last form of the sum rule was first presented in [7], while all the above forms can be found in [35, 36]. In Chapter 4, we shall study all three forms of the sum rules Γ_i, together with some related sum rules which we now discuss.

In order to see how deviations from TB mixing manifest, we also define the following parameters which express the deviation of the magnitude of the third row mixing matrix elements from their tri-bimaximal values:

$$\begin{aligned} |(U_{PMNS})_{31}| &\equiv \frac{1}{\sqrt{6}}(1+\xi_1) \\ |(U_{PMNS})_{32}| &\equiv \frac{1}{\sqrt{3}}(1+\xi_2) \\ |(U_{PMNS})_{33}| &\equiv \frac{1}{\sqrt{2}}(1+\xi_3) \end{aligned} \tag{2.33}$$

Hence from Eq.(2.16), we get the following expressions for the ξ_i parameters

$$\begin{aligned} \xi_1 &= \sqrt{6}\ |s_{23}s_{12} - s_{13}c_{23}c_{12}e^{i\delta}| - 1, \\ \xi_2 &= \sqrt{3}\ | - s_{23}c_{12} - s_{13}c_{23}s_{12}e^{i\delta}| - 1, \\ \xi_3 &= \sqrt{2}\ |c_{23}c_{13}| - 1. \end{aligned} \tag{2.34}$$

These third family deviation parameters ξ_i can also be expressed in terms of the deviation parameters r, s, a, using Eq.(2.20), as follows

$$\begin{aligned} \xi_1 &\approx |1 + s + a - re^{i\delta}| - 1, \\ \xi_2 &\approx |1 - \tfrac{1}{2}s + a + \tfrac{1}{2}re^{i\delta}| - 1, \\ \xi_3 &\approx |1 - a| - 1. \end{aligned} \tag{2.35}$$

We can express the relations, given by Eqs.(2.27, 2.28, 2.29), in terms of the third family deviation parameters defined in Eq.(2.33) as simply:

$$\xi_i = 0. \tag{2.36}$$

Using the parametrization in Eq.(2.18), the sum rule in Eq.(2.32) can be expressed in terms of the deviation parameters s, r and the Dirac CP phase (δ)[29],

$$\sigma_1 = r\cos\delta - s = 0. \tag{2.37}$$

To deal with issues of canonical normalisation corrections, the following sum rule has been proposed [37, 38],

$$\sigma_2 = r\cos\delta + \frac{2}{3}a - s = 0. \tag{2.38}$$

This sum rule was claimed to be stable under leading logarithmic third family RG corrections, although, as emphasized in [37, 38], it does not include the effect of running the mixing angle, θ_{13}, or r, whose inclusion introduces a Majorana phase dependence.[1] Such effects will be studied numerically in Chapter 4.

So far, we presented a set of sum rules involving the neutrino mixing matrix as well as the TB deviation parameters. In Chapter 4, we will study the RG running of these sum rules from the GUT scale to the M_Z scale, using the Mathematica package REAP, for two GUT inspired numerical models. However, before we discuss the RG running, we will first look at the analytic derivations of the three neutrino mixing angles, in general SD, as presented in the next chapter.

[1] This sum rule was derived from an expansion in m_2/m_3, and the running of r was neglected because it is suppressed by an extra factor of m_2/m_3 compared to the running of s and a.

Chapter 3

NLO and NNLO Corrections to Neutrino Parameters

In this chapter, we present analytic expressions for the neutrino mixing angles including the NLO and NNLO corrections originating from the second lightest and lightest neutrino masses [39]. We start by reviewing Sequential Dominance (SD) in the framework of type I see-saw mechanism. We also review the special cases of Constrained Sequential Dominance (CSD) and Partially Constrained Sequential Dominance (PCSD). We then present numerical results for the analytic formulae of the neutrino mixing angles and masses, for two GUT models, in the presence of NLO and NNLO corrections. Finally, we compare the numerical results to those evaluated using the Mathematica package MPT/REAP [16] [1].

3.1 Sequential dominance

Sequential dominance is a very elegant way of accounting for a neutrino mass hierarchy with large atmospheric and solar mixing angles. In the framework of the see-saw mechanism, diagonalising the complex neutrino Majorana matrix m^{ν}_{LL} gives rise to neutrino masses m_1, m_2 and m_3,

$$V^{\nu_L} m^{\nu}_{LL} V^{\nu_L T} = \begin{pmatrix} m_1 & 0 & 0 \\ 0 & m_2 & 0 \\ 0 & 0 & m_3 \end{pmatrix} \tag{3.1}$$

[1] Mixing Parameter Tools (MPT) is a package provided with REAP and it is mainly used to extract neutrino mixing parameters.

In the case of see-saw mechanism with right-handed neutrino dominance, a particular high energy theory includes a charged lepton Yukawa matrix Y^E, a neutrino Yukawa matrix Y^ν and a right-handed neutrino Majorana matrix M_{RR}.

Let us consider the case where the right-handed neutrino Majorana matrix takes a diagonal form with real eigenvalues as,

$$M_{RR} \approx \begin{pmatrix} Y & 0 & 0 \\ 0 & X & 0 \\ 0 & 0 & X' \end{pmatrix}. \tag{3.2}$$

We also write the complex neutrino (Dirac) Yukawa matrix Y^ν_{LR} in terms of the Yukawa couplings a,b,c,d,e,f,a',b',c' as

$$Y^\nu_{LR} = \begin{pmatrix} d & a & a' \\ e & b & b' \\ f & c & c' \end{pmatrix}. \tag{3.3}$$

The neutrino mass matrix can be derived using the see-saw formula, given by Eq.(2.12),

$$m^\nu_{LL} = \begin{pmatrix} \frac{a'^2}{X'} + \frac{a^2}{X} + \frac{d^2}{Y} & \frac{a'b'}{X'} + \frac{ab}{X} + \frac{de}{Y} & \frac{a'c'}{X'} + \frac{ac}{X} + \frac{df}{Y} \\ \frac{a'b'}{X'} + \frac{ab}{X} + \frac{de}{Y} & \frac{b'^2}{X'} + \frac{b^2}{X} + \frac{e^2}{Y} & \frac{b'c'}{X'} + \frac{bc}{X} + \frac{ef}{Y} \\ \frac{b'^2}{X'} + \frac{b^2}{X} + \frac{e^2}{Y} & \frac{b'c'}{X'} + \frac{bc}{X} + \frac{ef}{Y} & \frac{c'^2}{X'} + \frac{c^2}{X} + \frac{f^2}{Y} \end{pmatrix} \tag{3.4}$$

In SD, the atmospheric and solar neutrino mixing angles are obtained in terms of ratios of Yukawa couplings involving the dominant and subdominant right-handed neutrinos, respectively. Assuming for simplicity that $d = 0$, SD then corresponds to the right-handed neutrino of mass Y being the dominant term, while the right-handed neutrino of mass X giving the leading sub-dominant contribution to the see-saw mechanism. The SD condition can then be expressed as,

$$\frac{|e^2|, |f^2|, |ef|}{Y} \gg \frac{|xy|}{X} \gg \frac{x'y'}{X'} \tag{3.5}$$

where $x, y \in a, b, c$ and $x', y' \in a', b'c'$, and all Yukawa couplings are assumed to be complex. Therefore, according to SD, the leading order (LO) contribution to the neutrino mass matrix comes from one single right- handed neutrino resulting in a single neutrino mass eigenvalue m_3 and the "atmospheric" mixing angle θ_{23}. The second largest next-to-leading order (NLO) contribution to the neutrino mass

matrix in SD, arising from a second right-handed neutrino, induces the second neutrino mass m_2 as well as the "solar" and "reactor" mixing angles θ_{12} and θ_{13}, respectively.

In unified models, a third right-handed neutrino contributes to the seesaw mechanism with SD and its next-to-next-to-leading order (NNLO) contribution provides a mass m_1 to the lightest neutrino, which will also give corrections to the analytic expressions for the neutrino mixing angles at NNLO. These corrections , which are of order m_1/m_3, depend on the rather large 3-3 Yukawa coupling c'. The analytic estimates of the mixing angles in SD have so far only been presented to LO [40, 41] and these are given by,

$$\tan\theta_{23}^{\nu} \approx \frac{|e|}{|f|}, \tag{3.6}$$

$$\tan\theta_{12}^{\nu} \approx \frac{|a|}{c_{23}|b|\cos(\phi_b') - s_{23}|c|\cos(\phi_c')}, \tag{3.7}$$

$$\theta_{13} \approx e^{i(\phi_2+\phi_a-\phi_e)}\frac{|a|(e^*b+f^*c)}{(|e|^2+|f|^2)^{3/2}}\frac{Y}{X}, \tag{3.8}$$

where some of the Yukawa couplings were written as $x = |x|e^{i\phi_x}$. The phases χ^{ν} and ϕ_2^{ν} are fixed to give real angles θ_{12}^{ν} and θ_{13}^{ν} by:

$$c_{23}|b|\sin(\phi_b') \approx s_{23}|c|\sin(\phi_c'), \tag{3.9}$$

$$\phi_2 \approx \phi_e - \phi_a - \phi^*, \tag{3.10}$$

where

$$\phi_b' \equiv \phi_b - \phi_a - \phi_2 - \chi, \tag{3.11}$$

$$\phi_c' \equiv \phi_c - \phi_a + \phi_e - \phi_f - \phi_2 - \chi, \tag{3.12}$$

$$\phi^* = arg(e^*b + f^*c) \tag{3.13}$$

and $c_{23} \equiv \cos(\theta_{23})$ and $s_{23} \equiv \sin(\theta_{23})$.

In the large d limit, the angle θ_{13} can be expressed as follows [40]:

$$\theta_{13} \approx \frac{|d|}{\sqrt{|e|^2+|f|^2}} \equiv \theta_{13}^0. \tag{3.14}$$

Note that θ_{13} and θ_{13}^0 are given differently in the small d and large d cases so we must be careful to distinguish the two limiting cases. The phases ϕ_2 and ϕ_3

appearing in Eq.(A.9) are fixed by:

$$\phi_2 = \phi_e - \phi_d \tag{3.15}$$

$$\phi_3 = \phi_f - \phi_d. \tag{3.16}$$

In this chapter, we shall derive similar analytic expressions, in the framework of type I see-saw mechanism with SD, including both the NLO and NNLO corrections. The derivation of these analytic expressions builds on the results presented in [40] where the NLO and NNLO corrections were not considered [2]. For the remainder of this chapter, we will take the LO formulae of the mixing angles given by Eqs.(3.6, 3.7, 3.8, 3.14) to be t^0_{23}, t^0_{12} and θ^0_{13} respectively.

3.2 Special cases of Sequential Dominance

3.2.1 Constrained Sequential Dominance

Constrained Sequential Dominance (CSD) [7] corresponds to SD with the constraints defined as,

$$|a| = |b| = |c|, \tag{3.17}$$

$$|d| = 0, \tag{3.18}$$

$$|e| = |f| \tag{3.19}$$

$$e^*b + f^*c = 0, \tag{3.20}$$

where the parameters a, b, c, e, f, d are the complex Yukawa couplings presented in Eq.(3.3). The above CSD constraints give rise to TB neutrino mixing, in which $\tan\theta^\nu_{23} = 1$, $\tan\theta^\nu_{12} = 1/\sqrt{2}$ and $\theta^\nu_{13} = 0$. In CSD, a strong hierarchy $|m_1| \ll |m_2| < |m_3|$ is assumed which enables m_1 to be effectively ignored (typically this is achieved by taking the third right-handed neutrino mass X' to be very heavy leading to a very light m_1). We note that numerical results of neutrino mixing angles at CSD, in the presence of non-zero 3-3 Yukawa coupling, are only accurate to leading order in m_2/m_3 [40, 42, 43] and therefore these conditions do not give rise to precise TB neutrino mixing. In Chapter 4, we shall see that accurate TB neutrino mixing only arises when the CSD conditions are perturbed.

[2] Although the NLO corrections were calculated for the atmospheric angle they were not considered for the other angles, and NNLO corrections were completely neglected [40].

3.2.2 Partially Constrained Sequential Dominance

Tri-bimaximal-reactor Mixing (TBR) [44] can arise from type I see-saw mechanism via a very simple modification to CSD called Partially Constrained Sequential Dominance (PCSD). This modification involves allowing a non-zero 1-1 element of the Dirac neutrino mass matrix.

TBR mixing corresponds to the mixing matrix,

$$U_{TBR} = \begin{pmatrix} \sqrt{\frac{2}{3}} & \frac{1}{\sqrt{3}} & \frac{1}{\sqrt{2}}re^{-i\delta} \\ -\frac{1}{\sqrt{6}}(1+re^{i\delta}) & \frac{1}{\sqrt{3}}(1-\frac{1}{2}re^{i\delta}) & \frac{1}{\sqrt{2}} \\ \frac{1}{\sqrt{6}}(1-re^{i\delta}) & -\frac{1}{\sqrt{3}}(1+\frac{1}{2}re^{i\delta}) & \frac{1}{\sqrt{2}} \end{pmatrix} P_M, \tag{3.21}$$

where we have introduced the reactor parameter r defined by $s_{13} = \frac{r}{\sqrt{2}}$ [29] and $s^2_{13} \approx 0.02$ corresponds to $r \approx 0.2$. Estimates suggest that PCSD is capable of accommodating a sizeable reactor angle while the atmospheric and solar angles are predicted to remain close to their TB values [44]. Similarly to the CSD case, LO analytic results in the PCSD case are not very accurate and in general they receive both NLO and NNLO corrections as we shall see in subsequent sections.

3.3 Neutrino parameters in general SD to NLO and NNLO

In this section, we derive approximate analytic expressions for neutrino mixing angles in the case of neutrino mass hierarchy, in general SD including NLO and NNLO corections. The derivations make use of the diagonalisation procedure outlined in Appendix A.

3.3.1 Derivation of the atmospheric angle

As discussed in Appendix A, the diagonalisation of the mass matrix involves applying the real rotation R_{23} after re-phasing the neutrino mass matrix. This rotation gives rise to two new mass terms $\tilde{m}^{\nu}_{22}$ and m'_3 given by Eqs.(B.5,B.3) respectively.

Let us start by writing the lower 23 block in terms of the Yukawa couplings,

$$\begin{pmatrix} m_{22} & m_{23} \\ m_{23} & m_{33} \end{pmatrix} = \begin{pmatrix} \frac{b^2}{X} + \frac{e^2}{Y} & \frac{bc}{X} + \frac{ef}{Y} \\ \frac{bc}{X} + \frac{ef}{Y} & \frac{c'^2}{X'} + \frac{c^2}{X} + \frac{f^2}{Y} \end{pmatrix} \tag{3.22}$$

Diagonalising the 23 block according to Eq.(A.10) gives rise to an expression for $\tan(2\theta_{23})$ in terms of the lower block masses and phase ϕ_2, ϕ_3. This can be written as,

$$\tan(2\theta_{23}) = \frac{2(|m_{23}|e^{i(\phi_{23}-\phi_2-\phi_3)})}{|m_{33}|e^{i(\phi_{33}-2\phi_3)} - |m_{22}|e^{i(\phi_{22}-2\phi_2)}} \tag{3.23}$$

Substituing for the masses in Eq.(3.23), we get the following expression of $\tan(2\theta_{23})$ in terms of the complex Yukawa couplings,

$$\tan(2\theta_{23}) \approx \frac{2\frac{ef}{Y}(1+\epsilon_1)e^{i(-\phi_2-\phi_3)}}{\frac{f^2}{Y}(1+\epsilon_2+\eta_1)e^{i(-2\phi_3)} - \frac{e^2}{Y}(1+\epsilon_3)e^{i(-2\phi_2)}}, \tag{3.24}$$

where we have introduced new parameters $\epsilon_1, \epsilon_2, \epsilon_3$ and η_1, which are given as follows,

$$\epsilon_1 = \frac{\frac{bc}{X}}{\frac{ef}{Y}}, \quad \epsilon_2 = \frac{\frac{c^2}{X}}{\frac{f^2}{Y}}, \quad \epsilon_3 = \frac{\frac{b^2}{X}}{\frac{e^2}{Y}}, \quad \eta_1 = \frac{\frac{c'^2}{X'}}{\frac{f^2}{Y}}. \tag{3.25}$$

Note that ϵ_i, η_i are of order $m_2/m_3, m_1/m_3$ respectively, so that ϵ_i parametrise the NLO corrections while η_i parametrise the NNLO corrections.

Introducing the small parameter δ such that $|f| = |e|(1-\delta)$, we get

$$\begin{aligned} \tan(2\theta_{23}) &\approx \frac{2\frac{|e|^2}{Y}(1-\delta)(1+\epsilon_1)e^{i(\phi_e+\phi_f-\phi_2-\phi_3)}}{\frac{|e|^2}{Y}(1-2\delta)(1+\epsilon_2+\eta_1)e^{i(2\phi_f-2\phi_3)} - \frac{|e|^2}{Y}(1+\epsilon_3)e^{i(2\phi_e-2\phi_2)}}, \\ &\approx \tan(2\theta^{\nu}_{23})|_{|e|=|f|}\left(1 - \delta(1 - \frac{2(1+\epsilon_2+\eta_1)}{\epsilon_2+\eta_1-\epsilon_3})\right), \end{aligned} \tag{3.26}$$

Using Eq.(3.26), we get the final formula for the atmospheric angle, which can be written in SD as,

$$\tan(\theta_{23}) \approx t^0_{23}(1 + \mathrm{Re}\,(\gamma)), \tag{3.27}$$

where the complex couplings e, f are written in terms of their absolute values and phases as $e = |e|e^{i\phi_e}$, $f = |f|e^{i\phi_f}$ respectively. $t^0_{23} \equiv \tan(\theta_{23})|_{\epsilon_i=0,\eta_i=0}$ is given by Eq.(3.6) and the complex parameter γ is written, to leading order in ϵ_i, η_1, as:

$$\gamma \approx \frac{1}{2}(\epsilon_3 - \epsilon_2 - \eta_1) + \frac{\delta}{2}(\epsilon_3 + \epsilon_2 - 2\epsilon_1 + \eta_1). \tag{3.28}$$

We note that the final analytic expression of $\tan(\theta_{23})$, given by Eq.(3.27), depends only on the absolute values of e, f and the parameter γ. On the other hand, the phases ϕ_e, ϕ_f are not important for determining this angle. Here and in the remainder of this chapter, we will refer to $\sin(\theta_{23})$ and $\cos(\theta_{23})$, in the limit $\epsilon_i = 0, \eta_1 = 0$, as s^0_{23}, c^0_{23} respectively.

3.3.2 Derivation of the reactor angle

We apply the R_{13} rotation, as outlined in Appendix A, which modifies the outer block of the mass matrix as,

$$\begin{pmatrix} \tilde{m}_{11} & 0 \\ 0 & m'_3 \end{pmatrix} \equiv {R_{13}}^T \begin{pmatrix} m_{11} & \tilde{m}_{13} \\ \tilde{m}_{13} & m'_3 \end{pmatrix} R_{13} \tag{3.29}$$

We consider the reduced matrix that only involves the 13 elements and this gives rise to two zeros in the $13, 31$ positions as presented in Eq.(3.29). The neutrino angle θ_{13} can then be written as,

$$\begin{aligned} \theta^{\nu}_{13} &\approx \frac{\tilde{m}^{\nu}_{13}}{m'_3}, \\ &\approx \frac{1}{m'^0_3}(\tilde{m}^0_{13}(1-\gamma(s^0_{23})^2) + e^{-i\phi_2}\gamma s^0_{23}(\frac{ab}{X} + \frac{de}{Y}))(1-\beta), \end{aligned} \tag{3.30}$$

where the masses m'^0_3, m^0_{13}, are given by Eqs.(B.4, B.10) respectively. The complex parameter β is given by:

$$\beta \approx (s^0_{23})^2\epsilon_3 + (c^0_{23})^2(\epsilon_2 + \eta_1) - \epsilon_4 e^{-2i\phi_e}, \tag{3.31}$$

where the NLO correction parameter ϵ_4 is defined as,

$$\epsilon_4 = \frac{(bc^0_{23} - cs^0_{23}e^{i(\phi_e - \phi_f)})^2}{X}\left(\frac{|e|^2 + |f|^2}{Y}\right)^{-1}.$$

We can simplify Eq.(3.30) further, after expressing the masses m'^0_3, m^0_{13}, in terms of the complex couplings, by considering two different limits, namely the large d limit and the small d limit, as follows:

In the large d **limit**, $\frac{|de|}{Y}, \frac{|df|}{Y} >> \frac{|ab|}{X}, \frac{|ac|}{X}$, the angle θ_{13} can be expressed as,

$$\begin{aligned} \theta_{13} &\approx e^{i(\phi_2-\phi_e+\phi_d)}\frac{|d|}{\sqrt{|e|^2+|f|^2}}(1-\mathrm{Re}\,(\beta)) && (3.32)\\ &\approx \theta^0_{13}(1-\mathrm{Re}\,(\beta)), && (3.33)\end{aligned}$$

where the angle $\theta^0_{13} \equiv \theta_{13}|_{\eta_i=0,\epsilon_i=0}$ is given by Eq.(3.14) and the phases are fixed by $\phi_2 = \phi_e - \phi_d$.

In the small d **limit**, $\frac{|de|}{Y}, \frac{|df|}{Y} << \frac{|ab|}{X}, \frac{|ac|}{X}$, which is usually the case in CSD, θ_{13} can be expressed as,

$$\begin{aligned} \theta_{13} &\approx \theta^0_{13}\left(1-\mathrm{Re}\,(\gamma)(s^0_{23})^2-\mathrm{Re}\,(\beta)\right) && (3.34)\\ &+ s^0_{23}|\epsilon_5|\left((\mathrm{Re}\,\gamma\cos(\phi')-\mathrm{Im}\,\gamma\sin(\phi'))^2+(\mathrm{Re}\,\gamma\sin(\phi')+\mathrm{Im}\,\gamma\cos(\phi'))^2\right)^{\frac{1}{2}}, \end{aligned}$$

where $\phi' = \phi_2 - 2\phi_e$ and θ^0_{13}, in this limit, is derived in [41] and given by Eq.(3.8). The NLO correction parameter ϵ_5 is defined as,

$$\epsilon_5 = \frac{ab}{X}\left(\frac{|e|^2+|f|^2}{Y}\right)^{-1}. \qquad (3.35)$$

From Eq.(3.34), we can see that θ_{13} is proportional to θ^0_{13} with a small correction given in terms of the NLO and NNLO parameters. This result shows that the angle θ_{13} can be non-zero, in this limit, even in the case of vanishing LO result presented by θ^0_{13}.

In the PCSD case with non-zero d, we can write the leading result for θ_{13} as,

$$\begin{aligned} \theta_{13} &\approx \left(\theta^0_{13}+\frac{|d|}{\sqrt{|e|^2+|f|^2}}\right)\left(1-\mathrm{Re}\,(\gamma)(s^0_{23})^2-\mathrm{Re}\,(\beta)\right) && (3.36)\\ &+ s^0_{23}|\epsilon_5|\left((\mathrm{Re}\,\gamma\cos(\phi')-\mathrm{Im}\,\gamma\sin(\phi'))^2+(\mathrm{Re}\,\gamma\sin(\phi')+\mathrm{Im}\,\gamma\cos(\phi'))^2\right)^{\frac{1}{2}}\\ &+ s^0_{23}\,\mathrm{Re}\,(\gamma)\frac{|d||e|}{|e|^2+|f|^2}, \end{aligned}$$

where θ^0_{13} and the parameter ϵ_5 are given by Eqs.(3.8,3.35) respectively.

3.3.3 Derivation of the solar angle

As shown in Eq.(A.6), applying the phase matrix P_1 introduces a new phase χ to the mass matrix. We can then apply the real rotation R_{12}, as presented in

Eq.(A.12), which modifies the matrix by putting zeros in the $12, 21$ positions.

Using Eqs.(B.5, B.7,B.11), we get the following expression for $\tan(2\theta_{12})$,

$$\begin{aligned}\tan(2\theta_{12}) &= \frac{2|\tilde{m}_{12}|e^{i(\tilde{\phi}_{12}-\chi)}}{|\tilde{m}_{22}|e^{i(\tilde{\phi}_{22}-2\chi)}-\tilde{m}_{11}} \\ &\approx \frac{2AB}{B^2-A^2}\left(1-\gamma(s_{23}^0)^2-\zeta_1-\zeta_2\left(1-\zeta_1-\gamma(s_{23}^0)^2\right)\right), \quad (3.37)\end{aligned}$$

where, similarly to [40], A, B are expressed in terms of the complex couplings as,

$$A = \frac{a}{\sqrt{X}},$$

$$B = e^{-i(\phi_2-\chi)}\frac{c_{23}^0 b - s_{23}^0 c e^{i(\phi_e-\phi_f)}}{\sqrt{X}}.$$

and the new parameters ζ_1 and ζ_2 are given, in the small d limit, to first order in γ and β as,

$$\zeta_1 \approx e^{-i(\phi_3+\chi)}\left(\frac{acs_{23}^0}{ABX}\right)\gamma, \quad (3.38)$$

$$\zeta_2 \approx \frac{1}{B^2-A^2}\left(\eta_2\left(\frac{b^2}{X}+\frac{e^2}{Y}\right)e^{-2i\chi}-B^2\beta\right), \quad (3.39)$$

where η_2 is given by,

$$\eta_2 = \frac{c'^2}{X'}\left(\frac{|e|^2+|f|^2}{Y}\right)^{-1}. \quad (3.40)$$

Similarly to the derivation of the atmospheric angle, we can easily derive an expression for the solar mixing angle in SD using Eq.(3.37), which gives

$$\begin{aligned}\tan(\theta_{12}) &\approx \frac{A}{B}(1-\mathrm{Re}\,(\zeta')), \\ &\approx t_{12}^0(1-\mathrm{Re}\,(\zeta')), \quad (3.41)\end{aligned}$$

where $t_{12}^0 \equiv \tan(\theta_{12})|_{\eta_i=0,\epsilon_i=0}$ is given by Eq.(3.7). The new parameter ζ' is given as,

$$\zeta' \approx \frac{B^2-A^2}{B^2+A^2}\left(\gamma(s_{23}^0)^2+\zeta_1+\zeta_2(1-\zeta_1-\gamma(s_{23}^0)^2)\right). \quad (3.42)$$

3.4 Analytic results in the special cases of SD

In this section, we will look at how the rather complicated analytic results for the neutrino mixing angles, derived in the previous section, can be simplified in the special SD cases (CSD and PCSD). We will also look at whether the NLO and NNLO corrections will survive in these cases. For simplicity and for the remainder of this section, we shall take $\phi_e = \pi$ and all the remaining Yukawa phases to be zero except $\phi_{c'}$ which is left general.

3.4.1 Neutrino mixing angles in CSD

As discussed in Section.3.2, CSD corresponds to SD with the constraints given by Eqs.(3.17-3.20). In the CSD limit, there are no NLO corrections to the TB neutrino mixing angles. However, in practice, the large 3-3 Yukawa coupling (c') may be expected to lead to a non-zero m_1, and in this case the TB mixing angles would be expected to be subject to NNLO corrections. Using the analytic results, derived in the previous section, in SD to NLO and NNLO, we can verify that the NLO corrections vanish in all cases for CSD leaving only the NNLO corrections.

3.4.1.1 The atmospheric angle

We can write the atmospheric angle, given by Eq.(3.27), in CSD as,

$$\tan(\theta_{23})^{CSD} \approx 1 + \text{Re}\,(\gamma^{CSD}), \tag{3.43}$$

which involves a correction γ given by Eq.(3.28). This correction depends on the NLO parameters ϵ_i and the NNLO parameters η_i presented in Eq.(3.25). The CSD conditions, given by Eqs.(3.17-3.20), imply that the ϵ_i are equal ($\epsilon_2 = \epsilon_3 = -\epsilon_1$) and $\delta = 0$. From Eq.(3.28), it is clear that the NLO contributions to γ described by the ϵ_i cancel. This result implies that the atmospheric angle is corrected by γ which only involves NNLO corrections and it is given by,

$$\gamma^{CSD} \approx -\frac{\eta_1}{2} \approx -\frac{1}{2}\frac{|c'|^2 Y}{|e|^2 X'} e^{i2\phi_{c'}}. \tag{3.44}$$

3.4.1.2 The reactor angle

For the reactor angle θ_{13}, we only need to consider the expression valid in the small d limit given by Eq.(3.34) since the other limit contradicts with CSD. Imposing the CSD conditions in Eqs.(3.17-3.20), the LO result for the reactor angle (θ_{13}^0) becomes exactly zero as can seen from Eq.(3.8). As a result, the first term of Eq.(3.34) vanishes. The third term also vanishes for CSD and we are only left with the second term of order $\eta\epsilon$,

$$\theta_{13}^{CSD} \approx s_{23}^0 \epsilon_5 Re(\gamma^{CSD}) = \frac{1}{4\sqrt{2}} \frac{|b|^2 Y^2 |c'|^2}{|e|^4 X X'} \cos(2\phi_{c'}). \tag{3.45}$$

The above analytic result implies that the reactor angle is given by a term proportional to NNLO.NLO corrections.

3.4.1.3 The solar angle

We can also simplify the solar angle, given by Eq.(3.41), in the CSD case. This angle can be expressed as,

$$\tan(\theta_{12})^{CSD} \approx \frac{1}{\sqrt{2}}(1 - \text{ Re}\,(\zeta'^{CSD})) \tag{3.46}$$

which involves a correction ζ' given by Eq.(3.42). We can simplify this parameter in this limit to get,

$$\zeta'^{CSD} \approx \frac{1}{3}\left(\frac{\gamma^{CSD}}{2} + \zeta_1^{CSD} + \zeta_2^{CSD}\right). \tag{3.47}$$

which depends on γ^{CSD} as well as the parameters ζ_1, ζ_2 presented in Eqs.(3.38,3.39). We note that ξ' also depends on the small parameter β, through ξ_2, which is given by Eq.(3.31). The parameter γ^{CSD} takes the simplified form, which is presented in Eq.(3.44). The remaining parameters β, ζ_1, ζ_2, given by Eqs.(3.31, 3.38, 3.39), can also be simplified in CSD and take the following forms,

$$\beta^{CSD} \approx -\gamma^{CSD}, \tag{3.48}$$

$$\zeta_1^{CSD} \approx -\frac{\gamma^{CSD}}{2}, \tag{3.49}$$

$$\zeta_2^{CSD} \approx \frac{1}{2}\frac{|c'|^2 X}{|a|^2 X'} e^{i2\phi_{c'}}. \tag{3.50}$$

We also note that the NLO corrections vanish in this case and the solar angle is corrected only by NNLO corrections.

3.4.2 Neutrino mixing angles in PCSD

As discussed in Section 3.2.2, PCSD is similar to the CSD case defined by Eqs.(3.17-3.20), but with a non-zero value of 1-1 Yukawa coupling d. Similarly to the results found in the case of CSD, we shall see that the mixing angles derived in the PCSD case are only corrected by NNLO corrections while the NLO corrections vanish.

3.4.2.1 The atmospheric angle

In the PCSD case, the atmospheric angle given by Eq.(3.27) becomes,

$$\tan(\theta_{23})^{PCSD} \approx 1 + \text{Re}\,(\gamma^{PCSD}). \tag{3.51}$$

The small parameter γ in this case is identical to the case of CSD,

$$\gamma^{PCSD} = \gamma^{CSD}. \tag{3.52}$$

This result implies that the atmospheric angle correction only involves NNLO corrections, as in the case of CSD.

3.4.2.2 The reactor angle

We can simplify the reactor angle θ_{13}, presented in Eq.(3.30), in PCSD to find,

$$\theta_{13}^{PCSD} \approx \theta_{13}^{0}(1 + \text{Re}\,(\gamma^{PCSD})) - \frac{\text{Re}\,(\gamma^{PCSD})}{2}\frac{|b|^2 Y}{\sqrt{2}|e|^2 X}. \tag{3.53}$$

where the LO expression for the reactor angle, in the large d limit, is given by Eq.(3.14), and can be written as,

$$\theta_{13}^{0} \approx \frac{|d|}{\sqrt{2}|e|}. \tag{3.54}$$

Therefore, the reactor angle only receives NNLO corrections, similar to the CSD case.

3.4.2.3 The solar angle

In the PCSD case, the solar angle, given by Eq.(3.41), can be simplified as

$$\tan(\theta_{12})^{PCSD} \approx \frac{1}{\sqrt{2}}(1 - \mathrm{Re}\,(\zeta'^{PCSD})), \tag{3.55}$$

which involves a small correction ζ' given by Eq.(3.42), which we approximate here to,

$$\zeta'^{PCSD} \approx \frac{1}{3}\left(\frac{\gamma^{PCSD}}{2} + \zeta_1^{PCSD} + \zeta_2^{PCSD}\right). \tag{3.56}$$

The parameters ζ_1, ζ_2 can be simplified in the PCSD case as,

$$\zeta_1^{PCSD} \approx \gamma^{PCSD}(1 + \theta_{13}^0 \frac{\sqrt{2}|e|^2 X}{|b|^2 Y}) \tag{3.57}$$

$$\zeta_2^{PCSD} \approx \zeta_2^{CSD} + \sqrt{2}\theta_{13}^0 \gamma^{PCSD} + (\theta_{13}^0)^2, \tag{3.58}$$

where the LO expression for the reactor angle (θ_{13}^0) is given by Eq.(3.54). We note that the NLO corrections also vanish for the solar angle in the PCSD case however there is a correction of order $(\theta_{13}^0)^2$. The presence of the $(\theta_{13}^0)^2$ correction is due to the difference in the diagonalisation procedure between 2-3 and 1-3 elements of the neutrino mass. We note that, for the PCSD case, all corrections to the neutrino mixing angles vanish at NLO, with the NNLO corrections remaining.

3.5 Numerical results

In the previous section, analytic expressions of the neutrino mixing angles, involving NLO and NNLO corrections, were derived. Approximate results in the special SD cases (CSD and PCSD) were also presented and the NLO corrections vanished in both cases. In this section, we evaluate the analytic results for two different numerical GUT inspired models of [7, 10] previously studied in [45]. The first model is of light sequential dominance (LSD) with the lightest right-handed neutrino having the dominant contribution to the atmospheric neutrino mass. The second model is of heavy sequential dominance (HSD) [42, 43] where the heaviest right-handed neutrino gives the dominant contribution to the neutrino mass. We present a brief introduction to the two models. We then present numerical results for the neutrino mixing angles as well as the neutrino masses, presented in Appendix B. We also compare the numerical results to those obtained using the MPT/REAP package.

3.5.1 Results for the LSD model

The LSD model, we consider in this section, is a simple realistic model based on the family symmetry $SO(3)$ and Pati-Salam unification[7]. Heavy Higgs superfields $H, \overline{H}$ are introduced in order to break the Pati-Salam symmetry to the SM. The family symmetry is spontaneously broken ($SO(3) \rightarrow SO(2) \rightarrow Nothing$) by introducing flavon fields ϕ_i ($i = \{1, 2, 3\}$), ϕ_{23}, ϕ_{123} with the following vacuum alignment in order to achieve tri-bimaximal neutrino mixing,

$$\phi_1 = \begin{pmatrix} 1 \\ 0 \\ 0 \end{pmatrix}, \ \phi_2 = \begin{pmatrix} 0 \\ 1 \\ 0 \end{pmatrix}, \ \phi_3 = \begin{pmatrix} 0 \\ 0 \\ 1 \end{pmatrix}, \ \phi_{23} = \begin{pmatrix} 0 \\ 1 \\ -1 \end{pmatrix}, \ \phi_{123} = \begin{pmatrix} 1 \\ 1 \\ 1 \end{pmatrix}.$$

The Yukawa matrices can be obtained from the leading Yukawa operators (these operators are listed in [7]) by considering the dominance of right handed up and down messenger mass scales over left-handed.

$$M^d \approx \frac{1}{2} M^u \ll M^L$$

Symmetry breaking effects allow the following numerical values for the expansion parameters associated with ϕ_{23} where the fields are assumed to be replaced by their vevs,

$$\epsilon = \frac{\phi_{23}}{M^u} \approx 0.05, \quad \overline{\epsilon} = \frac{\phi_{23}}{M^d} \approx 0.15.$$

Numerical values are also found for the expansion parameters associated with the remaining flavons. Using these numerical values together with the leading Yukawa operators [7], the following Dirac neutrino Yukawa matrix can be achieved,

$$Y^{\nu}_{LR} \approx \begin{pmatrix} 0 & y_2\epsilon^3 & y''_3\epsilon^3 \\ y_1\epsilon^3 & y_2\epsilon^3 & 0.34y'_3\epsilon^2 \\ -y_1\epsilon^3 & y_2\epsilon^3 & y_3\overline{\epsilon}^{-\frac{1}{2}} \end{pmatrix}, \tag{3.59}$$

where the complex Yukawa couplings are written as, $y_i = |y_i|e^{i\delta_i}$. Using the Majorana operators [7], the right-handed Majorana matrix takes the following form

$$M_R = \begin{pmatrix} p\epsilon^6 & 0 & 0 \\ 0 & q\epsilon^6 & 0 \\ 0 & 0 & 1 \end{pmatrix} M_3, \tag{3.60}$$

where p, q are complex couplings and the leading heavy mass M_3 is given in terms of the Higgs vev and the neutrino messenger mass scale ($M^\nu = M^u$) as,

$$M_3 = \frac{\langle H \rangle^2}{M^\nu}$$

We can obtain numerical expressions for the neutrino Majorana mass matrix and the neutrino Yukawa matrix by taking the following values for the parameters y_1, y_2, y_3, p, q,

$$y_1 = 1.7,\ y_2 = 0.65,\ y_3 = 1.5,\ p = 0.32,\ q = 0.45. \tag{3.61}$$

These values were chosen so that the light sequential dominance relation, given by Eq.(3.5), is satisfied.

The above choice of values gives the following diagonal right-handed neutrino Majorana mass matrix M_{RR},

$$M_{RR} = \begin{pmatrix} 5.1 \times 10^7 & 0 & 0 \\ 0 & 7.05 \times 10^7 & 0 \\ 0 & 0 & 10^{16} \end{pmatrix}. \tag{3.62}$$

In addition to Eq.(3.59), we can write the Dirac neutrino Yukawa matrix as,

$$Y^\nu_{LR} = \begin{pmatrix} d & a & 0 \\ e & b & 0 \\ f & c & c' \end{pmatrix}, \tag{3.63}$$

3.5.1.1 The CSD case

We consider the LSD model, presented in the previous section, in the special case of CSD. We take the complex Yukawa coupling d to be zero as required by the CSD conditions. We also take the Yukawa couplings in the second column of Eq.(3.63) such that $|a| = |b| = |c| = 8.125 \times 10^{-5}$. In addition to this, we take the absolute values of the couplings e, f to be $|e| = |f| = 2.125 \times 10^{-4}$ while the value of the 3-3 Yukawa coupling c' is taken to be $|c'| = 0.5809$. We choose all the phases of the Yukawa couplings to be zero except ϕ_e ($\phi_e = \pi$).

Numerical results for the mixing angles, evaluated using the analytic formulae, are evaluated in the case of CSD and presented in Tab.(3.1). This table also shows

numerical results obtained using MPT/REAP package [16, 46], which appear to be very close to the ones obtained through the analytic approach. We note that here and in the remainder of this chapter, the MPT/REAP results were evaluated using the MPT package without considering RG running. As can be seen from Tab.(3.1), all the values of the mixing angles are slightly deviated from their TB values and this is mainly due to the presence of the non-zero 3-3 Yukawa coupling c'.[3] In addition to this, we present numerical values for the neutrino masses m_1, m_2 and m_3 given by Eqs.(B.13,B.14, B.15), using both MPT/REAP and the analytic formulae. As presented in Tab.(3.1), we can see that the MPT/REAP and the analytic results are very close particularly in the case of m_2.

Parameter	$\|d\|$	$\theta_{23}(^\circ)$	$\theta_{13}(^\circ)$	$\theta_{12}(^\circ)$	m_1 (eV)	m_2 (eV)	m_3 (eV)
Analytic	0	44.44	0.04	33.75	0.00015	0.0088	0.055
MPT/REAP	0	44.38	0.05	33.69	0.00016	0.0088	0.054

TABLE 3.1: Numerical results for the mixing angles and masses, evaluated in the CSD case with $c' \neq 0$, for a model with light sequential dominance. Analytic results as well as MPT/ REAP results are presented.

3.5.1.2 The PCSD case

We consider the previous LSD model in the case of PCSD with non-zero Yukawa coupling $d = 0.2|e|$, $|e| = 2.125\times10^{-4}$ and $|c'| = 0$. Keeping all the other conditions of CSD satisfied as outlined in Section 3.5.1.1, we found that the numerical values of all the mixing angles are deviated from their TB values particularly the reactor angle θ_{13} which becomes larger than zero and takes a value of 8.22^o as shown in Tab.(3.2). This large value satisfies the predictions of TBR mixing and it is in agreement with the most recent experimental results [12, 47].

MPT/REAP results for the neutrino mixing angles in this case are slightly different than the analytic results as presented in Tab.(3.2). This is mainly due to the approximate nature of the diagonalisation procedure that we followed in this thesis. Tab.(3.2) also shows numerical results for the neutrino masses m_1, m_2 and m_3 evaluated using both MPT/REAP and the analytic expressions. As expected, the neutrino mass m_1 is exactly zero in this case due to the vanishing NNLO corrections. The results for the masses m_2, m_3 in the analytic case are slightly different than the MPT/REAP case as a result of the different diagonalisation procedures.

[3] In the limit $c' = 0$, the analytic results give exact TB values ($\theta_{23} = 45^o$, $\theta_{12} = 35.26^o$, $\theta_{13} = 0.00^o$).

Parameter	$\|d\|$	$\theta_{23}(^\circ)$	$\theta_{13}(^\circ)$	$\theta_{12}(^\circ)$	m_1 (eV)	m_2 (eV)	m_3 (eV)
Analytic	$0.2\|e\|$	45.00	8.10	35.08	0	0.0085	0.0538
MPT/REAP	$0.2\|e\|$	44.29	8.53	34.89	0	0.0084	0.054

TABLE 3.2: Numerical results for the neutrino mixing angles and masses, evaluated in the PCSD case for a model with light sequential dominance, with $c' = 0$ and $d = 0.2|e|$. Analytic results as well as MPT/REAP results are presented.

In order to compare our numerical values to experimental data, we present numerical results for the difference in the squares of neutrino masses Δm^2_{sol} and Δm^2_{atm}, evaluated for the LSD model, as shown in Tab.(3.3). These results are evaluated at the SD cases using both the analytic results as well as MPT/REAP. The numerical results, as shown in Tab.(3.3), are within the experimental ranges presented in [47] particularly for the value of Δm^2_{sol} at CSD which is close to the best fit value of $7.6 \times 10^{-5} eV^2$.

Parameter	Analytic	MPT/REAP	Analytic	MPT/REAP
SD case	CSD	CSD	PCSD	PCSD
Δm^2_{sol} (eV^2)	7.5×10^{-5}	7.5×10^{-5}	7.3×10^{-5}	7.1×10^{-5}
Δm^2_{atm} (eV^2)	2.11×10^{-3}	2.04×10^{-3}	2.05×10^{-3}	2.1×10^{-3}

TABLE 3.3: Analytic and MPT/REAP numerical results of the difference in the squares of neutrino masses (Δm^2_{sol} and Δm^2_{atm}) evaluated for the LSD model. The results are presented at CSD with non-zero c' as well as the PCSD case with zero c' and non-zero coupling $|d| = 0.2|e|$.

3.5.2 Results for the HSD model

To check the generality of our numerical results, we consider another model with heavy sequential dominance (HSD). The right-handed neutrino Majorana mass matrix M_{RR}, in this case, is given by,

$$M_{RR} = \begin{pmatrix} 3.991 \times 10^8 & 0 & 0 \\ 0 & 5.8 \times 10^{10} & 0 \\ 0 & 0 & 5.021 \times 10^{14} \end{pmatrix}. \tag{3.64}$$

This model satisfies HSD where the dominant contribution to the neutrino mass is coming from the heaviest right-handed neutrino. The neutrino Yukawa matrix is of the form given in Eq.(3.63) with the following values of the Yukawa couplings: $|a| = |b| = |c| = 2.401 \times 10^{-3}$, $|e| = |f| = 0.677$ and $|c'| = 2.992 \times 10^{-5}$. Similarly

to the LSD model, we take all the phases of the Yukawa couplings to be zero except the coupling e ($\phi_e = \pi$).

Analytic and MPT/REAP results of the mixing angles and masses, in CSD, are presented and compared as shown in Tab.(3.4). We note that, for this model, the values of the mixing angles are closer to their TB values compared to the LSD model, which is mainly due to the smallness of the 3-3 Yukawa coupling c' in this case. We also present results for the PCSD case with non-zero d, as shown in Tab.(3.5), and similar to the LSD model, the reactor angle is found to be large and within the recent experimental range presented in [12]. The neutrino mass m_1 is exactly zero at the PCSD case with $c' = 0$ as expected.

Parameter	$\|d\|$	$\theta_{23}(^\circ)$	$\theta_{13}(^\circ)$	$\theta_{12}(^\circ)$	m_1 (eV)	m_2 (eV)	m_3 (eV)
Analytic	0	44.96	0.003	35.18	1.01×10^{-5}	0.009	0.055
MPT/REAP	0	44.96	0.003	35.16	1.1×10^{-5}	0.009	0.055

TABLE 3.4: Numerical results for the neutrino mixing angles and masses, evaluated in CSD with $c' \neq 0$, for a model with heavy sequential dominance. Analytic results as well as MPT/REAP results are presented.

Parameter	$\|d\|$	$\theta_{23}(^\circ)$	$\theta_{13}(^\circ)$	$\theta_{12}(^\circ)$	m_1 (eV)	m_2 (eV)	m_3 (eV)
Analytic	$0.2\|e\|$	45.00	8.10	35.08	0	0.009	0.055
MPT/REAP	$0.2\|e\|$	44.27	8.55	34.89	0	0.0089	0.056

TABLE 3.5: Numerical results for the neutrino mixing angles and masses, evaluated in the PCSD case for a model with heavy sequential dominance, with $c' = 0$ and $d = 0.2|e|$. Analytic results as well as MPT/REAP results are presented.

Similarly to the LSD model, we present numerical results for the difference in the squares of neutrino masses Δm^2_{sol} and Δm^2_{atm}, evaluated for the HSD model, as shown in Tab.(3.6). The results for this model, which are also presented at both SD cases using analytic results as well as MPT/REAP, are also within the experimental ranges presented in [47]. We note that the values of Δm^2_{sol}, in all cases, are closer to the upper limit of the 3σ experimental range [47].

3.6 Summary

In this chapter, we discussed Sequential Dominance (SD) which represents an elegant way of obtaining large atmospheric and solar angles, with hierarchical neutrino masses, in the framework of type I see-saw mechanism. We also discussed

Parameter	Analytic	MPT/REAP	Analytic	MPT/REAP
SD case	CSD	CSD	PCSD	PCSD
Δm^2_{sol} (eV^2)	8.2×10^{-5}	8.15×10^{-5}	8.2×10^{-5}	8×10^{-5}
Δm^2_{atm} (eV^2)	2.162×10^{-3}	2.13×10^{-3}	2.16×10^{-3}	2.2×10^{-3}

TABLE 3.6: Analytic and MPT/REAP numerical results of the difference in the squares of neutrino masses (Δm^2_{sol} and Δm^2_{atm}) evaluated for the HSD model. The results are presented at CSD with non-zero c' as well as the PCSD case with zero c' and non-zero coupling $|d| = 0.2|e|$.

the two special cases of SD (CSD and PCSD). We derived analytic expressions for the neutrino mixing angles, including the NLO and NNLO corrections arising from the second lightest and lightest neutrino masses, in the general SD case as well as CSD and PCSD. We found that the NLO corrections to the neutrino mixing angles vanish in the case of CSD. In the PCSD case, the NLO corrections to neutrino mixing angles are suppressed by the small reactor angle and therefore the mixing angles only receive NNLO corrections.

We evaluated the analytic results for two GUT inspired models of so-called LSD type and HSD type including non-zero 3-3 Yukawa coupling in the case of CSD. For both models the analytic results agree well with the numerical results obtained using MPT tool provided with MPT/REAP. In the CSD case, the absence of NLO corrections as well as the dependence of the neutrino mixing angles on the NNLO corrections were confirmed numerically. In the PCSD case with zero 3-3 Yukawa coupling, for both numerical models, we found that the numerical results for the solar and atmospheric angles remain close to their TB values while the reactor angle is much larger than zero. This result is in good agreement with the predictions of TBR mixing in the absence or smallness of charged lepton corrections, RG effects and canonical normalisation corrections. They are also in agreement with the most recent experimental results presented in [12].

In PCSD, the comparison between the analytical results and the numerical values using MPT/REAP showed small differences, which are however within the expected range due to the approximate nature of the diagonalisation procedure followed in this work. Explicitly, θ_{12} from the analytical results is found to be larger by about 0.2^o than the MPT/REAP value, θ_{23} is larger by 0.7^o while the reactor angle θ_{13} is smaller by about 0.4^o than the MPT/REAP value for both models.

In addition to evaluating the analytic formulae for the neutrino mixing angles, we also presented numerical results for the neutrino masses m_1, m_2, m_3 as well as

the difference in the squares of neutrino masses (Δm^2_{sol} and Δm^2_{atm}), for both the LSD and the HSD models. We found that the numerical results using the analytic expressions as well as the MPT/REAP package were close and the values of the difference in mass squared were in agreement with the most recent experimental results [47].

Chapter 4

RG Running Effects on Neutrino Parameters

In Quantum Field Theory, the coupling constants are energy dependent both in QCD and QED. For instance, in the case of QED, there are one loop corrections affecting an electron or a photon propagating in vacuum. Physically, this means that there are pairs of virtual electron-positron causing a screening effect of the bare electron charge. There are essentially three one-loop divergent diagrams in QED (ultraviolet divergences) as shown in Fig.(4.1). These divergent terms, which are dependent on the momentum of the external lines, must be regulated and removed. This is handled by the process of regularisation and also by renormalising the bare quantities of the theory such as the coupling. After performing these procedures, the ultraviolet divergences can be absorbed in the coupling constant of the theory and therefore the coupling becomes momentum dependent.

In general, Renormalisation Group (GR) represents a method used in order to describe how the dynamics of a particular system or model change as a function of the energy scale. This is a very powerful tool since it allows us to study each energy scale at a time. It is also useful for testing the predictions of theoretical models against experimental results at low energy scale.

In this chapter, we study the effects of RG running and charged lepton corrections on neutrino mixing parameters. We start by looking at a numerical example of LSD type to check the reliability of the sum rules, derived in chapter 2, at low energy scale (M_Z scale) [45]. In order to examine the generality of the numerical results, we also study another numerical example satisfying HSD. The RG running

was performed using a Mathematica package known as REAP [16]. A description of this package is given in a later section.

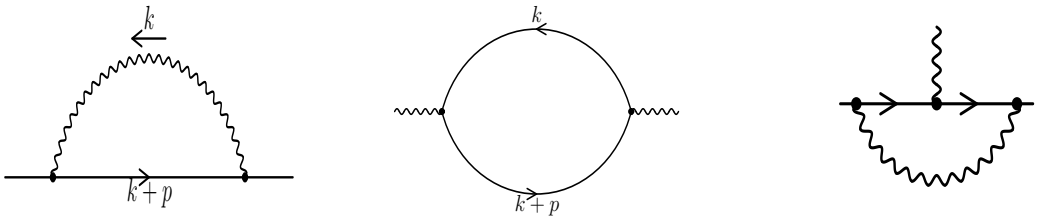

(A) (B) (C)

FIGURE 4.1: QED one-loop diagrams including electron self energy, photon self energy and QED vertex [48].

4.1 LSD numerical example

In order to study the RG corrections and reliability of the various sum rules, introduced in chapter 2, numerically it is necessary to define the GUT scale matrices rather specifically. In most of this chapter, we shall consider the same numerical model as the one described in Section 3.5.1. In Section 4.4, however, we will consider another numerical model leading to qualitatively similar results. In most of the remainder of this chapter we shall take the right-handed neutrino Majorana mass matrix M_{RR} to be diagonal and similar to the one presented by Eq.(3.62),

$$M_{RR} = \begin{pmatrix} 5.1 \times 10^{-9} & 0 & 0 \\ 0 & 7.05 \times 10^{-9} & 0 \\ 0 & 0 & 1 \end{pmatrix} M_3, \tag{4.1}$$

where $M_3 = 10^{16} GeV$. This is an example with light sequential dominance where the lightest right handed neutrino is dominant [40, 42, 43]. Ignoring RGE corrections to begin with, we find that precise tri-bimaximal neutrino mixing ($\theta_{12}^{\nu} = 35.26^{\circ}$, $\theta_{23}^{\nu} = 45.00^{\circ}$, $\theta_{13}^{\nu} = 0.00^{\circ}$) can be achieved with the Yukawa matrix,

$$Y_{LR}^{\nu} = \begin{pmatrix} 0 & 1.061667b & 0.001 \\ e & b & 0 \\ -0.9799e & b & c_3 \end{pmatrix} \tag{4.2}$$

where $b = 8.125 \times 10^{-5}$, $e = 2.125 \times 10^{-4}$ and $c_3 = 0.5809$. This matrix is similar to the one presented by Eq.(3.63) but with some tuning in order to ensure that TB

predictions are satisfied. These parameters also lead to the following values for the neutrino masses: $m_1 = 1.75 \times 10^{-4} eV$, $m_2 = 8.67 \times 10^{-3} eV$, $m_3 = 4.95 \times 10^{-2} eV$, $\Delta m^2_{atm} = 2.37 \times 10^{-3} eV^2$ and $\Delta m^2_{sol} = 7.52 \times 10^{-5} eV^2$.

The low energy pole masses of the quarks are all of the right order and given as follows: $m_u = 1.22\ MeV$, $m_d = 2.77\ MeV$, $m_s = 53\ MeV$, $m_c = 0.595\ GeV$, $m_b = 2.75\ GeV$ and $m_t = 163.6\ GeV$. In order to satisfy these values at low energy scale, REAP was used to perform the running of these masses from the M_Z scale to the GUT scale and the resulting quark Yukawa matrices Y_u and Y_d at the GUT scale were taken as initial conditions for the running of the neutrino mixing parameters and sum rules from the GUT scale to the M_Z scale.

The above parameter choice approximately satisfies the CSD conditions in Eq.(3.17). However small corrections are used in order to achieve TB neutrino mixing angles to 2 decimal places. If the CSD conditions were imposed exactly we would find instead $\theta_{12} = 33.97^\circ$, $\theta_{23} = 44.38^\circ$, $\theta_{13} = 0.059^\circ$ and $\delta = 0^\circ$ which are close to, but not accurately equal to, the TB values. This is to be expected since the SD relations are only accurate to leading order in m_2/m_3 [40, 42, 43]. We are mainly interested in studying the deviations from exact TB neutrino mixing due to charged lepton corrections and RG running, and therefore, we shall assume the matrix given by Eq.(4.2) rather than the CSD conditions as the starting point for our analysis. In this section, we will only consider the effects of charged lepton corrections on the physical mixing angles where the neutrino mixing is precisely tri-bimaximal. To study these effects, we shall use the REAP package previously discussed. We will consider cabibbo-like charged corrections, to begin, where the charged lepton Yukawa matrix is diagonal. We also discuss the more general charged lepton correction including the angle θ^E_{23}.

4.1.1 Cabibbo-like charged lepton corrections

As stated earlier, it is convenient to work in the basis where the charged lepton Yukawa matrix is diagonal. Thus, assuming cabibbo-like charged lepton corrections of the form of Eq.(2.24), the neutrino Yukawa matrix in the non-diagonal charged lepton basis must be transformed to the diagonal charged lepton basis according to:

$$Y_\nu \rightarrow Y'_\nu = V_{e_L} Y_\nu. \tag{4.3}$$

Hence the original neutrino Yukawa matrix in Eq.(4.2) must be rotated to the diagonal charged lepton basis according to Eq.(4.3).

Including the Cabibbo-like charged lepton corrections, physical tri-bimaximal mixing only holds when $\theta_{12}^E = 0$. However according to the sum rules for Γ_i, certain combinations of mixing parameters sum to 35.262° for all values of the Cabibbo-like charged lepton corrections. This is illustrated in Tabs.(4.1,4.2) where the values of the mixing angles together with the Dirac phase and the sum rules Γ_1, Γ_2, Γ_3 at the GUT scale are presented for different values of θ_{12}^E and λ_{12}^E. Γ_1 was found to be the most accurate sum rule at the GUT scale with a value of 35.262° exactly at all values of θ_{12}^E and λ_{12}^E. However the error in all the sum rules is less than about 0.1° in all the examples considered.

θ_{12}^E	0	1	3	5	8
θ_{12}	35.26	34.648	33.429	32.216	30.407
θ_{13}	0.001	0.708	2.122	3.534	5.648
θ_{23}	45.001	44.997	44.962	44.892	44.721
δ	0	210.204	210.82	211.492	212.672
Γ_1	35.262	35.262	35.262	35.262	35.262
Γ_2	35.262	35.26	35.247	35.217	35.133
Γ_3	35.261	35.26	35.252	35.23	35.162

TABLE 4.1: Values of the neutrino mixing angles θ_{12}, θ_{13} and θ_{23} together with δ and the sum rules Γ_1, Γ_2 and Γ_3 at the GUT scale, at $\lambda_{12}^E = 30^\circ$ and $tan(\beta) = 50$. All the angles are in degrees.

λ_{12}^E	0	7.5	15	30	45
θ_{12}	31.72	31.752	31.846	32.216	32.8
θ_{13}	3.534	3.534	3.534	3.534	3.534
θ_{23}	44.892	44.892	44.892	44.892	44.892
δ	180	187.9	195.789	211.492	227.039
Γ_1	35.262	35.262	35.262	35.262	35.262
Γ_2	35.262	35.259	35.250	35.217	35.174
Γ_3	35.254	35.253	35.248	35.230	35.208

TABLE 4.2: Values of the parameters: θ_{12}, θ_{13},θ_{23}, δ and the Γ_i sum rules at the GUT scale. These values are found in degrees at $\theta_{12}^E = 5^\circ$ and $\tan(\beta) = 50$.

4.1.2 More general charged lepton corrections

In the previous subsection we saw that the sum rules arising from Cabibbo-like charged lepton corrections are satisfied to excellent precision at the GUT scale, for the considered LSD numerical example. In this section we introduce the case of non-Cabibbo-like charged lepton corrections. To be precise we shall consider

more general charged lepton corrections given by,

$$V_{e_L} \approx \begin{pmatrix} c_{\theta_{12}^E} & -s_{\theta_{12}^E} e^{-i\lambda_{12}^E} & 0 \\ s_{\theta_{12}^E} e^{i\lambda_{12}^E} & c_{\theta_{12}^E} & 0 \\ 0 & 0 & 1 \end{pmatrix} \begin{pmatrix} 1 & 0 & 0 \\ 0 & c_{\theta_{23}^E} & -s_{\theta_{23}^E} e^{-i\lambda_{23}^E} \\ 0 & s_{\theta_{23}^E} e^{i\lambda_{23}^E} & c_{\theta_{23}^E} \end{pmatrix}, \tag{4.4}$$

where we have now allowed both θ_{23}^E and λ_{23}^E to be non zero. The neutrino Yukawa matrix will be transformed to the diagonal charged lepton basis according to

$$Y_\nu \to Y'_\nu = V_{e_L} Y_\nu, \tag{4.5}$$

but now using the non-Cabibbo-like charged lepton rotations in Eq.(4.4). After performing the charged lepton rotations in Eq.(4.5), values for the mixing angles as well as the ξ_i parameters given by Eq.(2.33) can be calculated at the GUT scale. Of course in the present case of non-Cabibbo-like charged lepton corrections the third row deviation parameters ξ_1, ξ_2 and ξ_3 are all expected to be non-zero at the GUT scale. This implies that the sum rules given by Eq.(2.36) no longer apply in the case of charged lepton corrections with non-zero θ_{23}^E. The effects of non-Cabibbo-like charged lepton corrections on the deviation parameters ξ_i is displayed in Tab(4.3) using the original neutrino Yukawa matrix as before, namely Eq.(4.2), but now with a small non-zero value of $\theta_{23}^E = 2^\circ$, and with different values of the new phase λ_{23}^E.

Note that the effect of turning on the charged lepton correction θ_{23}^E will lead to a correction of the physical lepton mixing angle θ_{23} but not θ_{12} (to leading order) [7]. Therefore while the sum rules $\Gamma_{1,2}$ and σ_2 are violated by a non-zero θ_{23}^E, the sum rules Γ_3 and σ_1 are both insensitive to θ_{23}^E. [1]

$\lambda_{23}^E(^\circ)$	$\lvert\xi_1\rvert$	$\lvert\xi_2\rvert$	$\lvert\xi_3\rvert$
0	0.034	0.034	0.035
30	0.027	0.031	0.030

TABLE 4.3: Values of $|\xi_1|$,$|\xi_2|$ and $|\xi_3|$ at the GUT scale for case of non-Cabibbo-like charged lepton corrections with $\theta_{12}^E = 5^\circ$, $\lambda_{12}^E = 30^\circ$, $\theta_{23}^E = 2^\circ$ and $\tan(\beta) = 50$, for different values of the phase λ_{23}^E.

[1] The insensitivity of the sum rule σ_1 to θ_{23}^E is clearly seen numerically in Fig.(4.15) (b).

4.2 Renormalization group running effects

Assuming that tri-bimaximal neutrino mixing holds in the framework of some unified theory, we expect Cabibbo-like charged lepton to give rise to corrections that can be cast in the form of sum rule relations. However, as already indicated, such sum rules are only strictly valid at the GUT scale, and will be subject to RG corrections. In this section, we present the RG running results, for the neutrino mixing angles and sum rules, from the GUT scale to the electroweak scale. For definiteness we shall assume the minimal supersymmetric standard model (MSSM), with a SUSY breaking scale of 1 TeV, below which the SM is valid.

The RG running was performed using a Mathematica package known as REAP (Renormalization of Group Evolution of Angles and Phases)[16]. This package solves renormalisation group equations of neutrino quantities such as Yukawa matrices and the gauge couplings [16]. It implements three models. The first one is the Standard Model (SM) extended by an arbitrary number of right-handed neutrinos to one-loop order. The second model is the Minimal Supersymmetric Standard Model (MSSM) extended by an arbitrary number of right-handed neutrinos to one and two-loop order. MSSM thresholds are not considered here and quarks are not integrated out for both this model and the SM. The last model is the Two Higgs Doublet Model (2HDM) with a Z_2 symmetry extended by an arbitrary number of right-handed neutrinos. The β-functions are to one-loop order and the Higgs vevs obey $v^2 = v_1^2 + v_2^2$. In all these models, the calculated evolution of the neutrino mixing parameters and mass eigenvalues can be achieved from the running of the neutrino mass matrix.

Future neutrino experiments are expected to have high sensitivities and therefore determining the RG corrections to neutrino mixing angles exactly, at the M_Z scale, is of great importance. These corrections were studied both theoretically and numerically as presented in [16, 49]. In these papers, the mixing angles were found to deviate from their TB values at the low energy scale particularly the maximal angle θ_{23}. We shall look at the deviations of the mixing angles as well as the sum rules, presented in Chapter.2, for the LSD numerical model. We will also comment on the validity of the sum rules, at the M_Z scale compared to the GUT scale, for each model. For the numerical results presented in this section, we considered all the Majorana phases of the neutrino Yukawa matrix given by Eq.(4.2) to be zero. We shall look at the case of non-zero Majorana phases in the next section.

4.2.1 Sum rules with Cabibbo-like charged lepton corrections

4.2.1.1 Sum rules in terms of mixing angles

In this section, we study the RG running of the sum rules which result from Cabibbo-like charged corrections. The neutrino Yukawa matrix is taken to be of the form of Eq.(4.2) as before. The RG change in the quantities, defined for a parameter P as $\Delta P = P_{M_Z} - P_{M_{GUT}}$, was calculated for the lepton mixing parameters and the Γ_i sum rules, and is presented in Tabs.(4.4,4.5). From the results we see that the least precise sum rule Γ_3 actually is subject to the smallest RG running since it does not involve θ_{23} which runs the most.

The RG running of Γ_i is displayed in Figs.(4.2, 4.3, 4.4, 4.5) for $\tan(\beta) = 50$. The RG evolution of Γ_1 and Γ_3 was also plotted at different values of $\tan(\beta)$ as shown in Figs.(4.6,4.7).

θ_{12}^E	0	1	3	5	8
$\Delta\theta_{12}$	+0.391	+0.402	+ 0.423	+ 0.444	+ 0.473
$\Delta\theta_{13}$	+ 0.151	- 0.116	- 0.095	- 0.071	- 0.033
$\Delta\theta_{23}$	+ 1	+ 1.001	+ 1.004	+ 1.008	+ 1.013
$\Delta\delta$	0	+ 7.453	+ 2.126	+ 1.181	+ 0.62
$\Delta\Gamma_1$	+ 0.953	+ 0.953	+ 0.953	+ 0.953	+ 0.953
$\Delta\Gamma_2$	+ 0.953	+ 0.953	+ 0.953	+ 0.954	+ 0.958
$\Delta\Gamma_3$	+ 0.237	+ 0.259	+ 0.301	+ 0.345	+ 0.412

TABLE 4.4: RG changes of the mixing parameters and sum rules Γ_1, Γ_2 and Γ_3 at $\lambda_{12}^E = 30^\circ$ and $tan(\beta) = 50$. All values are in degrees

λ_{12}^E	0	7.5	15	30	45
$\Delta\theta_{12}$	+ 0.454	+ 0.453	+ 0.452	+ 0.444	+ 0.432
$\Delta\theta_{13}$	- 0.092	- 0.091	- 0.087	- 0.071	- 0.046
$\Delta\theta_{23}$	+ 1.009	+ 1.009	+ 1.009	+ 1.008	+ 1.006
$\Delta\delta$	0	+ 0.31	+ 0.613	+ 1.181	+ 1.663
$\Delta\Gamma_1$	+ 0.953	+ 0.953	+ 0.953	+ 0.953	+ 0.953
$\Delta\Gamma_2$	+ 0.953	+ 0.953	+ 0.953	+ 0.954	+ 0.956
$\Delta\Gamma_3$	+ 0.362	+ 0.36	+ 0.357	+ 0.345	+ 0.326

TABLE 4.5: RG changes of the neutrino mixing angles, the Dirac phase δ and the sum rules Γ_1, Γ_2 and Γ_3 at $\theta_{12}^E = 5^\circ$ and $tan(\beta) = 50$. All values are in degrees.

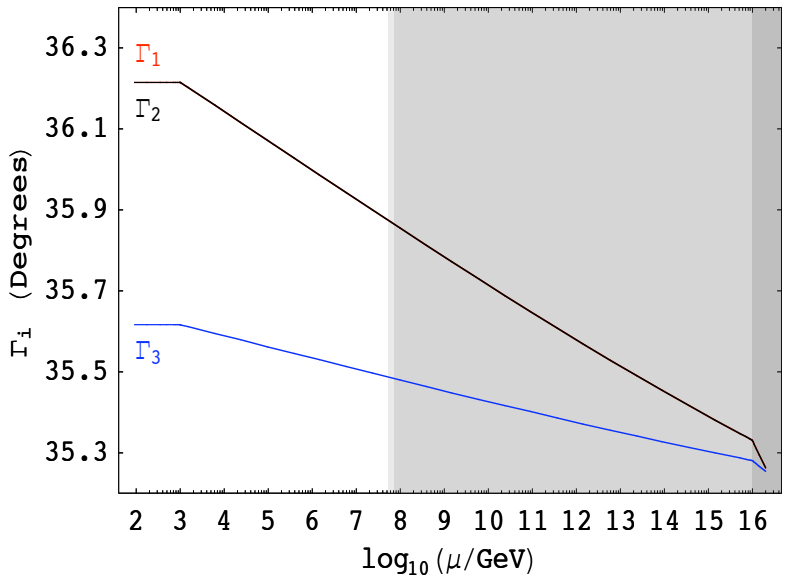

FIGURE 4.2: Evolution of sum rules Γ_1,Γ_2, Γ_3 for Cabibbo-like charged lepton corrections for large $\tan(\beta) = 50$. This running is achieved at $\theta_{12}^E = 5\,^\circ$ and $\lambda_{12}^E = 0\,^\circ$. Note how the graphs for Γ_1 and Γ_2 completely overlap.

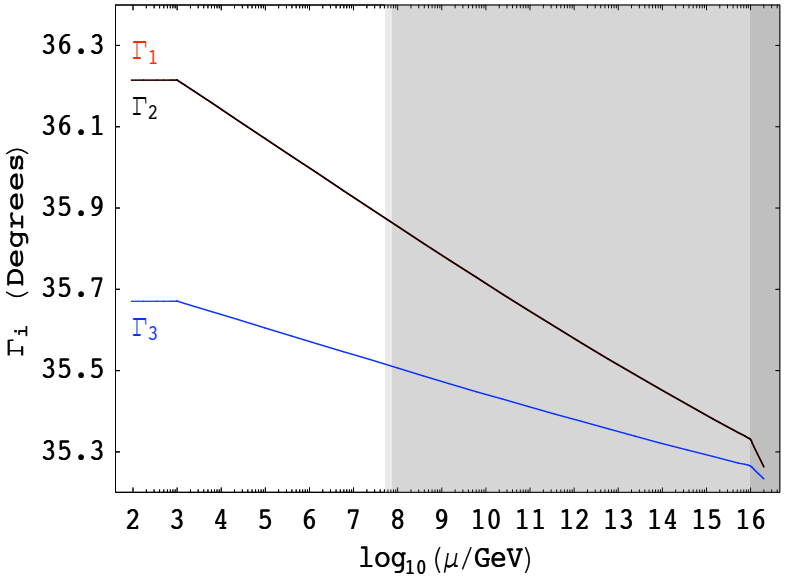

FIGURE 4.3: Evolution of sum rules Γ_1,Γ_2, Γ_3 for Cabibbo-like charged lepton corrections at $\theta_{12}^E = 8\,^\circ$ and $\lambda_{12}^E = 0\,^\circ$. This is achieved for large $\tan(\beta) = 50$.

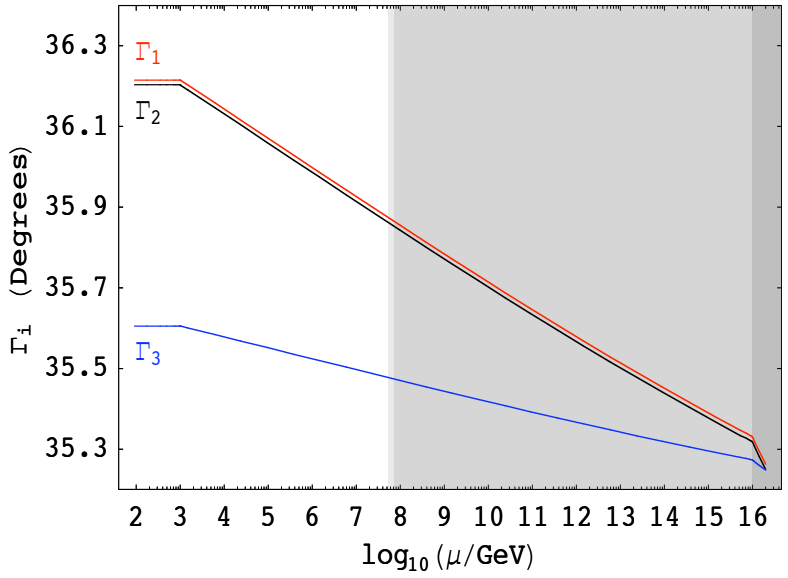

FIGURE 4.4: Evolution of sum rules Γ_1,Γ_2, Γ_3 for Cabibbo-like charged lepton corrections at $\theta_{12}^E = 5\,^\circ$ and $\lambda_{12}^E = 15\,^\circ$. This is achieved for large $\tan(\beta) = 50$.

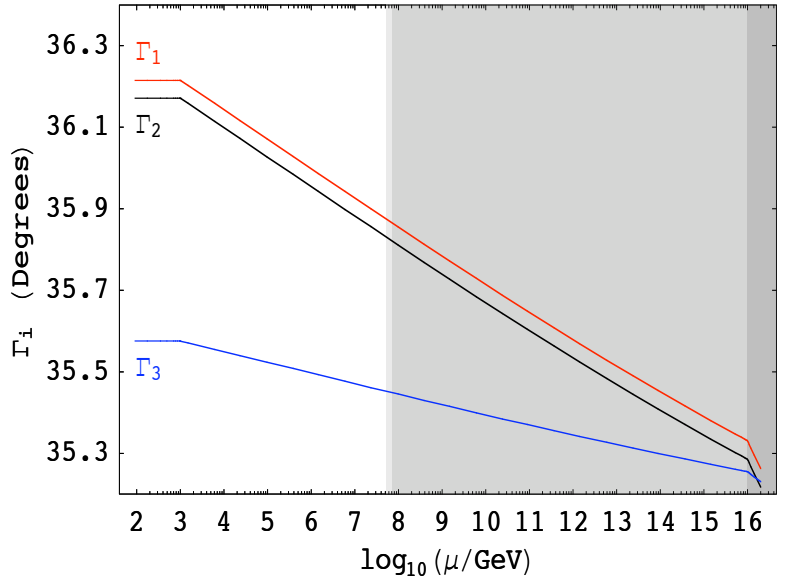

FIGURE 4.5: Evolution of sum rules Γ_1,Γ_2, Γ_3 for Cabibbo-like charged lepton corrections at $\theta_{12}^E = 5\,^\circ$ and $\lambda_{12}^E = 30\,^\circ$. This is achieved for large $\tan(\beta) = 50$.

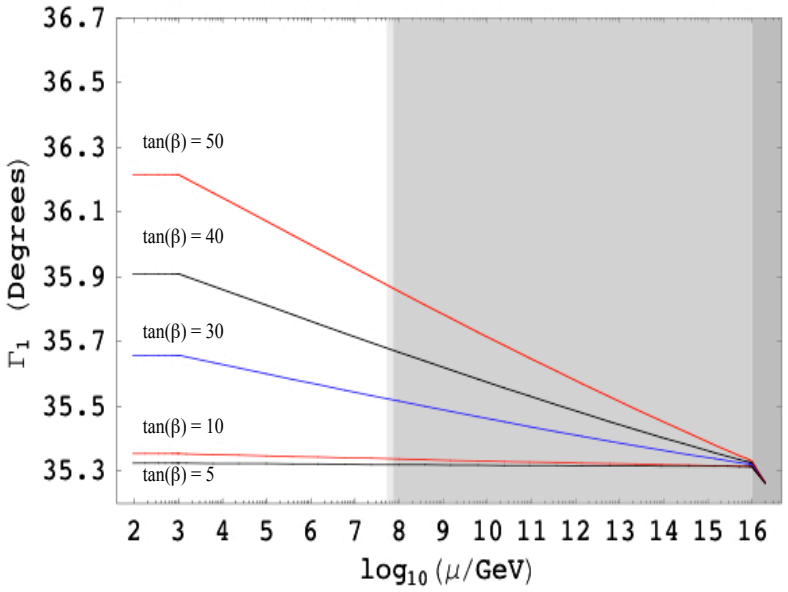

FIGURE 4.6: Evolution of the sum rule Γ_1 for Cabibbo-like charged lepton corrections for various values of $\tan(\beta)$. The running is at $\theta_{12}^E = 5\,^\circ$ and $\lambda_{12}^E = 0\,^\circ$. Note the expanded (and different) vertical scales used in this figure; in all cases of $\tan(\beta)$, the corrections are less than one degree.

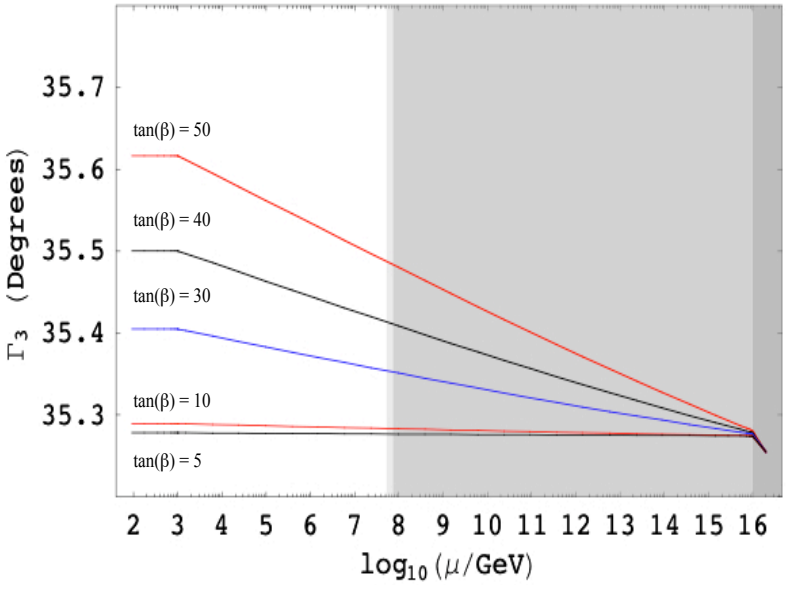

FIGURE 4.7: Evolution of the sum rule Γ_3 for Cabibbo-like charged lepton corrections for various values of $\tan(\beta)$. The running is at $\theta_{12}^E = 5\,^\circ$ and $\lambda_{12}^E = 0\,^\circ$.

4.2.1.2 Sum rules in terms of TB deviation parameters

In this subsection, for completeness we study the evolution of the TB deviation parameters defined in Eq.(2.18). Their RG evolution, for different values of θ_{12}^E, is shown in Figs.(4.8,4.9). In Figs.(4.10,4.11) we display the evolution of the sum rules given by Eqs.(2.37, 2.38). From Figs.(4.10,4.11), it is seen that both σ_1, σ_2 are precisely equal to zero at the GUT scale for $\theta_{12}^E = 0$ but differ by a tiny amount for $\theta_{12}^E, \lambda_{12}^E \neq 0$. In this numerical example it is apparent that the sum rule σ_2 is slightly more stable than the original sum rule σ_1, although there is not much more stability. This is a manifestation of the fact that σ_2 does not take into account the running of r, which introduces an effect coming from the Majorana phases which we have assumed to be zero in this example. Later on we shall discuss a numerical example with non-zero Majorana phases where the enhanced stability of σ_2 will be more pronounced.

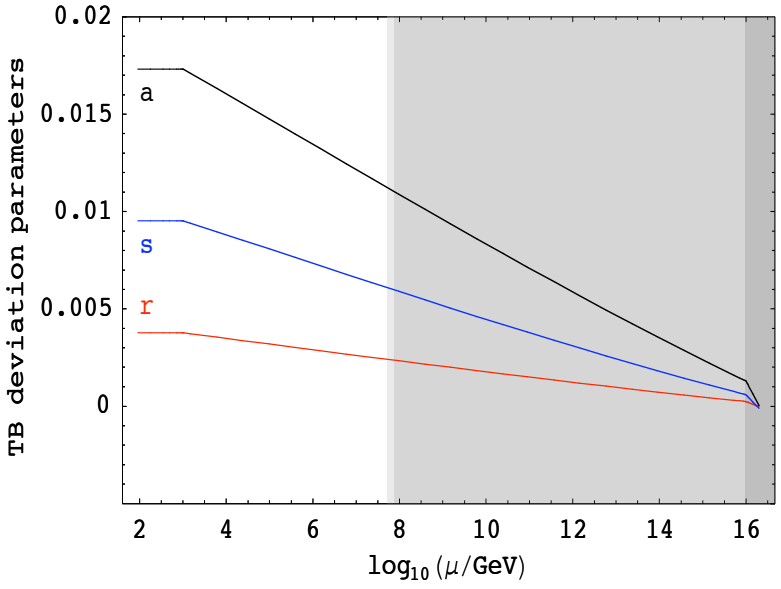

FIGURE 4.8: Evolution of the deviation parameters r, s, a from the GUT scale to the electroweak scale, in the absence of charged lepton corrections, for large $\tan(\beta) = 50$.

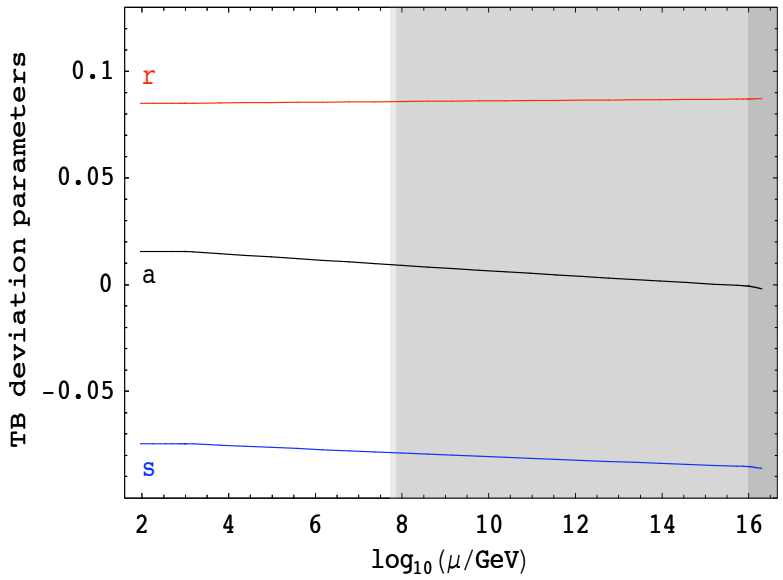

FIGURE 4.9: Evolution of the deviation parameters r, s, a from the GUT scale to the electroweak scale, in the presence of Cabibbo-like charged lepton corrections, for large $\tan(\beta) = 50$. The values of charged lepton parameters are: $\theta_{12}^E = 5\,^\circ$ and $\lambda_{12}^E = 15\,^\circ$.

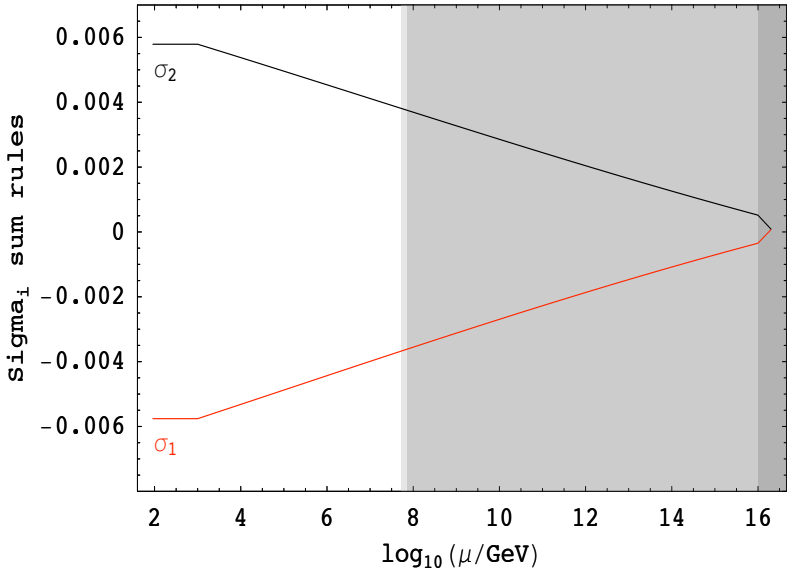

FIGURE 4.10: Evolution of the sum rules σ_1 and σ_2 from the GUT scale to the electroweak scale, in the absence of charged lepton corrections ($\theta_{12}^E = 0\,^\circ$ and $\lambda_{12}^E = 0\,^\circ$), for large $\tan(\beta) = 50$.

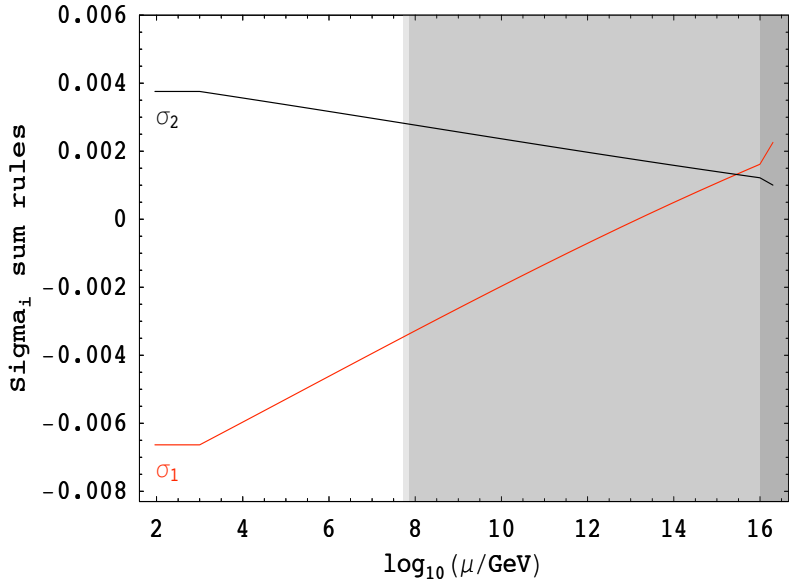

FIGURE 4.11: Evolution of the sum rules σ_1 and σ_2 from the GUT scale to the electroweak scale, in the presence of Cabibbo-like charged lepton corrections, for large $\tan(\beta) = 50$. The values of charged lepton parameters are: $\theta_{12}^E = 5\,^\circ$ and $\lambda_{12}^E = 30\,^\circ$.

4.2.2 Sum rules with more general charged lepton corrections including θ_{23}^E

Finally in this subsection we study the evolution of the ξ_i parameters for the case of charged lepton corrections of the more general form in Eq.(4.4). In Fig.(4.12), we show the RG running of the parameters ξ_1, ξ_2 and ξ_3, given in terms of the mixing angles in Eq.(2.34), for the case of Cabibbo-like charged lepton corrections. As expected, for Cabibbo-like charged lepton corrections, these parameters are exactly zero at the GUT scale for all values of θ_{12}^E and λ_{12}^E, but then diverge from zero due to the RG corrections. In Fig.(4.13), we now switch on the non-Cabibbo-like charged lepton corrections by a small amount corresponding to $\theta_{23}^E = 2\,^\circ$. In this case we see that the parameters ξ_1, ξ_2 and ξ_3 are all non zero at the GUT scale and deviate even more at low energies due to RG running.

In Figs.(4.14,4.15), we show the running of the TB deviation parameters and the sum rules σ_1 and σ_2 for the non-Cabibbo-like case with $\theta_{23}^E = 2\,^\circ$. It is clear from Fig.(4.15) that the σ_1 sum rule is still valid at the GUT scale even for a non-zero θ_{23}, as remarked earlier.

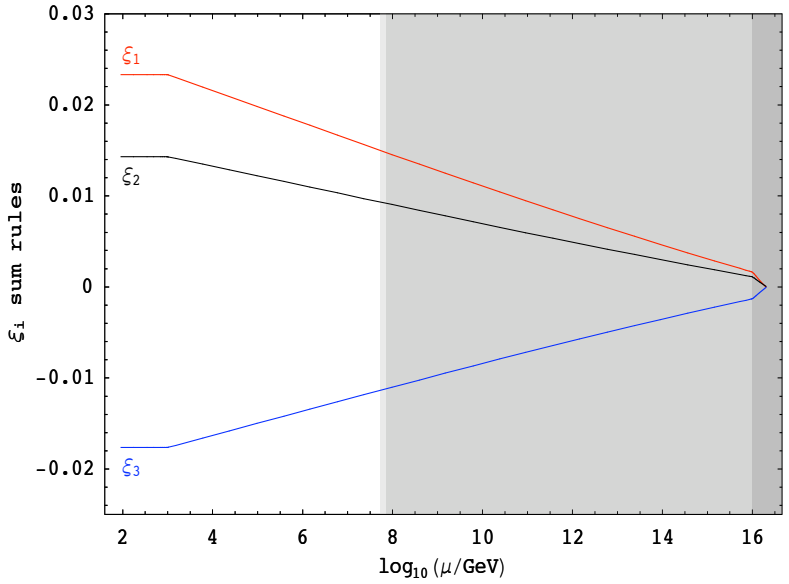

FIGURE 4.12: Evolution of the third row deviation parameters ξ_1, ξ_2 and ξ_3 from the GUT scale to the electroweak scale, in the presence of Cabibbo-like charged lepton corrections with $\theta_{12}^E = 5\,^\circ$ and $\lambda_{12}^E = 30\,^\circ$, for large $\tan(\beta) = 50$.

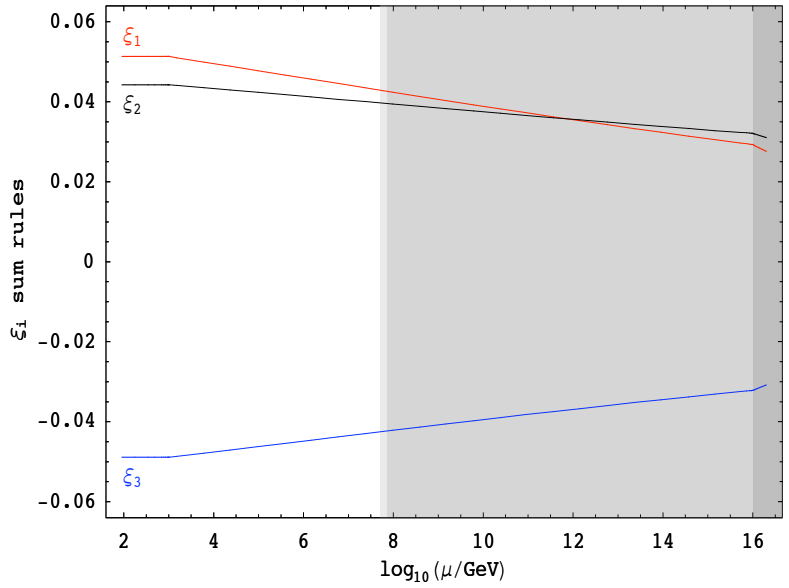

FIGURE 4.13: Evolution of the third row deviation parameters ξ_1, ξ_2 and ξ_3 from the GUT scale to the electroweak scale, in the presence of more general charged lepton corrections with $\theta_{12}^E = 5\,^\circ$ and $\lambda_{12}^E = 30\,^\circ$, $\theta_{23}^E = 2\,^\circ$ and $\lambda_{23}^E = 30\,^\circ$, for large $\tan(\beta) = 50$.

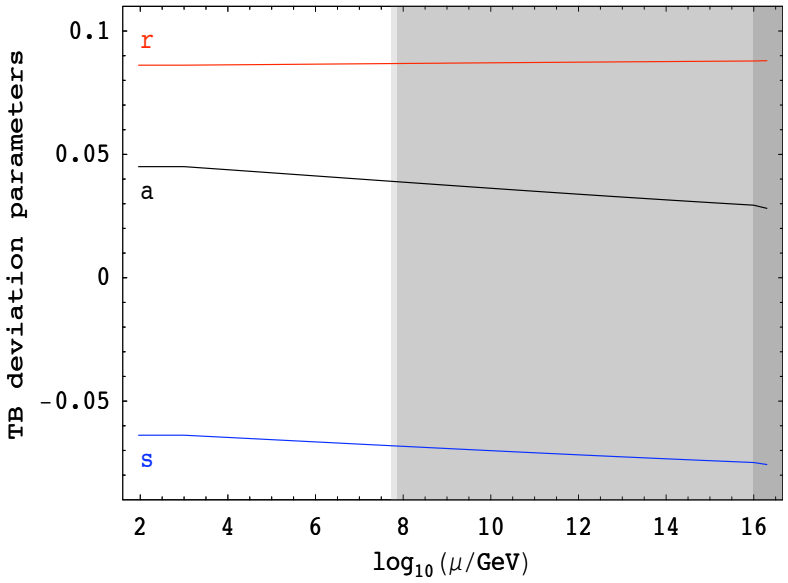

FIGURE 4.14: Running of the TB deviation parameters r, a and s, from the GUT scale to the electroweak scale, in the presence more general charged lepton corrections with $\theta_{12}^E = 5\,^\circ$, $\lambda_{12}^E = 30\,^\circ$, $\lambda_{23}^E = 30\,^\circ$, $\theta_{23}^E = 2\,^\circ$, for large $\tan(\beta) = 50$.

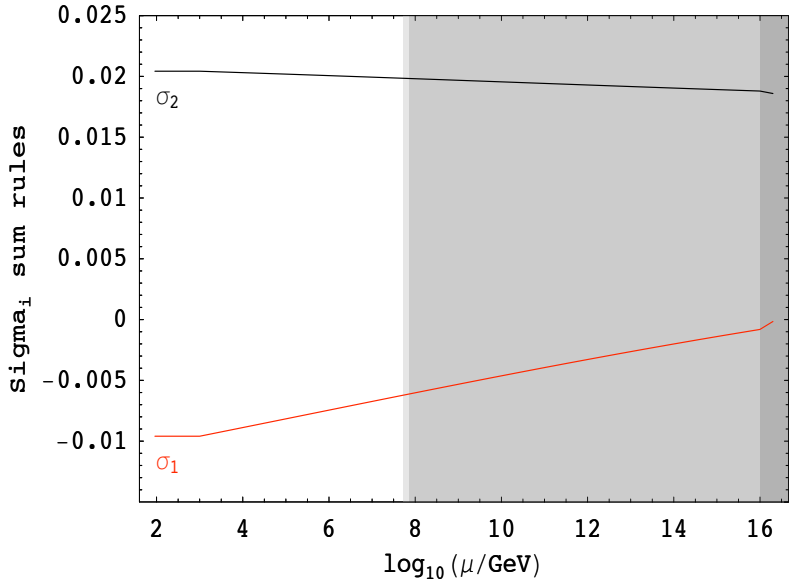

FIGURE 4.15: Running of the sum rules σ_1, σ_2, from the GUT scale to the electroweak scale, in the presence more general charged lepton corrections with $\theta_{12}^E = 5\,^\circ$, $\lambda_{12}^E = 30\,^\circ$, $\lambda_{23}^E = 30\,^\circ$, $\theta_{23}^E = 2\,^\circ$, for large $\tan(\beta) = 50$. Note that $\sigma_1 = 0$ at the GUT scale even in the presence of the more general charged lepton corrections.

4.3 RG running with non-zero Majorana phases

So far we have presented results for a particular example with zero Majorana phases. In this section, we present the running of the σ_i sum rules and the TB deviation parameters where the neutrino Yukawa matrix is taken to be similar to Eq.(4.2) with the same values for $|b|$, $|e|$ and c_3 but with non- zero Majorana phases (δ_1, δ_2),

$$Y^{\nu}_{LR} = \begin{pmatrix} 0 & 0.97282be^{i\delta_2} & 0.001 \\ ee^{i\delta_1} & be^{i\delta_2} & 0 \\ -1.012ee^{i\delta_1} & be^{i\delta_2} & c_3 \end{pmatrix} \tag{4.6}$$

where we shall take the values of the phases δ_1 and δ_2 to be $120^o, 60^o$ respectively. We take the right-handed Majorana mass matrix to be the same as the one given in Eq.(4.1). The numerical value of the Yukawa couplings has been changed slightly to compensate for the non-zero phases in order to once again yield exact tri-bimaximal neutrino mixing at the GUT scale. This was done by changing the corrections in the 12 and 31 elements of the above neutrino Yukawa matrix compared to those given in Eq.(4.2).

In Figs.(4.16,4.17), we show results for the running of the sum rules σ_i and for the deviation parameters r, a, s for the above example with non-zero Majorana phases. In this example the σ_2 sum rule is much more stable than σ_1 as clearly shown in Fig.(4.16). This shows that the question of the stability of the sum rule σ_2 is dependent on the choice of Majorana phases via the running of r. In particular with this choice of Majorana phases the deviation parameters s, a and r all run less as shown in Fig.(4.17), compared to the previous case with zero phases Fig.(4.8).

The Γ_i and ξ_i sum rules also change with the Majorana phases turned on but not as much as σ_i sum rules. For instance, at $\theta^E_{12} = 5^o$ and $\lambda^E_{12} = 0^o$, we find that Γ_1 and Γ_2 get smaller by 0.05 degrees at the M_Z scale compared to the case where the phases are zero. Γ_3 on the other hand gets larger by about 0.1 degrees. At $\theta^E_{12} = 5^o$ and $\lambda^E_{12} = 30^o$, ξ_1 and ξ_2 get smaller by about 0.001 to 0.003 compared to the zero phases case whereas ξ_3 gets larger by 0.006.

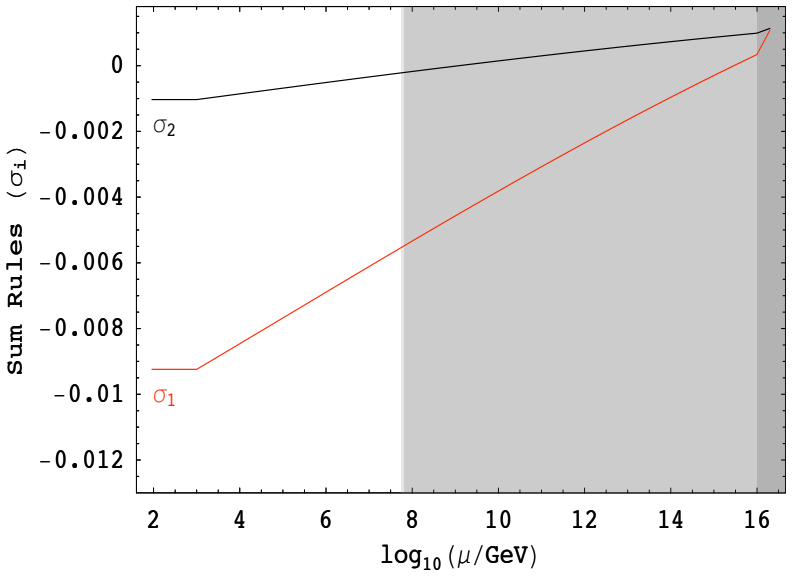

FIGURE 4.16: Running of the sum rules σ_1, σ_2, from the GUT scale to the electroweak scale, in the presence of non zero Majorana phases ($\delta_1 = 120^o$ and $\delta_2 = 60^o$). The running is performed, without charged lepton corrections ($\theta_{12}^E = 0\,^\circ$, $\lambda_{12}^E = 0\,^\circ$), at $\tan(\beta) = 50$.

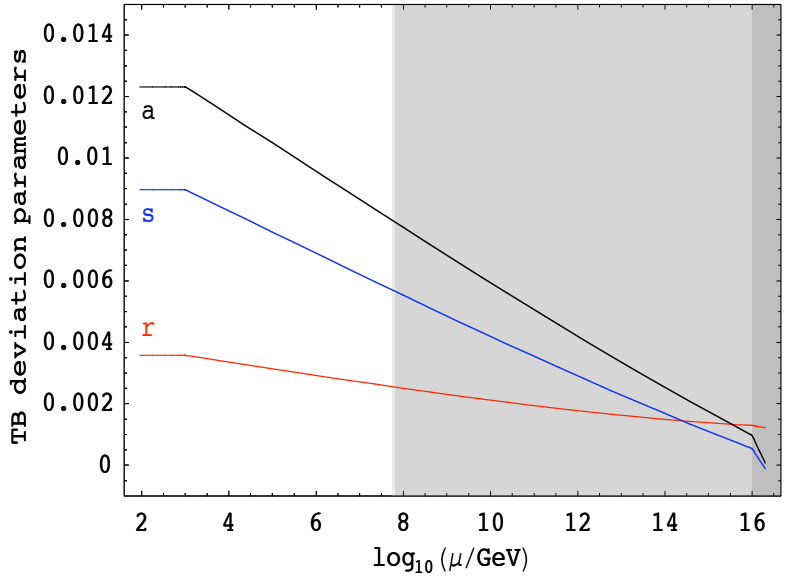

FIGURE 4.17: Running of the TB deviation parameters (r, a, s), from the GUT scale to the electroweak scale, in the presence of non zero Majorana phases ($\delta_1 = 120^o$ and $\delta_2 = 60^o$). The running is performed, without charged lepton corrections ($\theta_{12}^E = 0\,^\circ$, $\lambda_{12}^E = 0\,^\circ$), at $\tan(\beta) = 50$.

4.4 RG running with heavy sequential dominance

So far all the numerical results have been based on a particular example inspired by the models of [7, 10], namely the case where the GUT scale neutrino Yukawa matrix has the form in Eq.(4.2), or the closely related form in Eq.(4.6) with non-zero Majorana phases. In these examples the dominant contribution to atmospheric neutrino mass is coming from the lightest right-handed neutrino via the see-saw mechanism, a situation known as light sequential dominance (LSD) [42, 43]. In order to test the generality of the results in this section we consider a quite different example in which the dominant contribution to the atmospheric neutrino mass is coming from the heaviest right-handed neutrino via the see-saw mechanism, a situation known as heavy sequential dominance (HSD) [42, 43]. This example is chosen since it the most qualitatively different to the example of LSD considered previously, yet despite this we shall see that the numerical results for the corrections to TB mixing are qualitatively similar to those encountered previously. This gives us some confidence that our results and conclusions are not restricted to the particular numerical example studied but are in fact applicable to a large class of see-saw models based on hierarchical neutrino masses.

In the HSD example considered here the right handed neutrino Majorana matrix as well as the neutrino Yukawa matrix are given by the following equations:

$$M_{RR} = \begin{pmatrix} 3.991 \times 10^{-6} & 0 & 0 \\ 0 & 5.800 \times 10^{-4} & 0 \\ 0 & 0 & 5.021 \end{pmatrix} M_3,$$

where $M_3 = 10^{14} GeV$. Ignoring RGE corrections to begin with, we find that precise tri-bimaximal neutrino mixing at the GUT scale ($\theta^{\nu}_{12} = 35.26\,^{\circ}$, $\theta^{\nu}_{23} = 45.00\,^{\circ}$, $\theta^{\nu}_{13} = 0.00\,^{\circ}$) can be achieved with the Yukawa matrix:

$$Y^{\nu}_{LR} = \begin{pmatrix} 1.001 \times 10^{-7} & 1.0036\, b & 0 \\ 0 & b & -1.0013\, e \\ 2.992 \times 10^{-5} & b & e \end{pmatrix} \tag{4.7}$$

where $b = 2.401 \times 10^{-3}$, $e = 0.677$. These parameters also lead to the following values for the neutrino masses: $\Delta m^2_{atm} = 2.47 \times 10^{-3} eV^2$ and $\Delta m^2_{sol} = 7.53 \times 10^{-5} eV^2$ which are well within the allowed experimental ranges.

Note that in the case of HSD the Yukawa couplings present in the neutrino Yukawa matrix are larger than the previous case especially e which we take to be 0.677

compared to 2.125×10^{-4} in the previous example. Furthermore there are similarly two large Yukawa couplings in the third column of the Yukawa matrix. Moreover the heaviest RH neutrino associated with these large Yukawa couplings has a mass well below the GUT scale leading larger threshold corrections coming from it.

We assume charged lepton corrections of the form of Eq.(2.24), the neutrino Yukawa matrix in the non-diagonal charged lepton basis is then transformed to the diagonal charged lepton basis according to Eq.(4.3). Using the REAP package, the running of Γ_i sum rules was performed from the GUT scale to low energy scale and the results are shown in Figs.(4.18, 4.19, 4.20). From the Figs.(4.18) we can see that, despite the larger threshold corrections, for $\tan(\beta) = 50$, the RG running of Γ_3 is still small (about 0.4^o) whereas that of Γ_1 and Γ_2 is about 1.3^o, compared to the results shown in Fig.(4.2) (nearly 1^o). This suggests that, qualitatively, the results obtained for the previous numerical example inspired by the GUT models in [7, 10] are expected to have wide applicability beyond the specific example considered. Figs.(4.19, 4.20) show the running of the sum rules Γ_1, Γ_3 at different values of $\tan(\beta)$. Similar to the previous model, we see that the RG corrections for these sum rules, at the M_Z scale, get smaller with smaller values of $\tan(\beta)$.

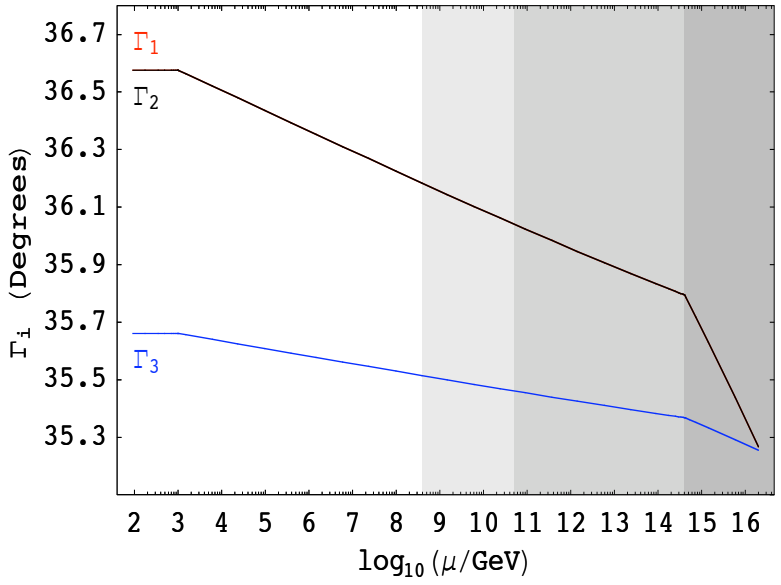

FIGURE 4.18: Running of the sum rules Γ_i, from the GUT scale to the electroweak scale, in the case of heavy sequential dominance. The running was performed, for the case of Cabibbo-like charged lepton corrections ($\theta_{12}^E = 5\,^\circ$, $\lambda_{12}^E = 0\,^\circ$), at $\tan(\beta) = 50$.

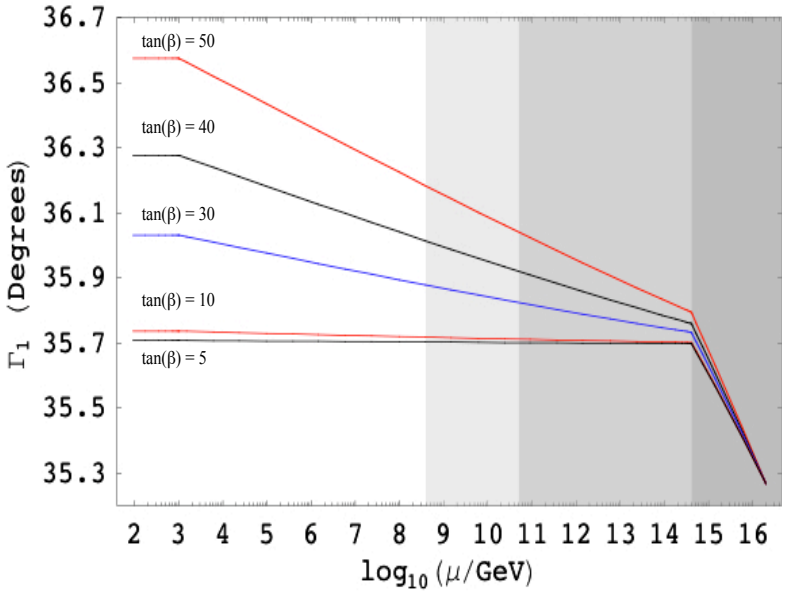

FIGURE 4.19: Evolution of the sum rule Γ_1, from the GUT scale to the electroweak scale, in the case of heavy sequential dominance. The running was performed, for various values of $\tan(\beta)$, for the case of Cabibbo-like charged lepton corrections with $\theta_{12}^E = 5\,^\circ$ and $\lambda_{12}^E = 0\,^\circ$.

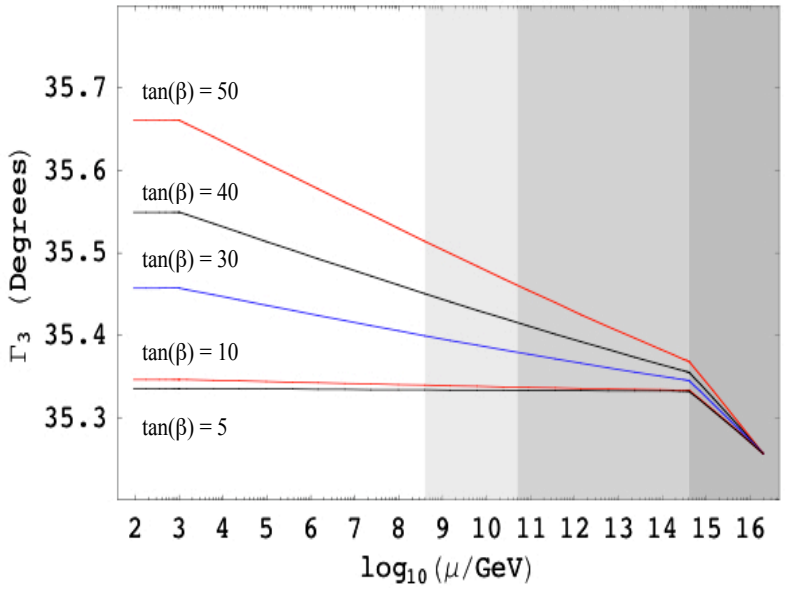

FIGURE 4.20: Evolution of the sum rule Γ_3, from the GUT scale to the electroweak scale, in the case of heavy sequential dominance. The running was performed, for various values of $\tan(\beta)$, for the case of Cabibbo-like charged lepton corrections with $\theta_{12}^E = 5\,^\circ$ and $\lambda_{12}^E = 0\,^\circ$.

4.5 Analytic approach to RG running

So far, all the results presented in this chapter have been based on a numerical evaluation of the RG corrections using the REAP package. In order to investigate the quantitative accuracy of the analytic approach, we shall compare the analytic estimates of the RG effects for the LSD example presented in Section.4.1. For this purpose it is sufficient to switch off the charged lepton corrections and study the RG corrections to the neutrino mixing angles using the analytic approximations in [16] which we then compare to the numerical results we obtained earlier in this chapter, and which we also summarize here for convenience. In order to estimate the RG corrections to the mixing angles, following [16] it is assumed that the (3,3) matrix elements govern both the charged Yukawa matrix (Y^e) and the neutrino Yukawa matrix $(Y^\nu)^2$ in the flavour basis in which the charged lepton mass matrix is diagonal. Taking $Y^e \approx diag(0,0,y_\tau)$ and $Y^\nu \approx diag(0,0,y_{\nu_3})$, one finds, to leading log approximation, that there is a single parameter which governs the RG corrections to all the mixing angles given by [37, 38]:

$$\eta^{RG} = \frac{y_\tau^2}{8\pi^2}\ln\frac{M_{GUT}}{M_Z} + \frac{y_{\nu_3}^2}{8\pi^2}\ln\frac{M_{GUT}}{M_3}. \tag{4.8}$$

Assuming tri-bimaximal neutrino mixing at the GUT scale, the low energy scale parameters are then given approximately by:

$$s^\nu_{12}(M_Z) = \frac{1}{\sqrt{3}}(1+\frac{\eta^{RG}}{6}) \ , \ s^\nu_{23}(M_Z) = \frac{1}{\sqrt{2}}(1+\frac{\eta^{RG}}{4}) \ , \ s^\nu_{13}(M_Z) = \frac{\eta^{RG}}{3}\frac{m_2}{m_3}. \tag{4.9}$$

We now apply the above analytic formalism to the LSD model defined in section.4.1, and subsequently studied numerically in the earlier sections of this chapter. In this model from Eq.(4.2) we see that $y_{\nu_3} = c_3 \approx 0.58$ at the GUT scale. We also find $y_\tau = 0.33$ and the mass ratio $m_2/m_3 = 0.16$ for the case $\tan(\beta) = 50$. Using these values, the mixing angles and the quantities (Γ_i) can be estimated as presented in Tab.(4.6), where the analytic estimates are shown alongside the numerical results for comparison.

It is interesting to compare the analytic results of the neutrino mixing angles and sum rules at the M_Z scale to the numerical ones in Tab.(4.6), assuming that they take the precise TB mixing values at the GUT scale and setting all charged lepton corrections to zero, for the LSD model described above. The results show that

[2]We have already noted that for some models such as HSD this is not the case for the neutrino Yukawa matrix.

Parameter	θ_{12}^{ν}	θ_{23}^{ν}	θ_{13}^{ν}	Γ_1	Γ_2	Γ_3
Analytic (^{o})	35.59	45.69	0.15	35.94	35.94	35.44
Numerical (^{o})	35.65	46.00	0.15	36.21	36.21	35.49

TABLE 4.6: A comparison between the analytic and numerical results for the RG corrections to neutrino mixing angles at the M_Z scale, assuming that they take the precise TB mixing values at the GUT scale, for the LSD model described in the body of the chapter with $\tan(\beta) = 50$.

the numerical estimate of θ_{13}^{ν} (which is equal to zero at the GUT scale) is very accurately reproduced by the analytic approximation (indeed there is no difference to 2 d.p.), and the RG correction to θ_{12}^{ν} is also well reproduced with the analytic estimate underestimating the correction by only 0.06 degrees. However the results also show that there is a significant underestimate of θ_{23}^{ν} with the analytically estimated value at the M_Z scale being less than the numerical value by about 0.3 degrees, resulting in the analytically estimated values for Γ_1 and Γ_2 being less than the numerical values by about the same amount (0.3^o). From the point of view of the effects studied so far in this chapter (for example, note the precision of the scales shown in the results in Fig.(4.2)), an error of 0.3^o is undesirable and therefore we would not wish to compromise the numerical results by being subject to such unnecessary errors incurred when considering the analytic approach.

We remark that the origin of the discrepancy between the analytic estimates, calculated in this section, and the numerical results, for the cases where the analytic approach is reliable and applicable, is due to the fact that the analytic estimates are based on the assumption that the Yukawa couplings y_τ and y_{ν_3} are fixed at their GUT scale values and do not run, whereas the numerical results allow for the co-running of all the Yukawa couplings in the matrix (including the second family Yukawa couplings), with the leading logs being effectively re-summed.

After calculating the analytic estimates of the RG corrections to the neutrino mixing angles and sum rules, for the LSD model presented in Section.4.1, we shall now summarise the reasons why we have chosen to study these corrections numerically, rather than using the analytic estimates presented in [16]:

The first reason we follow the numerical approach is that, as we showed earlier, some analytic estimates of RG effects which have ignored the effects of phases are unreliable. For example, the main purpose of the work, presented in this chapter, is to find out precisely how large the RG corrections are to sum rule relations which have been proposed in the literature as presented in Section.2.8. Although the RG corrections to such sum rules are expected to be small, they are certainly

not negligible compared to the expected precision of future neutrino experiments, and indeed this prompted the introduction of the modified sum rule in Eq.(2.38), where the extra term compared to Eq.(2.37) was supposed to take into account the RG corrections [37, 38]. However, it turns out that the new analytic term, which ignores the effects of phases, is too simplistic. Indeed the numerical results in Figs.(4.10, 4.16) clearly show that the extra term included in the analytic estimate of the RG correction in Eq.(2.38) does not capture the phase dependence of the RG correction to the original sum rule in Eq.(2.37). The numerical study in this chapter has highlighted the shortcoming of analytic estimates of the RG corrections to sum rules which do not include the phase dependence.

The second reason we follow the numerical approach, rather than an analytic approach, is that for some of the cases studied the analytic approach is simply not applicable. The usual analytic approach is based on the assumption that only the third family charged lepton and neutrino Yukawa couplings are taken into account (while many analytic studies ignore neutrino Yukawa couplings and threshold effects altogether). Whilst the approximation of keeping only third family Yukawa couplings is sufficient for some models, for example the LSD class of models, it is certainly not sufficient for all classes of models. For example the HSD case that we also study involves two large neutrino Yukawa couplings, and the analytic estimates in [37, 38] do not directly apply to this case.

The third reason for following a numerical approach is a purely quantitative one, namely, even for the cases where the analytic approach is reliable and applicable (and we have already seen examples in the previous two paragraphs when it is neither) we would like to obtain the best possible estimate of the RG corrections which are the main focus of this work. If the sum rules are to be confronted with experiment, it is important to have a reliable quantitative handle on the RG corrections, and for this purpose it is necessary to go beyond the leading log analytic approximation presented earlier in this section.

4.6 Summary

In this chapter, we have analyzed the effects of charged lepton corrections and RG running on the low energy predictions of theories which accurately predict tribimaximal neutrino mixing at the high energy scale. In GUT motivated examples the charged lepton corrections are often Cabibbo-like and in this case the effect of charged lepton corrections leads to a range of neutrino mixing sum rules at the

GUT scale, given by the Γ_i sum rules in Eqs.(2.30,2.31,2.32), as well as the σ_i sum rules expressed in terms of the deviation parameters in Eqs.(2.37, 2.38). We have studied the RG running of such sum rules numerically for a specific numerical example inspired by the GUT models in [7, 10], corresponding closely to CSD with LSD. Our results indicate small but measurable effects for the two examples studied. For example the Γ_3 sum rule which at the GUT scale corresponds to $\theta_{12} - \theta_{13}\cos(\delta) \approx 35.3^o$ becomes renormalized by about 0.4^o even for large $\tan\beta = 50$. We have also considered the effect on charged lepton corrections coming from non-Cabibbo-like charged lepton corrections (due to non-zero θ_{23}^E) and confirmed that the sum rule σ_1 is insensitive to θ_{23}^E.

Even for a particular class of numerical model, such as the GUT-flavour inspired LSD model considered, the numerical results will depend in general on the choice of Majorana phases for that model. We have seen that switching on these Majorana phases can alter significantly the running of the TB mixing deviation parameters r, s, a as well as the sum rules such as σ_i. For example the sum rule σ_2 which includes the leading logarithmic RG corrections due to the running of s and a, will have a Majorana phase dependence via the running of r which was neglected in the derivation of σ_2 [37]. Thus, the relative stability of σ_2 as compared to σ_1 turns out to be a Majorana phase dependent question.

Although most of the numerical results are based on a particular GUT-flavour motivated LSD type of model, we have also considered similar results for a completely different type of model based on HSD. Overall we have found that the RG running effects are quite small in both cases which suggests that qualitatively similar results will apply to other models based on the Minimal Supersymmetric Standard Model, extended to include the see-saw mechanism, with hierarchical neutrino masses. These corrections, although small, they will nevertheless be important when comparing the neutrino mixing sum rules to the results of future high precision neutrino oscillation experiments [50].

Part II

Moduli Stabilisation and Inflation

Chapter 5

String Compactifications: An Overview

In this chapter, we present a brief, nontechnical, review of string compactifications, extra dimensions and moduli stabilisation. There are many excellent reviews that discuss this subject extensively [51, 52, 53, 54, 55].

5.1 String theory

String theory is very attractive as it represents to date the only consistent framework for unifying the Standard Model and gravity. It assumes that everything in nature is made of one dimensional objects known as strings which can be either closed as a loop or open with their ends attached to other extended objects (branes). This means that in quantum field theory (QFT), all fields including scalars, fermions and gauge bosons can be described as different vibrational modes of these strings.

There are five known string theories in ten space-time dimensions [56]: type I, type IIA, type IIB. heterotic $E_8 \times E_8$ and heterotic $SO(32)$. Identifying the spectrum of string theory is a complex subject. Here, we list the main fields for closed strings which are the metric G_{MN}, the dilaton ϕ, and the anti-symmetric tensor B_{MN}. The five string theories are all limits of an eleven dimensional theory known as M-theory. This theory contains other dimensional extended objects called branes or membranes. In certain limits, M-theory can be related to a particular type of string theory by compactifying one dimension of space to get a ten dimensional

theory. For instance, taking one of the space dimensions to be in the shape of a circle, the theory becomes equivalent to type IIA string theory where the size of the circle plays the role of string coupling (the dilaton). Another compactification of M-theory, which yields Heterotic $E_8 \times E_8$ in ten dimensions, is achieved by taking the circle to have a Z_2 symmetry. This is a simple illustration of the idea of compactifying space dimensions in order to go from higher to lower dimensional theories. There are also dualities which connect all string theories together, and these are namely T, S and U duality. The existence of these dualities between different types of string theory is very important in model building, particularly when certain calculations in one theory are cumbersome. In such cases, one can perform equivalent calculations in another string limit, then transform the calculations back to the more difficult limit of the relevant theory. All string theories are described at low energy by effective Supergravity theories.

In order to obtain the correct phenomenology in four dimensions, string theories are preferred to have $\mathcal{N} = 1$ Supersymmetry in ten dimensions. Supersymmetry is a non-trivial extension of the known symmetries of space and time (which are described in special relativity by the Poincaré group). In model building, there are various reasons why one should focus on theories with low energy $\mathcal{N} = 1$ Supersymmetry. An important reason is that it gives rise to other extensions of the Standard Model (SM) which would solve some of its shortcomings; for example, the gauge hierarchy problem. One of these extensions is the Minimal Supersymmetric Standard Model (MSSM) which embeds the SM within a supersymmetric theory.

Looking at string theory, we find that heterotic and type I theories possess $\mathcal{N} = 1$ Supesymmetry in ten dimensions and contain a large number of gauge groups. Therefore, these theories are good candidates for model building and they can easily accommodate the ingredients of the SM. On the other hand, Type II theories seem to have $\mathcal{N} = 2$ Supersymmetry in ten dimensions and very small gauge groups. This poses a problem when trying to establish a four dimensional theory starting from these theories. To generate the correct phenomenology at four dimensions, we need to find a mechanism that breaks $\mathcal{N} = 2$ to $\mathcal{N} = 1$ Supersymmetry.

The study of type II theories was revolutionised after the discovery of Dirichlet-branes (D-branes)[57, 58]. These are extended objects that exist within the vacua of these theories. The ends of the open strings are usually attached to the surfaces of the branes while the closed strings, which are usually identified with gravity fields, are free to move in ten dimensional space-time without necessarily being

attached to branes. The dimension of a particular brane is related to the states of the relevant theory that couples to it and we usually refer to a brane with its space dimension as D_p brane. We also refer to it as a $(p+1)$-sub manifold of the full space-time manifold in ten dimensions. This subject is not within the scope of this thesis and, therefore, will not be discussed any further. We refer the reader to the reviews [57, 58]

5.2 String compactifications

String theories are leading candidates for the unification of the SM with gravity. However, they all exist in high dimensions that we cannot observe in our four dimensional universe. This means that, in order to compare the physics of these theories to our universe, we need to find a way of hiding the extra dimensions so that we can only see the four dimensions required by our universe. This is known as compactification of space dimensions. Compactification means that the extra dimensions are curled up with a very small radius (much smaller than the lengths observed by high energy experiments). Compactifying the six extra dimensions of string theories (these become seven when considering compactifications of M-theory), we eventually get a four dimensional theory as required by phenomenology.

The idea of compactification is not a new one, it was first realised by Kaluza and Klein [59, 60] where they introduced a fifth dimension, invisible in everyday life. This gives a generalisation of general relativity to five dimensions. Before we move on to string compactifications and their implications, let us first briefly review Kaluza Klein reduction.

5.2.1 Kaluza Klein reduction

Kaluza Klein reduction [59, 60] represents the simplest type of compactification. In order to review it, let us start by writing the action of Einstein-Hilbert space in five dimensions (five dimensional gravity) as,

$$S = -\int_{\mathcal{M}} d^5X\sqrt{-\hat{g}}\hat{R}, \tag{5.1}$$

where $\hat{R}$ is the five dimensional Ricci scalar. The five dimensional metric is $\hat{g}_{MN}$ with indices $M, N = 0, 1, 2, 3, 4$. We consider the vacuum of this theory where

the five dimensional space M can be written as a product of the four dimensional space M_4, with 4 dimensional coordinates x^μ where $\{\mu = 0, 1, 2, 3\}$, and a fifth dimension y. The decomposition of the five dimensional metric can be written as

$$\langle \hat{g}_{MN} \rangle dX^M dX^N = \langle g_{\mu\nu} \rangle dx^\mu dx^\nu + \langle g_{55} \rangle dy dy \tag{5.2}$$

where the quantities are written in terms of their vacuum expectation values and $g^{\mu\nu}$ is the metric in four space-time dimensions.

We solve the Einstein equation $\hat{R}_{MN} = 0$ in order to see whether the theory admits such compactification. The solutions are $g_{\mu\nu} = \eta_{\mu\nu}$ and $g_{55} = 1$.

The fields $\phi(x, y)$, which result by taking fluctuations about the vacuum of the theory, can be written as a Fourier expansion in terms of the radius of the extra dimension R. We take this extra dimension to be compact and periodic $y \in [0, 2\pi R]$. The fields $\phi(x, y)$ can then be written as,

$$\phi(x, y) = \frac{1}{\sqrt{2\pi R}} \sum_{n=-\infty}^{+\infty} \phi_n(x) e^{iny/R}, \tag{5.3}$$

The field ϕ satisfies the five dimensional equation of motion given by,

$$\partial_\mu \partial^\mu \phi + \partial_y^2 \phi = 0. \tag{5.4}$$

Substituting Eq.(5.3) in Eq.(5.4), we get

$$\sum_{n=-\infty}^{+\infty} \left(\partial_\mu \partial^\mu - \frac{n^2}{R^2} \right) \phi_n = 0. \tag{5.5}$$

Taking the radius of the circle to be very small, we recover one massless scalar field, ϕ_0, and many excited fields with high masses, n/R. To specify an effective theory, we consider the limit where the radius R vanishes, where we only keep the massless field and truncate the other heavy modes (Kaluza- Klein modes). This procedure is known as dimensional reduction and it can be generalised to the case of six or seven extra dimensions. In such cases, a manifold of extra dimensions is integrated out to leave an effective four dimensional theory. Kaluza-Klein reduction leads to a four dimensional theory with the metric $g_{\mu\nu}$, a gauge field A_μ and a scalar field ϕ. the action of this theory is written as

$$S_{4d} = \int_S d^4x \sqrt{-g} \left(R - \frac{1}{4} \phi_0 F_{\mu\nu(0)} F^{\mu\nu}_{(0)} - \frac{1}{6\phi_0^2} \partial_\mu \partial^\mu \phi_0 \right), \tag{5.6}$$

where $F^{(0)}_{\mu\nu}$ is the field strength of the zero mode gauge field. Looking at the above action, we conclude that compactification of five dimensional gravity gives rise to electromagnetism and four dimensional gravity. This is a simple example of the idea of unification and represents the first successful step of unifying one of the SM forces (electromagnetism) with gravity. We have seen how one extra dimension can be successfully compactified to give a four dimensional theory. However, the presence of the massless scalar field (dilaton) poses a major problem in these constructions. This massless field predicts long range forces that may modify our laws of physics.

The situation is more complicated when trying to follow this approach to compactify the six extra dimensions corresponding to string theories (or seven extra dimensions in M-theory constructions). In such cases, compactification leads to a large number of massless scalars that are not observed in four dimensions. We will come back to the problem of massless scalar fields and ways of resolving it in later sections. The physics of the effective four dimensional theory that we obtain after compactifying the extra dimensions depends greatly on the internal manifold of the extra dimensions and its geometry. Since there are many ways of arranging these extra dimensions, we may obtain various four dimensional theories starting from the same high dimensional theory depending on the type of the internal manifold considered each time.

5.2.2 Internal manifolds

As we stated in the previous section, the idea of compactification can be applied to string theory, where the six extra dimensions span the geometry of the internal manifold that we denote by $\mathcal{M}_6$. We also refer to the resulting four dimensional manifold as $\mathcal{M}_4$. The manifold in ten dimensions can then be seen as a product of the four and six dimensional manifolds ($\mathcal{M} = \mathcal{M}_4 \times \mathcal{M}_6$). Similar to the case of Kaluza Klein reduction, the metric decomposes as,

$$ds = e^{2A(y)} g_{\mu\nu} dx^\mu dx^\mu + g_{mn} dy^m dy^n \tag{5.7}$$

where the indices μ, ν run in four dimensions $\{0, 1, 2, 3\}$ while the indices m, n run in six dimensions $\{1, ..., 6\}$, $g_{\mu\nu}$ is the four dimensional metric while g_{mn} is any six dimensional metric. The parameter $A(y)$ is a warp factor which is a function of the internal coordinates.

Compactifications of string or M-theory are required to preserve minimal Supersymmetry such that the four dimensional theory is supersymmetric at the compactification scale. Supersymmetry is then spontaneously broken by other mechanisms such as fluxes or non-perturbative effects. This condition upon the symmetry of the effective four dimensional theory restricts the choice of the internal geometry, which effectively means that only few internal manifolds can give rise to the required phenomenology at four dimensions.

Toroidal compactifications are not a very good choice for compactifying the extra dimensions, as they give rise to many Supersymmetries, more than it is required phenomenologically at low energy. In order to get an effective four dimensional theory with physics comparable to that of our observed universe, we need to find other types of internal manifolds. A more interesting and simple type of manifolds which is widely used in string and M-theory compactifications is known as Calabi-Yau manifold. Calabi-Yau manifolds (CY_n) are compact, Riemannian with $SU(n) \subset SO(2n)$ holonomy. The holonomy goup H is defined in simple terms as a set of matrices which are achieved when considering parallel transport along a closed curve on an n-dimensional manifold. In the case of heterotic and type I string theories, $d = 4, \mathcal{N} = 1$ is achieved by taking the six dimensional manifold to be a Calabi-Yau three-fold (CY_3) with $SU(3)$ holonomy. On the other hand, compactifications of type II theories, on the same type of manifold, give rise to $d = 4, \mathcal{N} = 2$ Supersymmetry starting from a 10-d theory with $\mathcal{N} = 2$ Supersymmetry.

Orientifold projections are a good mechanism for breaking Supersymmetry from $\mathcal{N} = 2$ down to $\mathcal{N} = 1$ Supersymmetry for type II theories. These are Z_2 projections with parity operation on the type II string world-sheet. The projection acts by transforming left-moving vibrations into right-moving ones. The other way around is also achieved, and the right-moving vibrations are transformed into left-moving ones. In general, the number of Supersymmetries is related to the number of massless gravitinos in the four dimensional theory. This means that breaking Supersymmetry from $\mathcal{N} = 2$ to $\mathcal{N} = 1$, in type II theories, corresponds to one of the gravitinos present becoming massive. The presence of intersecting D-branes in these theories preserves some of Supersymmetry ($\mathcal{N} = 1$) at low energy. One example of such constructions is type IIB orientifold compactifications on D_7 and D_3 branes. We note that breaking $\mathcal{N} = 1$ Supersymmetry also corresponds to the gravitino becoming massive. In this case, determining the right mass of the gravitino is very important in the study of phenomenologically viable models as we will see in the next chapter.

Similarly to the simple case of one extra dimension, Calabi Yau compactifications of ten dimensional string theories involve the decomposition of fields of the theory into four dimensional components. For instance, the 2-form field B_{MN} decomposes into $B_{\mu\nu}$ which gives only one zero mode. $B_{\mu n}$ and B_{mn}, on the other hand, give rise to a number of vector and scalar modes respectively. The metric g_{MN} also decomposes into 3 fields including $g_{\mu\nu}$, which gives rise to one zero mode, identified as the lower dimensional graviton. The field g_{mn} gives rise to a number of massless scalar modes at low dimensions. Some of these scalar fields are known as moduli fields. Calabi-Yau compactification is a vast subject on its own and involves many sub-fields such as differential geometry. We will not consider the technical details of such compactifications in this thesis; for a more thorough discussion, the reader is referred to the reviews [51, 56].

5.2.3 Moduli fields

Here and in the remainder of this thesis, we refer to the massless scalars, resulting from string compactifications to four dimensions, as ϕ_j. These scalars, which parameterise continuous families of four dimensional vacua and describe the geometry of the compact manifolds, are known as moduli fields.[1] Moduli are very important in identifying the configuration of internal manifolds in string theory compactifications. To understand the nature of the moduli space, let us consider the moduli space of Ricci flat metrics. This space characterises various choices of the Ricci metric g_{ij} that can be considered in order to achieve a valid string compactification. It is possible to vary this metric, locally, from one choice to another at any point in four dimensions. These variations must be described by fields. These variations between different metrics are, in fact, what gives rise to massless scalar fields which together form the moduli space. This is similar to the case of spontaneous symmetry breaking which leads to a massless field (Goldstone mode). The only diference is that moduli fields can exist without a symmetry.

In general, there are two types of scalar fields: neutral fields and charged matter fields. In this thesis, we only consider neutral scalars whose interactions are mainly gravitational. Geometrically, the moduli fields that result from Calabi-Yau compactifications parameterise the space of the associated internal manifolds. Their expectation values at the vacuum (Vevs) of the four dimensional effective theory represent the size and shape of the compact manifold. One type of these moduli

[1] Throughout this thesis, we will refer to scalar fields resulting from string compactifications as moduli even after a potential is generated for them.

is called Kähler moduli since they modify the structure of the Kähler manifold. There are also moduli that alter the complex structure and these are known as complex structure moduli. There are other types of moduli such as brane moduli, which represent positions of the branes involved in the compactification process. We note that this type of moduli will not be considered in this thesis.

The fact that these moduli fields are massless presents a serious problem for string phenomenology, as stated earlier. The existence of these massless fields means that they would couple to matter by mediating new long range forces. These extra forces are problematic, since they can modify the laws of physics of our four dimensional universe, that have already been confirmed by experiments. In other words, if these fields couple to varying types of matter, they would give rise to different forces since their coupling is not universal, which violates the equivalence theorem. In order to have a realistic theory and resolve this problem, we need to find a way of generating a potential through which they can be trapped.

Values of four dimensional quantities, such as coupling constants, depend on the values that the scalar fields take at the minimum of their potential. Since the values of these quantities can be measured by experiments, generating a potential for the moduli is crucial in order to have a viable model. Moduli fields are, usually, fixed at values where one of the minima of the potential lies (in cases where the potential exhibits such minima). This process of generating a potential and stabilising the scalar fields at phenomenologically viable minima is known as moduli stabilisation, which is one of the main themes of this thesis.

Generating a potential for the moduli fields is not only important in string phenomenology but also in inflation. The presence of this potential is important for realising inflationary scenarios in the framework of string theory since, without it, it would not be possible for the moduli fields to be trapped. However, even after generating a potential, the problem of flat directions can still arise. Uplifting these flat direction is also crucial since, otherwise, they would evolve forever and cause other more serious problems such as decompactification of internal dimensions. Our understanding of flux compactifications has led to important progress in this field in recent years. We will come back to this discussion in Chapter 7.

A typical Calabi-Yau compactification leads to hundreds of moduli fields, which makes it very difficult to study such models and their phenomenological implications. The existence of these moduli fields gives rise to many vacua in four dimensions, which means that we may find many possibilities of low dimensional physics depending on our choice of the internal manifold. These vacua may be

classified according to the value of the potential V_{min} as: Minkowski ($V_{min} = 0$), deSitter ($V_{min} > 0$) or Anti-deSitter ($V_{min} < 0$). We refer to all these types of vacua as the string landscape. Only vacua that fit closely with the requirements of particle physics and cosmology are considered as phenomenologically viable. These involve satisfying the condition $V_{min} = 0$ since we generally assume our local region of the universe to be modelled as Minkowski space-time[2]. deSitter vacua with small value of V may also be included. Even when considering Minkowski vacua only, we still find many choices of minima in parameter space and one may ask the question: how do we choose the vacuum that corresponds to our universe? We still do not know the answer to such a question since any minimum that is stable and satisfies the requirement of four dimensional physics can be considered as a viable one. We will not discuss the subject of string landscape in this thesis; there are, however, many related reviews that the reader may wish to consult such as [61].

5.3 Flux compactifications

Flux compactifications involve turning on the field strengths of the form fields present in the ten dimensional theory which are known as fluxes. These fluxes are related to form fields of dimension p (C_p) and can be written as $F_{p+1} = dC_p$. Introducing non-vanishing expectation values for these ten dimensional fluxes modifies the theory such that an effective potential is generated in four dimensions.

In general, fluxes exist in two different sectors of string theories. We have those which correspond to the NS-NS sector, where NS refers to Neveu Schwarz, and others arising from the Ramond-Ramond (R-R) sector. For string reductions, it is more useful (and sometimes necessary for purposes of moduli stabilisation) to consider both types of these fluxes together rather than only one. Fluxes, when introduced into string compactifications, have the characteristic of stabilising many moduli. In some cases, they may lead to the stabilisation of all relevant moduli, particularly when non-perturbative effects are added.

One of the simplest flux compactifications is the T^6/Z_2 orientifold of type II theories. In this construction, T^6 is a six dimensional torus with coordinates $x^i, i = 1, .., 6$. Compactifications where the compact dimensions are described by this torus give rise to $\mathcal{N} = 4$ Supersymmetry in four dimensions as stated in earlier

[2]In this thesis, we mainly consider vacua that satisfy Minkowski space-time.

sections. This Supersymmetry is then broken down to $\mathcal{N}=1$ by the parity function Z_2 which affects the coordinates along the compact dimensions ($x^i \to -x^i$). In other words, it swaps the left-and right-moving fields in the R-R or NS-NS sectors. This kind of compactifications lead to ten chiral multiplets at $D=4, \mathcal{N}=1$ which are namely: the dilaton S, three Kähler moduli and six complex structure moduli. There are many other compactifications where the fluxes play an important role in breaking Supersymmetry and stabilising the moduli fields. One of these compactifications is $T^6/Z_2 \times Z_2$ in the heterotic and type II theories which represent the basic constructions of the superpotentials discussed in Chapter 6. In the next section, we will briefly review the four dimensional structure of such compactifications.

5.4 Effective 4-D theories

Since our universe is four dimensional, we are interested in the description of compactifications in four dimensions so that we can relate their content to the SM. The ten dimensional description is not very attractive for phenomenology as it usually involves much more information than is needed. In addition to the matter content, a four dimensional effective $\mathcal{N}=1$ Supergravity, resulting from dimensional reductions of string or M-theory, is generally described by three functions: the superpotential $W(\phi_j)$, the Kähler potential $K(\phi_j, \overline{\phi}_{\bar{j}})$ and the gauge kinetic functions $f_j(\phi_j)$. These are described, respectively, as

- The superpotential $W(\phi_j)$ is a complex holomorphic function of the chiral superfields ϕ_j. This function may receive non-perturbative corrections as we will see in Chapter 6.
- The Kähler potential $K(\phi_j, \overline{\phi}_{\bar{j}})$ is a real non-holomorphic function of the chiral superfields ϕ_j. It may also receive non-perturbative corrections.
- The gauge kinetic functions $f_j(\phi_j)$ are complex holomorphic functions of the superfields ϕ_j.

One of the simplest examples of flux compactifications was discussed in the previous section. A similar compactification is $T^6/(Z_2 \times Z_2)$ orientifold which involves an additional Z_2 projection. We will briefly review the resulting four dimensional content of these compactifications on type IIA and heterotic theories [62, 63].

Heterotic theories compactified on $T^6/(Z_2 \times Z_2)$ lead to $\mathcal{N} = 1$ Supersymmetry in four dimensions. As stated earlier, the ten space-time dimensions are split into four dimensional space-time $\{1, 2, 3, 4\}$ and six space dimensions $\{5, .., 10\}$ respectively. One Z_2 projection is taken so that it acts on the coordinates $x^{5,6,7,8}$ while the other Z_2 acts on $x^{7,8,9,10}$. This type of compactifications defines three complex planes $(A_i,\ i = \{1, 2, 3\})$, which remain invariant by $Z_2 \times Z_2$, and correspond to the extra dimensions of the theory $(A_1 = 5, 6,\ A_2 = 7, 8$ and $A_3 = 9, 10)$.

For heterotic compactifications from ten to four dimensions, the fields decompose into different components. These include the dilaton ϕ, the two-form potential B_{ij} and the metric G_{ij}. The moduli fields can be defined in terms of the internal metric which is written as,

$$(G_{ij})_A = \frac{t_A}{u_A} \begin{pmatrix} u_A^2 + \nu_A^2 & \nu_A \\ \nu_A & 1 \end{pmatrix}. \tag{5.8}$$

where the indices i, j are the internal space dimensions $\{i, j = 5, ..10\}$ and the index A ranges over $\{1, 2, 3\}$. Seven moduli can then be identified as,

$$S = s + i\sigma, \quad T_A = t_A + i\tau_A, \quad U_A = u_A + i\nu_A. \tag{5.9}$$

The four dimensional superfields S, T_A and U_A are: the dilaton-axion, the volume moduli and the complex-structure moduli respectively. The real parts of these complex fields (s, t_A, u_A) [3] are known as geometrical moduli while the imaginary parts (σ, τ_A, ν_A) are called axions.

The Kähler potential is at the classical level and has the standard form in a general $\mathcal{N} = 1$ Supergravity theory derived from orbifold compactifications of string theory (matter fields are not considered in this thesis) [62, 64]:

$$K = -\ln(S + \overline{S}) - \sum_{A=1}^{3} \ln(T_A + \overline{T}_A) - \sum_{A=1}^{3} \ln(U_A + \overline{U}_A). \tag{5.10}$$

where $S, T_A, U_A, A \in \{1, 2, 3\}$ are the seven complex moduli fields resulting from the compactification scheme. The Kähler potential, given by Eq.(5.10), is obtained through the process of $\mathcal{N} = 4$ Supergravity gauging of heterotic and type IIA compactification with $z_2 \times z_2$ orbifold as discussed in [62, 63, 64]. The orbifold projection leads to an expression of the gravitino mass in $\mathcal{N} = 4$ Supergravity theory. Solving a set of constraint equations involving $\mathcal{N} = 4$ scalar fields, one can

[3] We are using geometric here to refer to the real parts of the moduli and not their connection to the geometry of the internal manifold.

rewrite the gravitino mass in terms of the $\mathcal{N}=1$ seven complex moduli S, U_A, T_A. Separating the holomorphic part in the gravitino mass term ($m_{3/2} = e^{K/2}W$), we obtain the above formula for the Kähler potential (Eq.(5.10)).

The scalar potential can be easily written for a particular model after identifying the Kähler potential and superpotential. We write the F-term of this potential, in $\mathcal{N}=1$ Supergravity, as,

$$V = e^K (K^{i\bar{j}} D_i W D_{\bar{j}} \bar{W} - 3W\overline{W}), \tag{5.11}$$

where $K^{i\bar{j}}$ is the inverse Kähler metric ($K_{i\bar{j}} = \partial^2 K/\partial\phi_i \partial\overline{\phi}_{\bar{j}}$) and $D_i W = \partial_i W + \partial_i K\, W$ is the Kähler covariant derivative acting on the superpotential. The indices i, j correspond to the relevant moduli S, T_A and U_A.

Similar chiral fields structure is also obtained when considering compactifications of type II theories. Branes are needed to preserve some Supersymmetry in these constructions. For instance, in the case of type IIA theories, $\mathcal{N}=1$ Supersymmetry is achieved with D_6 branes. The large number of fluxes present in type IIA ($F_0, F_2 ... F_6$) leads to a richer "zoo" of possibilities of superpotentials, compared to heterotic constructions, depending on the type and number of fluxes considered. For such theories at four dimensions, the complex fields T_a are found to be the same as the heterotic case. However, the real components of the fields S, U_A (s', u'_A) are found to be different from those presented in Eq.(5.9). These geometric moduli are given, in terms of those identified in the heterotic theory, as

$$s' = \sqrt{\frac{s}{u_1 u_2 u_3}}, \quad u'_1 = \sqrt{\frac{s u_2 u_3}{u_1}}, \quad u'_2 = \sqrt{\frac{s u_1 u_3}{u_2}}, \quad u'_3 = \sqrt{\frac{s u_1 u_2}{u_3}}. \tag{5.12}$$

Heterotic and type IIA constructions are not only different in terms of identification of geometric moduli. They also differ in the structure of the resulting superpotentials. This is mainly due to the fact that the allowed fluxes in heterotic theory cannot give rise to an explicit S dependence in the superpotentials as we will see in Chapter 6. Although the fluxes play an important role in generating a potential for the moduli fields and breaking Supersymmetry, a number of problems may still arise at low dimensions, such as flat directions and runaway solutions. These may be resolved by adding a non-perturbative superpotential term. We will come back to this in the next chapter.

In Chapter 6, we will study moduli stabilisation on a number of models resulting from heterotic and type IIA compactifications on the $T^6/(Z_2 \times Z_2)$ orientifold. We will discuss the stabilisation of all moduli analytically and numerically before we

move on to Chapter 7, where we discuss their dynamics and their contribution to the theory of modular inflation.

Chapter 6

Moduli Stabilisation

6.1 General structure of $\mathcal{N} = 1$ superpotentials

In this section, we discuss the role of gaugino condensation in modifying the structure of $\mathcal{N} = 1$ superpotentials resulting from compactifications of string theories as discussed in [64]. We also analyse the breaking of $\mathcal{N} = 1$ Supersymmetry in the presence of fluxes and the gaugino condensate superpotential.

6.1.1 Gaugino condensate and moduli fields

Compactifications of string theory give rise to many moduli at four dimensions with exact or spontaneously broken supersymmetries. The stabilisation of these moduli is very important, not only in particle physics, but also in cosmology since their dynamics play an important role in the theory of inflation as we shall see in Chapter 7. In order to have a realistic four dimensional theory, we need to explain the process of Supersymmetry breaking and its connection to moduli stabilisation. In some cases, introducing fluxes is not enough to break $\mathcal{N} = 1$ Supersymmetry; they also do not guarantee the stabilisation of all moduli which means that the effective potential may have flat or runaway directions. Non-perturbative effects are very important in breaking $\mathcal{N} = 1$ Supersymmetry. One of such effects is gaugino condensation which occurs in the infrared regime of strongly coupled gauge sectors. In general, a non-perturbative term can be written as,

$$W_{np} = \mu^3 e^{(-kZ)}, \tag{6.1}$$

where $k = \frac{24\pi^2}{b_0}$, b_0 is a one-loop beta-function coefficient, Z is a modulus and μ is the RG scale. After adding the non-perturbative term (W_{np}) to the flux superpotential (W_{flux}), one can write the effective superpotential as,

$$W_{eff} = W_{flux} + W_{np}. \tag{6.2}$$

To illustrate how the structure of both non-perturbative and flux terms in the superpotential affects the vacuum at four dimensions, we proceed by examining some examples discussed in [64].

First, we consider a superpotential where the flux term is given by a quantity a which is moduli dependent,

$$W = a + \omega(S), \tag{6.3}$$

where $\omega(S) = \mu^3 e^{-S}$. The modulus S is rescaled according to

$$\frac{24\pi^2 S}{b_0} \to S. \tag{6.4}$$

This rescaling leaves the corresponding kinetic terms unchanged and multiplies the scalar potential by a factor. For heterotic compactifications, the perturbative term a is only dependent on moduli U_A and T_A with $A = 1, 2, 3$, whereas for type II, the modulus S may feature in this term as we will see in later examples. The scale μ may depend on moduli U_A, T_A but we will assume that it is of $\mathcal{O}(1)$ for the models studied in this chapter.

As stated in earlier sections, the F-term scalar potential can be written in terms of the superpotential W as,

$$e^{-K}V = \sum_i |W - W_i(Z_i + \bar{Z}_i)|^2 - 3|W|^2. \tag{6.5}$$

If we consider a situation where the moduli T_A are not present in the superpotential, we can express the scalar potential as,

$$e^{-K}V = \sum_{T_A} |W - W_{T_A}(T_A + \bar{T_A})|^2 + \sum_{\{Z_i\}\equiv\{S,U_A\}} |W - W_i(Z_i + \bar{Z}_i)|^2 - 3|W|^2. \tag{6.6}$$

This means that the first term in Eq.(6.6) gives exactly $3|W|^2$ since, in this case, the first derivative of the superpotential with respect to T_A is zero ($W_{T_A} = 0$).

This term clearly cancels with the third term and gives a potential of the form,

$$e^{-K}V = \sum_{\{Z_i\}\equiv\{S,U_A\}} |W - W_i(Z_i + \bar{Z}_i)|^2. \tag{6.7}$$

We are led to a no-scale model [53], with a semi-positive-definite potential and flat directions along $\{T_A\}$. No-scale type usually refers to models where one term of the positive contribution to the scalar potential offsets the negative term $-3|W|^2$ and gives rise to a positive definite scalar potential. This situation is sometimes encountered in string models where the three geometrical moduli T_A represent flat directions.

Similar to the Kähler potential, the $\mathcal{N} = 1$ superpotentials, considered in this thesis, can be generated using the technique of $\mathcal{N} = 4$ Supergravity gauging. Performing this method for heterotic or type II compactications with $z_2 \times z_2$ orbifold generates expressions for the gravitino mass terms as a function of the $\mathcal{N} = 4$ scalar fields. The $z_2 \times z_2$ truncation, which is used to reduce Supersymmetry to $\mathcal{N} = 1$, leads to seven complex fields S, U_A, T_A in the moduli sector. Using a set constraint equations, the gravitino mass terms can be rewritten as a function of $\mathcal{N} = 1$ scalar fields. The $\mathcal{N} = 1$ superpotential can then be obtained, using the relation $m_{3/2} = e^{K/2}W$, as a polynomial in the moduli fields with maximum degree seven [62, 63, 64].

The identification of $\mathcal{N} = 1$ superpotentials also depends on the possible fluxes present in the theory. For example, in the case of type IIA theory compactified to four dimensions, we have R-R fluxes (F_0, F_2, F_4, F_6) as well as NS-NS and geometrical fluxes. After defining the moduli fields in terms of the internal metric, we can write the flux contributions to the $\mathcal{N} = 1$ superpotential. It is possible to switch on single fluxes such as the zero-form (F_0) which generates a superpotential dependent on the imaginary parts of the complex moduli fields T_A [63],

$$W = -iF_0T_1T_2T_3.$$

For type IIA orientifolds, we can also have examples with combined fluxes where most of the moduli fields are stabilised. For instance, switching a system of geometric, R-R and NS-NS fluxes ω_3, F_0, F_2, H_3, we get the following superpotential where four moduli fields are stabilised (for a specific choice of these fluxes)[63]:

$$W = a(ST_1 + ST_2 + ST_3) + a(T_1T_2 + T_2T_3 + T_3T_1) + 3ib(S + T_1T_2T_3).$$

More examples of $\mathcal{N} = 1$ superpotentials are listed in [63].

The presence of both perturbative and non-perturbative superpotentials plays an important role in modifying the structure of the vacuum in four dimensions [63]. In some cases, non-perturbative contributions to the superpotential not only break Supersymmetry, but they also have an important effect on the stabilisation of the relevant moduli and on the positivity of the scalar potential. In the next section, we will analyse the process of Supersymmetry breaking and its relation to the different moduli present in the theory. As stated in the previous chapter, we will mainly consider constructions of Minkowski vacua in four dimensions.

6.1.2 Supersymmetry breaking in Mikowski space

Supersymmetry breaking is very important for the realisation of four dimensional models comparable to the SM. In general, Supergravity theories provide an attractive framework for breaking Supersymmetry spontaneously. Such breaking is only achieved if the F_j auxiliary equations do not vanish along all moduli directions Z_j. These equations can be written as,

$$F_j \equiv W - (Z_j + \overline{Z_j})W_j = 0, \tag{6.8}$$

with the Kähler potetial given as outlined in the previous chapter,

$$K = -\sum_j \ln(Z_j + \overline{Z_j}). \tag{6.9}$$

Let us now look for ways of finding a stationary point of the corresponding scalar potential, where Supersymmetry breaks. Following [63], we demand that the conditions, given by Eq.(6.10), are satisfied in Minkowski space,

$$\langle V \rangle = 0\,, \qquad\qquad \langle W \rangle \neq 0\,. \tag{6.10}$$

We also solve the equations, $\partial_j V = 0$, for each scalar field Z_j. These can be written in terms of the Kähler potential, K, and the superpotential, W, as

$$\begin{aligned} 0 = \mathrm{e}^{-K} V K_j - \overline{W_j} F_j - 3 W_j \overline{W} + \\ \sum_{i \text{ with } i \neq j} \left[W_j - (Z_i + \overline{Z_i}) W_{ij} \right] \overline{F_i} - (Z_j + \overline{Z_j}) W_{jj} \overline{F_j}, \end{aligned} \tag{6.11}$$

where the scalar potential is given by,

$$V = e^K (K^{i\bar{j}} D_i W D_{\bar{j}} \bar{W} - 3W\overline{W}), \tag{6.12}$$

As an example, we consider a superpotential of the form,

$$W = (T_1 - T_2)(-U_1 + U_2 - T_3 + 2S) + (U_1 T_3 - L)w(S). \tag{6.13}$$

This superpotential is generated through the method of $\mathcal{N} = 4$ Supergravity gauging of $T^6/(z_2 \times z_2)$ orientifold compactifications of type IIA theory in the presence of geometric and F_2 fluxes [63, 64]. Using the above expression for W, we can see that the first term of Eq.(6.11) vanishes at a Minkowski point while the second derivative, W_{jj}, only appears for the case of moduli that are present in the gaugino condensate term (Modulus S for the superpotential given by Eq.(6.13)).

We consider the case where the scalar fields split in two categories. The first one controls the breaking of Supersymmetry where the conditions, $\langle W_j \rangle = 0$ and $\langle F_j \rangle = \langle W \rangle \neq 0$ are satisfied. The conditions $F_j = 0$ apply to the second category which preserves Supersymmetry. The number of scalar fields breaking Supersymmetry is exactly three as implied by the Minkowski condition $\langle V \rangle = 0$.

The stationary condition, given by Eq.(6.11), can then be written as

$$0 = \sum_{i \text{ with } i \neq j} \langle W_{ij} \operatorname{Re} Z_i \rangle, \tag{6.14}$$

with a summation restricted over moduli that break Supersymmetry. In the remainder of this chapter, we will look into examples where the structure of the superpotential gives indeed a partition between directions which break Supersymmetry and those which preserve it. The presence of the gaugino condensate term in the superpotential does not guarantee Supersymmetry breaking. To illustrate this, we analyse the following superpotential,

$$\begin{aligned} W = {} & A(U_1 - U_2)(T_1 - T_2) + B(U_1 + U_2 - 2U_3)(T_1 + T_2 - 2T_3) \\ & + (T_1 + T_2 - 2T_3)\omega(S). \end{aligned} \tag{6.15}$$

Let us start by writing the auxiliary equations $F_i \equiv W - W_i(Z_i + \bar{Z}_i)$ for all moduli. For instance those corresponding to the moduli U_1 and U_2 can be written

explicitly as follows,

$$\begin{aligned} F_{U_1} &\equiv A(-\overline{U}_1 - U_2)(T_1 - T_2) + B(-\overline{U}_1 + U_2 - 2U_3)(T_1 + T_2 - 2T_3) \\ &+ (T_1 + T_2 - 2T_3)\omega(S), \qquad (6.16) \\ F_{U_2} &\equiv A(U_1 + \overline{U}_2)(T_1 - T_2) + B(U_1 - \overline{U}_2 - 2U_3)(T_1 + T_2 - 2T_3) \\ &+ (T_1 + T_2 - 2T_3)\omega(S). \qquad (6.17) \end{aligned}$$

Cancellation of the auxiliary equations fixes the T_A moduli ($T_A = T$). We can clearly see that, for this choice of the T_A moduli, the auxiliary equations F_{U_1}, F_{U_2} vanish. However taking these moduli to be all equal at the vacuum gives $\langle W \rangle = 0$ which contradicts the conditions of Supersymmetry breaking presented in Eq.(6.10). Clearly Supersymmetry is not broken for this superpotential even though the condensate term $(T_1 + T_2 - 2T_3)\omega(S)$ is present.

In order to break Supersymmetry, we have to modify the above example by adding another term which we call the breaking term W_{break},

$$W_{break} = R(T_1 U_1 + T_2 U_2). \qquad (6.18)$$

The new superpotential is a combination of the breaking term and the one given by Eq.(6.1.2),

$$W' = W + W_{break}, \qquad (6.19)$$

For this superpotential, similarly to the previous superpotential W, cancellation of the F-auxilary equations along U_1, U_2 shows that the T_A moduli are all equal and real. Due to the presence of W_{break}, the condition $\langle W \rangle \neq 0$ is now satisfied and Supersymmetry is broken only if the condition $\langle V \rangle = 0$ is fulfilled as previously stated in Eq.(6.10). To satisfy this condition, we only require that the first derivative of superpotential is zero along the directions that break Supersymmetry. These directions are T_3, U_3 and S. The conditions $W'_{T_3} = W'_{U_3} = W'_S = 0$ read,

$$\begin{aligned} -2(B(U_1 + U_2 - 2U_3) + \omega(S)) &= 0, \qquad (6.20) \\ -2B(T_1 + T_2 - 2T_3) &= 0, \qquad (6.21) \\ -(T_1 + T_2 - 2T_3)\omega(S) &= 0. \qquad (6.22) \end{aligned}$$

Since the moduli T_A are all equal and real, Eqs.(6.21, 6.22) are satisfied exactly. The remaining directions, T_1, T_2, U_1 and U_2, preserve Supersymmetry and, therefore, their F-auxilary equations are zero. The auxilary equations along T_1 and T_2

can be written as follows,

$$\begin{aligned} F_{T_1} &\equiv A(U_1-U_2)(-\overline{T}_1-T_2)+B(U_1+U_2-2U_3)(-\overline{T}_1+T_2-2T_3) \\ &+ (-\overline{T}_1+T_2-2T_3)\omega(S)+R(-\overline{T}_1U_1+T_2U_2)=0, \qquad (6.23) \\ F_{T_2} &\equiv A(U_1-U_2)(T_1+\overline{T}_2)+B(U_1+U_2-2U_3)(T_1-\overline{T}_2-2T_3) \\ &+ (T_1-\overline{T}_2-2T_3)\omega(S)+R(T_1U_1-\overline{T}_2U_2)=0. \qquad (6.24) \end{aligned}$$

Taking U_A to be real and $U_1 = U_2 = U$, Eqs.(6.23, 6.24) can be simplified as,

$$-2TB(2U-2U_3)-2T\omega(S)=0. \qquad (6.25)$$

This equation, which fixes the field U_3 at $\omega(S)/2B+U$ at the minimum, is equivalent to Eq.(6.20). The stationary point condition given by Eq.(6.14) can be written for this model as,

$$\mathrm{Re}\, S = -2B(U+T)-\omega(S). \qquad (6.26)$$

The model studied above has a minimum, with broken Supersymmetry, at real T_A and U_A with the moduli $T_A = T$ and $U_1 = U_2$. The modulus U_3 is fixed at the minimum by Eq.(6.20) while $\mathrm{Re}\, S$ is fixed by Eq.(6.26). Although the condensate term is present in this model, it does not contribute to the breaking of Supersymmetry which is only broken when the term W_{break} is added explicitly to the superpotential. We will not comment on this model any further. Instead, we will look at another class of models where the presence of the gaugino condensate term is crucial for breaking Supersymmetry. These models are presented in the next section with numerical solutions.

6.2 Analysis of DKP models

We have presented examples of models where the presence of the gaugino condensate was not responsible for breaking Supersymmetry in Section 6.1. In this section, we analyse models discussed by Derendinger et al. [64] (from now on, we refer to these models as DKP models). We will also comment on a model discussed by Löwen et al. [65], which has similar features to one of the DKP models (we refer to it as LNZ model). In these models, the presence of the gaugino condensate is crucial for the breaking of Supersymmetry.

6.2.1 Model I

We look at an example of type IIA, where the condensate term breaks Supersymmetry and, therefore, fully contributes to the structure of the effective theory in the vacuum. We consider the following superpotential, as given in Eq.(6.13),

$$W = (T_1 - T_2)(-U_1 + U_2 - T_3 + 2S) + (U_1 T_3 - L)\omega(S), \tag{6.27}$$

where L is a flux parameter and $\omega(S)$ is the condensate term given in terms of the dilaton field as,

$$\omega(S) = \mu^3 e^{-S}. \tag{6.28}$$

As discussed in Section.6.1, this model has particular directions which break Supersymmetry; these are T_1, T_2 and the flat direction U_3. The directions which preserve Supersymmetry are: T_3, U_1, U_2 and S. From now on, we will refer to this as model I.

To ensure that $\langle V \rangle = 0$, we only require that $\langle W_{T_1} \rangle = \langle W_{T_2} \rangle = 0$. Only two conditions should be fulfilled for the Supersymmetry breaking directions, since the superpotential is independent of U_3. The resulting Supersymmetry-breaking condition reads

$$-U_1 + U_2 - T_3 + 2S = 0. \tag{6.29}$$

The vanishing of the F-auxiliary fields ($F_j \equiv W - (Z_j + \overline{Z_j})W_j = 0$) along the directions T_3, U_1, U_2 and S leads to the following equations,

$$\begin{aligned}
\xi\left(\overline{U_1} + U_2 - T_3 + 2S\right) - \left(\overline{U_1}T_3 + L\right) w(S) &= 0, && (6.30)\\
\xi\left(-U_1 - \overline{U_2} - T_3 + 2S\right) + \left(U_1 T_3 - L\right) w(S) &= 0, && (6.31)\\
\xi\left(-U_1 + U_2 + \overline{T_3} + 2S\right) - \left(U_1\overline{T_3} + L\right) w(S) &= 0, && (6.32)\\
\xi\left(-U_1 + U_2 - T_3 - 2\overline{S}\right) + \left(U_1 T_3 - L\right)\left(1 + S + \overline{S}\right) w(S) &= 0, && (6.33)
\end{aligned}$$

where, following [64], we have introduced,

$$\xi \equiv T_1 - T_2. \tag{6.34}$$

The stationary point condition, $\partial_j V = 0$, given by Eq.(6.14) reads,

$$\mathrm{Re}\,\xi = 0. \tag{6.35}$$

Combining Eq.(6.30) and Eq.(6.32), we get

$$\xi(\overline{U}_1 + U_1 - T_3 - \overline{T}_3) + (U_1\overline{T}_3 - \overline{U}_1 T_3)\omega(S) = 0. \tag{6.36}$$

This equation clearly shows that the moduli T_3 and U_1 are equal ($T_3 = U_1$). A similar combination of Eq.(6.30) and Eq.(6.31) gives,

$$\xi(\overline{U}_1 + U_1 + U_2 + \overline{U}_2) - (\overline{U}_1 U_1 + U_1^2)\omega(S) = 0. \tag{6.37}$$

For Eq.(6.37) to be consistent, the modulus U_1 must be real, which also means that T_3 is real ($T_3 = U_1 = t$). We can rearrange Eq.(6.30) for ξ, taking U_1, T_3 to be equal and real, and the result is,

$$\xi = \frac{(t^2 + L)\omega(S)}{U_2 + 2S}. \tag{6.38}$$

To ensure that the stationary point condition is fulfilled ($\mathrm{Re}\,\xi = 0$), we adjust the imaginary part of the modulus S ($S = s - i\frac{\pi}{2}$). This also implies, through Eq.(6.29), that $U_2 = u + i\pi$.

So far, we have looked at possible combinations of the F-auxiliary fields, which gave us certain requirements on the real and imaginary parts of the moduli. Now, we can easily express the extremisation equations for the fields t, u and s. These equations are given as Eq.(6.29), a combination of Eq.(6.30) and Eq.(6.31), as well as a combination of Eq.(6.29), Eq.(6.30) and Eq.(6.33), and read:

$$\begin{aligned} u + 2(s - t) &= 0, & (6.39)\\ t\left(t^2 - L\right) - u\left(t^2 + L\right) &= 0, & (6.40)\\ t^5 + 2Lt^3 - 4Lt^2 - 3L^2 t - 4L^2 &= 0. & (6.41) \end{aligned}$$

An expression of $\xi = T_1 - T_2$ can also be derived using any of the Eqs.(6.30-6.30), once all the other moduli are fixed. Eq.(6.30), for instance, can be rearranged to give an expression for ξ as shown in Eq.(6.38); this latter can be simplified further to

$$\xi = \frac{t^2 + L}{u + 2s}\omega(S). \tag{6.42}$$

The gravitino mass can also be expressed in terms of t, L and $\omega(S)$,

$$\mathrm{e}^{-K/2}\, m_{3/2} = \langle W \rangle = \left(t^2 - L\right)\omega(S). \tag{6.43}$$

Using Eq.(6.41) and assuming $L > 0$, we obtain

$$L = t^2 \frac{t - 2 + 2\sqrt{t^2 + 1}}{3t + 4}, \tag{6.44}$$

where the choice for the sign of the square root is the only one compatible with the positivity of all moduli.

As stated earlier, in this model the gaugino condensate is entirely responsible for the breaking of Supersymmetry. In order to see whether the solutions, given in Eqs.(6.44-6.34), derived for this model represent viable minima, we need to look at numerical examples and study the structure of the scalar potential (5.11) along different moduli directions. One choice of these solutions is presented in Table 6.1, where the parameter μ is fixed at $\mu = 2$. The scalar potential exhibits a global minimum at these values, as shown in Figs.(6.1, 6.2). These two figures illustrate the scalar potential displayed in the complex planes S and U_2 respectively.

Since this is a model of seven complex fields, it is hard to see, graphically, whether the above numerical example is a viable minimum in all directions. Therefore, calculating the Hessian matrix is crucial in order to identify the viability of this minimum. This matrix was evaluated and found to be positive definite which confirms that the above numerical example is indeed a global minimum of the scalar potential along all the relevant moduli. For details of the calculation of this matrix, we refer the reader to Appendix C.

Parameter/ Moduli	L	t	u	s	$\mathrm{Im}\,\xi$
Values	1.788	2	0.763	1.618	2.295

TABLE 6.1: One particular choice of numerical solutions to model I.

As shown in Eq.(6.43), the gravitino mass is dependent on the values of $\mathrm{Re}\,S$ and the parameter μ. In order to achieve a phenomenologically viable gravitino mass (about $10^{-14} M_p$)[1], with $\mathrm{Re}\,S$ as well as the other fields fixed at their minimum values presented in Table 6.1, the value of μ must be very small of order $\mu = 10^{-4}$. If, however, we keep the value of μ fixed at $\mu = 2$, which is the value used so far in the model, larger values of $\mathrm{Re}\,S$ (from 15 up to 30) must be considered in order to achieve a lighter gravitino mass. Numerical results of the gravitino mass are presented in Table 6.2, where we also show the corresponding values of μ and

[1]We denote the Planck mass as $M_p \sim 10^{19} GeV$. In most of this thesis, we will assume Planck units and take $M_p = 1$.

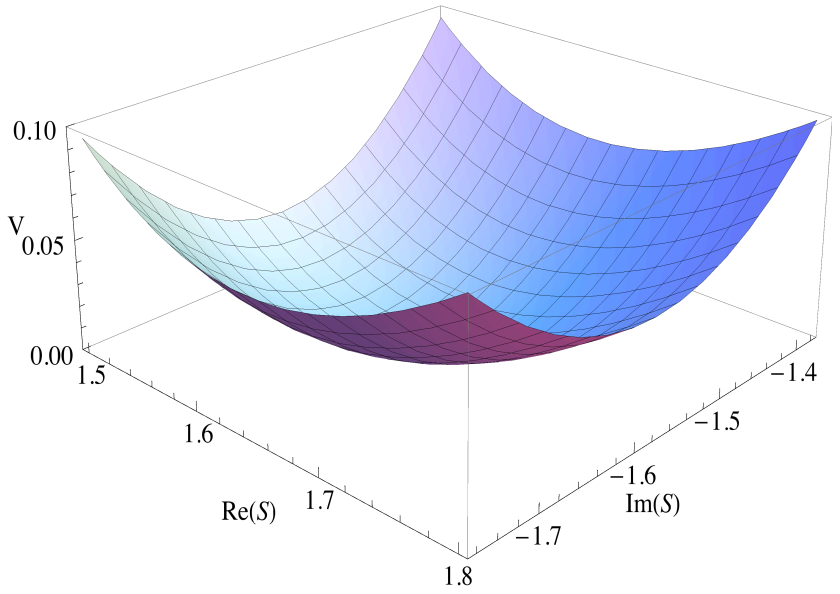

FIGURE 6.1: Stabilising potential for $\mathrm{Re}\, S$, $\mathrm{Im}\, S$. All other moduli have been fixed at their minimum values.

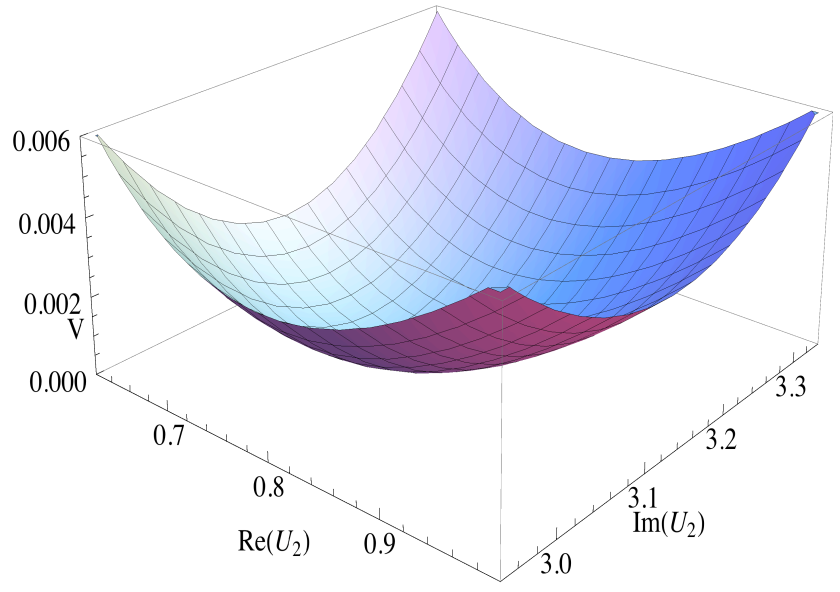

FIGURE 6.2: Stabilising potential for $\mathrm{Re}\, U_2$, $\mathrm{Im}\, U_2$. The remaining moduli are fixed at their minimum values.

$\mathrm{Re}\, S$. Taking the value of μ to be $\mu = 10^{-4}$ does not affect the values of the moduli fields at the minimum except the value of $\mathrm{Im}\, \xi = \mathrm{Im}\, T_1 - \mathrm{Im}\, T_2$ which becomes $\xi \approx 2.29 \times 10^{-13}$. Changing the value of $\mathrm{Re}\, S$, on the other hand, affects the minimum values of the other fields and, therefore, in this case we need to look for another numerical example that is different from the one presented in Table 6.1.

μ	2	2	2	10^{-3}	10^{-4}
$\mathrm{Re}\, S$	16	20	25	1.618	1.618
$m_{3/2}(M_p)$	5.2×10^{-8}	8.7×10^{-10}	5.4×10^{-12}	2.4×10^{-11}	2.4×10^{-14}

TABLE 6.2: The dependence of the gravitino mass (in Planck units) on the parameter μ and modulus S for model I.

We showed how some of the moduli present in this model are successfully stabilised with numerical examples. However, there are two flat directions. One of them is along U_3, which is not present in the superpotential given by Eq.(6.13). The other one is along the $T_1 + T_2$ direction. Before studying the dynamics of the moduli presented in this section, we need to find a way to lift the flat directions. One way to proceed is the application of the local no-scale idea [66, 67].

6.2.2 Lifting the flat directions

The DKP model presented in the previous section (model I) has one problem, which is the appearance of unfixed U_3 moduli in addition to the $T_1 + T_2$ direction. These flat directions can be uplifted by applying the local no-scale idea, where corrections to the Kähler potential are added to fix the moduli while the flatness condition ($V \equiv 0$) applies only locally [65, 66, 67].

For the flatness condition to be around point z_0 in $\mathcal{D}$, one demands:

$$\partial_z \partial_{\overline{z}} e^{-G/3} = \phi_{z\overline{z}}(z, \overline{z}), \tag{6.45}$$

where $\mathcal{D}$ is the positive kinetic energy domain (defined by $G_{z\overline{z}} > 0$) and G is the Kähler function, which is related to the Kähler potential K and the superpotential W by,

$$G = K + \ln |W|^2. \tag{6.46}$$

The function $\phi(z, \overline{z})$ satisfies the conditions:

$$\phi_{z\overline{z}} \geq 0, \forall z \in \mathcal{D}, \tag{6.47}$$

and

$$\phi_{z\overline{z}}(z_0, \overline{z}_0) = 0. \tag{6.48}$$

The solution for Eq.(6.45) is given by:

$$G = -\frac{3}{2}\log(f + \overline{f} + \phi)^2. \tag{6.49}$$

We can express the condition for the positive kinetic energy domain in terms of the functions ϕ, f and their derivatives,

$$G_{z\overline{z}} = 3\frac{|f_z + \phi_z|^2 - \phi_{z\overline{z}}(f + \overline{f} + \phi)}{(f + \overline{f} + \phi)^2} > 0. \tag{6.50}$$

In a general $\mathcal{N} = 1$ Supergravity theory, the scalar potential V can be expressed in terms of the function G as,

$$V = e^G(G^{z\overline{z}}G_z G_{\overline{z}} - 3). \tag{6.51}$$

For G given by Eq.(6.49), we can write the scalar potential,

$$V = 3\frac{\phi_{z\overline{z}}(f + \overline{f} + \phi)}{|f + \overline{f} + \phi|^3\left(|f_z + \phi_z|^2 - \phi_{z\overline{z}}(f + \overline{f} + \phi)\right)}. \tag{6.52}$$

From the above equation, we can see that the potential is positive definite in $\mathcal{D}$ only if the conditions $\phi_{z\overline{z}} \geq 0$ and $f + \overline{f} + \phi > 0$ are satisfied exactly.

Let us consider a correction to the Kähler potential ϕ, given by,

$$\phi = \frac{(z - z_0)^2(\overline{z} - \overline{z}_0)^2}{4}. \tag{6.53}$$

This correction affects the shape of the scalar potential only outside the minimum value z_0. If we fix the value of the field at z_0, the function, ϕ, vanishes and the structure of the potential, without its presence, can be restored. To see how the correction, ϕ, modifies the scalar potential along the flat directions in model I, let us apply this procedure to uplift the flat direction along the complex modulus, $U_3 = \mathrm{Re}\, U_3 + i\,\mathrm{Im}\, U_3$, for example. This function can then be written, in terms of

$\mathrm{Re}\, U_3$ and $\mathrm{Im}\, U_3$, as

$$\begin{aligned}\phi(U_3) &= \frac{(U_3-(U_3)_0)^2(\overline{U}_3-(\overline{U}_3)_0)^2}{4},\\ &= \frac{((\mathrm{Re}\, U_3-(\mathrm{Re}\, U_3)_0)^2+(\mathrm{Im}\, U_3-(\mathrm{Im}\, U_3)_0)^2)^2}{4},\end{aligned} \tag{6.54}$$

where $(U_3)_0$ is the minimum value along U_3. The conditions for the positivity of the scalar potential are both satisfied. To see this, we write $\phi_{U_3\overline{U}_3}$ and $U_3+\overline{U}_3+\phi$, as a function of the real and imaginary parts of U_3, as follows,[2]

$$\phi_{U_3\overline{U_3}} = ((\mathrm{Re}\, U_3-(\mathrm{Re}\, U_3)_0)^2+(\mathrm{Im}\, U_3-(\mathrm{Im}\, U_3)_0)^2, \tag{6.55}$$

$$\begin{aligned}U_3+\bar{U}_3+\phi &= 2\,\mathrm{Re}\, U_3\\ &+ \frac{((\mathrm{Re}\, U_3-(\mathrm{Re}\, U_3)_0)^2+(\mathrm{Im}\, U_3-(\mathrm{Im}\, U_3)_0)^2)^2}{4}.\end{aligned} \tag{6.56}$$

The above equations show that the positivity condition, given by Eq.(6.50), is satisfied. Now, we can study the structure of the scalar potential in this direction. Fig.(6.4) presents the stabilising potential for the U_3 direction, where the minimum value is taken to be purely real ($\mathrm{Im}\, U_3 = 0$) with the value $(U_3)_0 = 0.5$. A similar procedure can be followed in order to uplift the T_1+T_2 direction locally. Fig.(6.3) shows the scalar potential as a function of the complex modulus T_1, where the minimum value, along this direction, is given by $(T_1)_0 = 1+i(\xi_0+1)$ with $\xi_0 = \mathrm{Im}\,\xi = 2.295$, as presented in Table 6.1. The minimum value for T_2 is taken to be $(T_2)_0 = 1+i$, such that $\mathrm{Im}\,(T_1-T_2) = \xi_0$ and $\mathrm{Re}\,(T_1-T_2) = 0$, as required by the stationary point condition in Eq.(6.35).

[2]Here, we are taking the function f to be equal to U_3.

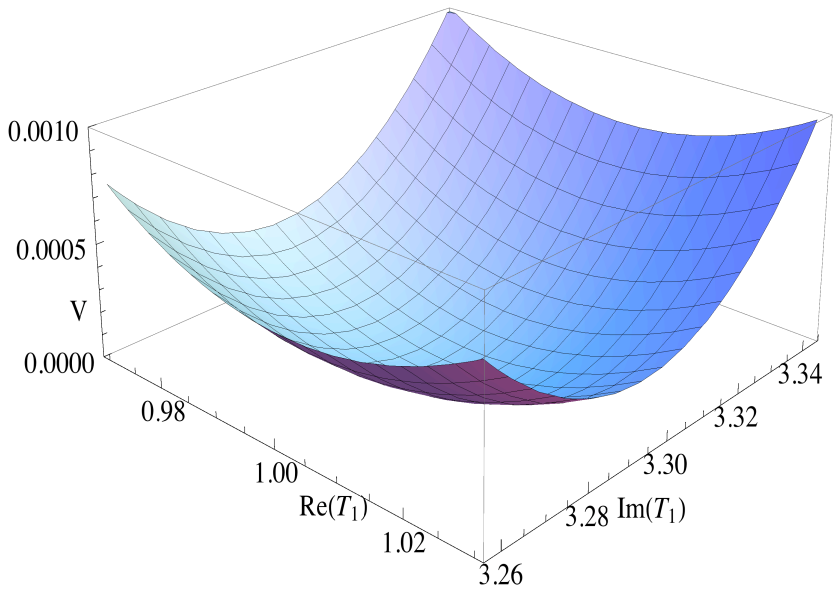

FIGURE 6.3: Scalar potential as a function of the complex modulus T_1. The remaining moduli are all fixed at their Vevs.

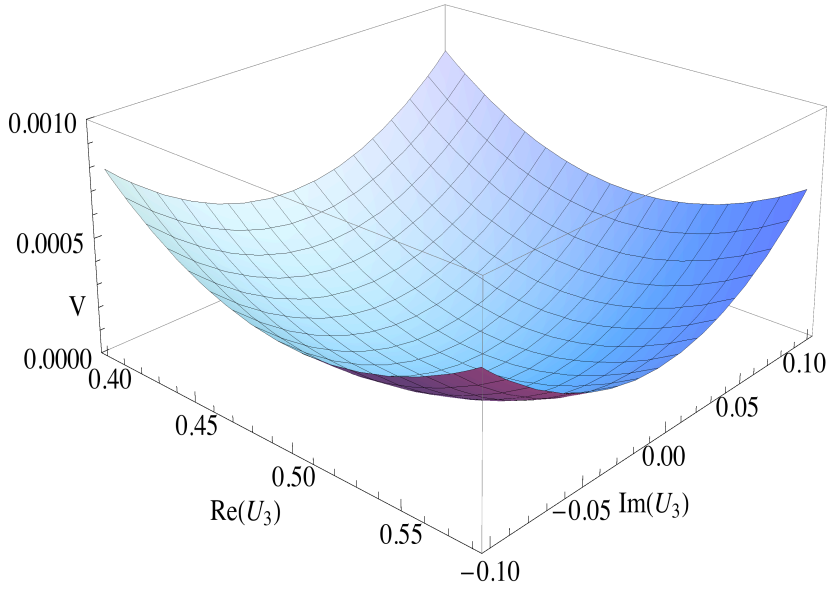

FIGURE 6.4: Scalar potential as a function of the complex modulus U_3. The remaining moduli are all fixed at their minimum values.

6.3 Model II

We now consider another DKP model originating from heterotic compactifications, which we refer to as model II from now on. Although heterotic compactifications are similar to type II when Supersymmetry breaking is mostly due to fluxes, they turn out to be very different in cases where Supersymmetry breaking is induced by a gaugino condensate[3]. The main reason is the absence of S contributions to the superpotential directly originating from fluxes. Let us consider a superpotential with the following form [64],

$$W = \hat{A}U_1 + \hat{B}U_2 + \hat{C}U_3 + \hat{D}U_1U_2U_3. \tag{6.57}$$

This superpotential is odd in the fields U_i and captures most of the features of the heterotic compactifications, with a gaugino condensate. The following functions of T_1, T_2 and S have been introduced,

$$\hat{A} = (\alpha + \alpha'\omega(S))\,\xi + A\omega(S), \tag{6.58}$$

$$\hat{B} = (\beta + \beta'\omega(S))\,\xi + B\omega(S), \tag{6.59}$$

$$\hat{C} = (\gamma + \gamma'\omega(S))\,\xi + C\omega(S), \tag{6.60}$$

$$\hat{D} = (\delta + \delta'\omega(S))\,\xi + D\omega(S), \tag{6.61}$$

where the parameters ξ and $w(S)$ are given as follows,

$$\xi = T_1 - T_2 \ , \ \omega(S) = \mu^3 e^{-S}.$$

In the remainder of this section, we will present the DKP solutions for model II, following [64] closely. We will then discuss the problematic aspects of their solution and propose an alternative one with a numerical example.

6.3.1 The DKP solutions

We start by deriving the stationary point condition given by Eq.(6.14). The moduli directions that break Supersymmetry, in this model, are T_1, T_2 and the flat direction T_3. On the other hand, Supersymmetry is preserved by the remaining

[3]The difference between models originating from heterotic and type II compactifications will become more apparent in the next chapter, when we look at inflation.

directions along U_i and S. This means that we can express the stationary point condition as,

$$(\alpha+\alpha'\omega+(\delta+\delta')U_2U_3)\,\mathrm{Re}\,(T_1-T_2)+(\beta+\beta'\omega+(\delta+\delta')U_1U_3)\,\mathrm{Re}\,(T_1-T_2)+ (\gamma+\gamma'\omega+(\delta+\delta')U_1U_2)\,\mathrm{Re}\,(T_1-T_2)=0, \tag{6.62}$$

which clearly leads to the vanishing of ξ at the minimum ($\mathrm{Re}\,\xi=0$). We choose the modulus S to have an imaginary part with the value $-\pi/2$ ($S=s-i\pi/2$) and the fields U_i to be all real and equal ($U_i=u_i$). This choice makes everything consistent provided that the flux parameters α, β, γ, δ and A, B, C, D are all real while α', β', γ', δ' are imaginary.

The vanishing first derivatives of the superpotential in terms of T_1 and T_2 ($\langle W_{T_1}\rangle = \langle W_{T_2}\rangle = 0$) means that the no-scale requirement $\langle V\rangle = 0$ is fulfilled. The corresponding condition reads,

$$(\alpha+\alpha'\omega)u_1+(\beta+\beta'\omega)u_2+(\gamma+\gamma'\omega)u_3+(\delta+\delta'\omega)u_1u_2u_3=0. \tag{6.63}$$

The vanishing of the U_A-auxiliary and S-auxiliary fields, $F_S = F_{U_A} = 0$, read,

$$-\hat{A}u_1+\hat{B}u_2+\hat{C}u_3-\hat{D}u_1u_2u_3=0, \tag{6.64}$$

$$\hat{A}u_1-\hat{B}u_2+\hat{C}u_3-\hat{D}u_1u_2u_3=0, \tag{6.65}$$

$$\hat{A}u_1+\hat{B}u_2-\hat{C}u_3-\hat{D}u_1u_2u_3=0. \tag{6.66}$$

The above equations imply that,

$$\hat{A}u_1=\hat{B}u_2=\hat{C}u_3=\hat{D}u_1u_2u_3. \tag{6.67}$$

Following [64], Eq.(6.67) allows us to express u_1, u_2 and u_3, in terms of ξ and s, as

$$u_1=\sqrt{\frac{\hat{B}\hat{C}}{\hat{A}\hat{D}}},\;\; u_2=\sqrt{\frac{\hat{A}\hat{C}}{\hat{B}\hat{D}}},\;\; u_3=\sqrt{\frac{\hat{A}\hat{B}}{\hat{C}\hat{D}}}. \tag{6.68}$$

The equation for the $S-$auxiliary field gives:

$$\frac{2}{s}=-4-\left(\frac{\alpha'}{\hat{A}}+\frac{\beta'}{\hat{B}}+\frac{\gamma'}{\hat{C}}+\frac{\delta'}{\hat{D}}\right)\xi\omega. \tag{6.69}$$

In order to solve for s and ξ, the authors of [64] introduced a set of intermediate imaginary quantities λ_i, defined by:

$$\hat{A} = \lambda_1 \xi\omega, \;\; \hat{B} = \lambda_2 \xi\omega, \;\; \hat{C} = \lambda_3 \xi\omega, \;\; \hat{D} = \lambda_4 \xi\omega. \tag{6.70}$$

The authors also claim that solutions with large and positive s, together with exponentially small ξ do exist under minor and natural assumptions on the fluxes (coefficients $\alpha, \beta, \gamma, \delta, \alpha', \beta', \gamma', \delta'$ and A, B, C, D). For simplicity, they consider the plane-symmetric situation, where

$$\alpha = \beta = \gamma, \;\; \alpha' = \beta' = \gamma', \;\; A = B = C. \tag{6.71}$$

The above conditions imply,

$$\lambda_1 = \lambda_2 = \lambda_3 \equiv \lambda, \;\; u_1 = u_2 = u_3 \equiv u, \tag{6.72}$$

and the resulting equation for u can be written as

$$u = \sqrt{\frac{\lambda}{\lambda_4}}. \tag{6.73}$$

The parameters λ and λ_4 are given, in terms of the flux coefficients, by

$$\frac{1}{\lambda} = \frac{\omega}{3(\alpha + \alpha'\omega)} \frac{3D\alpha + A\delta + (3\alpha' D + A\delta')\omega}{D\alpha - A\delta + (D\alpha' - A\delta')\omega}, \tag{6.74}$$

$$\frac{1}{\lambda_4} = -\frac{\omega}{(\delta + \delta'\omega)} \frac{3D\alpha + A\delta + (3\alpha' D + A\delta')\omega}{D\alpha - A\delta + (D\alpha' - A\delta')\omega}. \tag{6.75}$$

Equations for ξ and s can be summarised as follows,

$$\xi = -\frac{1}{4} \frac{3D\alpha + A\delta + (3\alpha' D + A\delta')\omega}{(\alpha + \alpha'\omega)(\delta + \delta'\omega)} \omega, \tag{6.76}$$

$$\frac{2}{s} = -4 - \frac{(\alpha'\delta - \delta'\alpha)\omega}{(\alpha + \alpha'\omega)(\delta + \delta'\omega)} \frac{3D\alpha + A\delta + (3\alpha' D + A\delta')\omega}{D\alpha - A\delta + (D\alpha' - A\delta')\omega}. \tag{6.77}$$

Provided that the flux coefficients $\alpha, \delta, \alpha', \delta', A, D$ are large while their ratios are of order unity, Eq.(6.77) admits acceptable solutions for s. If this requirement is fulfilled, a variable ρ (which is a real function of s) can be defined as

$$\rho = i \frac{D\alpha - A\delta}{D\alpha\omega}. \tag{6.78}$$

This variable can be taken to be of $\mathcal{O}(1)$ since ω is small and the ratio of the coefficients is also of $\mathcal{O}(1)$.

Under these assumptions, an expansion in powers of ω can be performed for all quantities. This simplifies the expressions of s and ξ as,

$$\xi \approx -\frac{D}{\delta}\omega, \tag{6.79}$$

$$\frac{1}{2s} \approx -1 - \frac{D}{\delta}\frac{\alpha'\delta - \delta'\alpha}{D\alpha' - A\delta' - iD\alpha\rho}. \tag{6.80}$$

The gravitino mass can also be expressed in terms of the flux parameters and ω as,

$$e^{-K/2}m_{3/2} = \frac{A\delta' - D\alpha' + \frac{A\delta - D\alpha}{\omega}}{\alpha + \alpha'\omega}\left(-3\frac{\alpha + \alpha'\omega}{\delta + \delta'\omega}\right)^{3/2}\omega^2. \tag{6.81}$$

In the special case where $\alpha' = i\alpha, \quad \delta' = -i\delta$, Eq.(6.81) simplifies further to:

$$\begin{aligned} e^{-K/2}m_{3/2} &\approx i\left(2De^{-2s} + \frac{A\delta - D\alpha}{\alpha}e^{-s}\right) \\ &\approx i4D\left(-\frac{3\alpha}{\delta}\right)^{3/2}\frac{s}{2s+1}\omega^2. \end{aligned} \tag{6.82}$$

The above equation shows that the gravitino mass scales as ω^2. The dependence of the gravitino mass on ω^2 does not guarantee it to have a phenomenologically viable value. We think that the double suppression appears mainly due to the arrangement of parameters in the gravitino mass formula in Eq.(6.82). This means that choosing a small value for $\mathrm{Re}\, S$, for example $\mathrm{Re}\, S = 1$, will not always give rise to a phenomenologically viable value of the gravitino mass even with the presence of ω^2 in the formula. A similar discussion was presented in the previous section, where we have looked at some numerical examples as shown in Table 6.2.

So far, we have outlined the DKP solutions to model II as presented in [64]. We will proceed, in the next section, by analysing these solutions and presenting their problematic aspects. We will also propose alternative ones and study them numerically.

6.3.2 Alternative solutions to model II

This DKP model, similarly to Model I, has the problem of flat directions along the U_3 and $T_1 + T_2$ directions. We will not comment on this problem further as we have discussed it in detail for model I and presented a way of fixing the flat directions. Another, more important, problem is the inconsistency in the solutions presented in Eqs.(6.73-6.82). When trying to find numerically viable minima to the corresponding scalar potential, it was not possible to find a set of coefficients α, β, A and D that satisfied all the solutions and gave rise to a Minkowski vacuum along those directions. We now discuss in detail alternative solutions that result in phenomenologically viable minima.

Starting from Eqs.(6.64, 6.65, 6.66), we can see that, by taking the fields u_i all to be equal and real, the condition, given by Eq.(6.83), must be fulfilled,

$$\hat{A} = \hat{B} = \hat{C}, \tag{6.83}$$

which gives rise to the following equation for u

$$u^2 = \frac{\hat{A}}{\hat{D}}. \tag{6.84}$$

Expressions for ξ can be derived using the condition presented in Eq.6.83. For instance, setting the expressions of $\hat{A}$ and $\hat{B}$ to be equal and rearranging for ξ, we get

$$(\alpha - \beta + (\alpha' - \beta')\omega)\xi = (B - A)\omega. \tag{6.85}$$

Similar arrangements can be made for the conditions $\hat{A} = \hat{C}$ and $\hat{B} = \hat{C}$. This leads to three expressions for ξ, in terms of the flux coefficients and ω, given as,

$$\xi = \frac{(B-A)\omega}{\alpha - \beta + (\alpha' - \beta')\omega} = \frac{(C-A)\omega}{\alpha - \gamma + (\alpha' - \gamma')\omega} = \frac{(C-B)\omega}{\beta - \gamma + (\beta' - \gamma')\omega}. \tag{6.86}$$

Rearranging the parameters in the expressions of ξ, presented in Eq.(6.86), also leads to three different expressions for the term ω. To see this, let us start by setting the first two expressions in Eq.(6.86) to be equal. This gives,

$$(C-A)(\alpha-\beta) + (C-A)(\alpha'-\beta')\omega = (B-A)(\alpha-\gamma) + (B-A)(\alpha'-\gamma')\omega, \tag{6.87}$$

which leads to the following expression for ω

$$\omega = \frac{(B-A)(\alpha-\gamma)-(C-A)(\alpha-\beta)}{(C-A)(\alpha'-\beta')-(B-A)(\alpha'-\gamma')}. \tag{6.88}$$

Using the other expressions of ξ, we obtain two more equations which can be written as,

$$\omega = \frac{(B-A)(\beta-\gamma)-(C-B)(\alpha-\beta)}{(C-B)(\alpha'-\beta')-(B-A)(\beta'-\gamma')} \tag{6.89}$$

$$= \frac{(C-A)(\beta-\gamma)-(C-B)(\alpha-\gamma)}{(C-B)(\alpha'-\gamma')-(C-A)(\beta'-\gamma')}. \tag{6.90}$$

From the above equations of ξ and ω, we can clearly see that the DKP choice of flux coefficients as stated in the previous section, namely: $\alpha = \beta = \gamma, \alpha' = \beta' = \gamma'$ and $A = B = C$ is inconsistent with the extremisation equations obtained for both ξ and ω. This particular choice of parameters leads to undefined ξ and ω. This is one of the main reasons why we think that the DKP solutions, for model II, are problematic and that it is impossible to achieve numerically viable minima starting from their solutions.

Another expression for the modulus u can be derived from Eq.(6.63), which in turn, should be consistent with Eq.(6.84),

$$u^2 = -\frac{\alpha+\beta+\gamma+(\alpha'+\beta'+\gamma')\omega}{\delta+\delta'\omega}. \tag{6.91}$$

The modulus $s = \mathrm{Re}\, S$ can also be expressed, in terms of the flux parameters, as

$$s = -\frac{(\alpha+\beta+\gamma+\delta u^2)\xi}{((\alpha'+\beta'+\gamma'+\delta' u^2)\xi + A + B + C + Du^2)\omega(S)}. \tag{6.92}$$

We have obtained all the extremisation equations for the moduli fields present in this model. The existence of more than one equation for the directions ξ, u and ω makes it more difficult to search for numerically viable minima since the flux parameters, entering these equations, have to be fixed at certain values satisfying all equations without any inconsistencies. We have a large number of flux coefficients in this model, which means that phenomenologically there are many choices in parameter space that satisfy the above equations. Here, we are only interested in one of these choices which is presented in Tables 6.3, 6.4, where the values of the flux coefficients as well as moduli fields are stated.

Parameter	μ	α	β	γ	δ	α'	β'	γ'	δ'	A	B	C	D
Values	-2.756	2	1	6	45	2	1	1	6	$50\,i$	$40\,i$	$30\,i$	0

TABLE 6.3: One possible choice of parameters present in model II.

Moduli	$\omega(S)$	$\mathrm{Im}\,\xi$	u	$\mathrm{Re}\,S$	$\mathrm{Im}\,S$
Values	-6	-12	1.29	1.25	0

TABLE 6.4: Numerical solutions to the moduli corresponding to the choice of parameters in Table 6.3.

For the above numerical solutions to be viable, we need to examine the structure of the scalar potential, which can be derived according to Eq.(5.11), along the relevant moduli fields. Fig.(6.5) shows a plot of the scalar potential as a function of the complex field U_1, while fixing the other moduli fields at their minimum values. As expected, the minimum lies exactly at the numerical solution for u ($\mathrm{Re}\,U_1 = u = 1.29$) with a vanishing imaginary part ($\mathrm{Im}\,U_1 = 0$). Similar plots can be achieved along the remaining directions and all of them show the global minimum at the values given in Table 6.4. To ensure the existence of this minimum, we evaluate the Hessian matrix. Although the analysis of model II suggests the existence of a minimum. The hessian matrix is not positive definite in this case. This means that the solutions presented for this model do not correspond to a minimum in all directions.

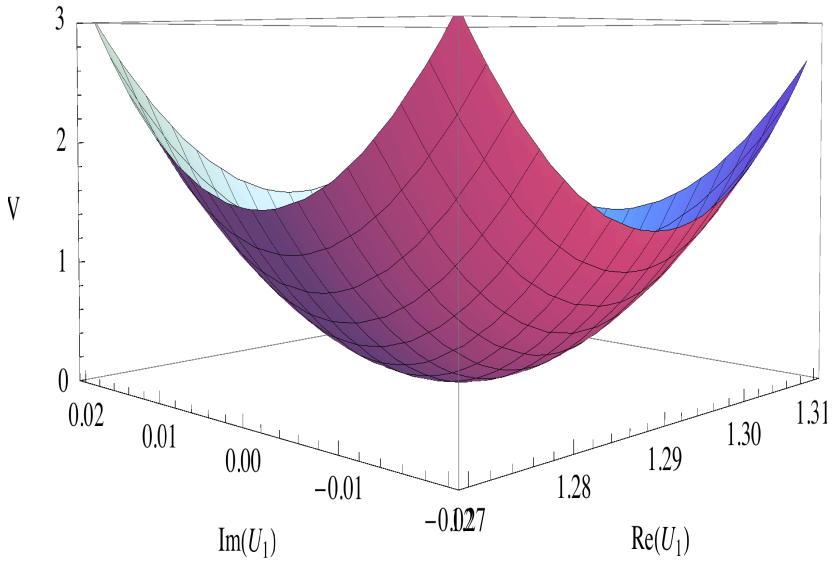

FIGURE 6.5: The scalar potential as a function of $\mathrm{Re}\,U_1$, $\mathrm{Im}\,U_1$.

We have found consistent solutions for model II. However, evaluating these solutions as well as studying the dynamics of the corresponding moduli fields numerically, is extremely costly in terms of time. This is mainly due to the large number of flux parameters present in the model (about twelve). For this reason, we will not comment on this model any further and instead we will look at a simplified version of the model studied first by Löwen et al. [65]. Their model has the same features as model II but with less moduli fields and flux coefficients.

6.4 Model III (LNZ model)

In this section we study a model presented in [65], which covers the key features of model II discussed in the previous section.

Consider the following superpotential which is similar to the one presented in Eq.(6.57) but with only one U field:

$$W = 3\hat{A}U + \hat{D}U^3, \tag{6.93}$$

with the Kähler potential: $K = -\ln(T_A + \overline{T_A}) - \ln(S + \overline{S}) - 3\ln(U + \overline{U})$. As in model II, the following functions of T_1, T_2 and S are introduced:

$$\hat{A} = (\alpha + \alpha'\omega(S))\xi + A\omega(S), \tag{6.94}$$

$$\hat{D} = (\delta + \delta'\omega(S))\xi + D\omega(S), \tag{6.95}$$

with $\xi = T_1 - T_2$ and $\omega(S) = \mu^3 e^{-S}$.

6.4.1 LNZ solutions

We start by identifying the moduli that break Supersymmetry. These are the same as those presented for model II, namely: T_1, T_2 and T_3. The directions that preserve it are S and U in this case. The conditions $\langle W_{T_1} \rangle = \langle W_{T_2} \rangle = 0$ can be expressed as,

$$(\alpha + \alpha'\omega(S)) + (\delta + \delta'\omega(S))U^2 = 0. \tag{6.96}$$

Looking at Eq.(6.96), we find that the stationary point condition ($\partial_j V = 0$), similar to the previous models, can be expressed as $\mathrm{Re}\,\xi = 0$. We will not go through all the steps of deriving the stabilisation equations, for S and U here,

since the analysis is very similar to that presented for model II. We choose $S = s - i\pi/2$ and $U = u$ real. This choice, together with the requirement that the flux parameters α, δ and A, D are real while α', δ' are imaginary, makes everything consistent.

The vanishing of the first derivatives of the superpotential W, with respect to T_1 and T_2, at the vacuum (given by Eq.(6.96)) guarantees that the requirement $\langle V \rangle = 0$ is fulfilled. Similar to model II, the modulus T_3 does not feature in the superpotential (flat direction). Eq.(6.96) leads to the following equation for u,

$$u = \sqrt{\frac{-(\alpha + \alpha'\omega(S))}{(\delta + \delta'\omega(S))}}. \tag{6.97}$$

Another equation for u and minimisation equations for $s = \mathrm{Re}\, S$ and ξ are given by Eqs.(6.84, 6.76, 6.77). These are achieved by expressing the vanishing F-auxiliary equations along these directions as shown in the previous section.

The gravitino mass can also be expressed by Eq.(6.81) and in the special case ($\alpha' = i\alpha,\ \delta' = -i\delta$), by Eq.(6.82). The authors of [65] argue that, in order to obtain a phenomenologically attractive gravitino mass, the position of the minimum in the S direction must be shifted to larger values, for example $S = 15 - i\pi/2$. They also claim that a Minkowski vacuum is obtained with the following set of flux coefficients:

$$\alpha = 100,\ \ \delta = -100,\ \ A = 10,\ \ D = -10.00001, \tag{6.98}$$

where they considered a fine-tuning of parameters of order $A\delta - D\alpha \approx 10^{-3}$. This choice of parameters gives a gravitino mass of order $1.11 \times 10^{-14} M_p$. Löwen et al. also claim that the gravitino mass is doubly suppressed since it is, like that expressed for model II, proportional to ω^2 as shown in Eq.(6.82). Further to our discussion for model II, we think that the presence of ω^2 does not really guarantee a viable phenomenological result for the gravitino mass. There is also a problem of inconsistency in Eq.(6.77) for the value of $s = 15$. We found that, for this equation to be satisfied exactly, s should be of order $s = \mathrm{Re}\, S = 15.1857$. Even with this correction to the value of s, plots of the corresponding scalar potential as a function of $\mathrm{Re}\, S$ show no Minkowski minimum as can be seen in Fig.(6.6). Fig.(6.7) shows another plot of the scalar potential with respect to $\mathrm{Re}\, S$ and $\mathrm{Re}\, U$. In this figure, the minimum along the $\mathrm{Re}\, U$ direction is clear while nothing is observed along the $\mathrm{Re}\, S$ direction.

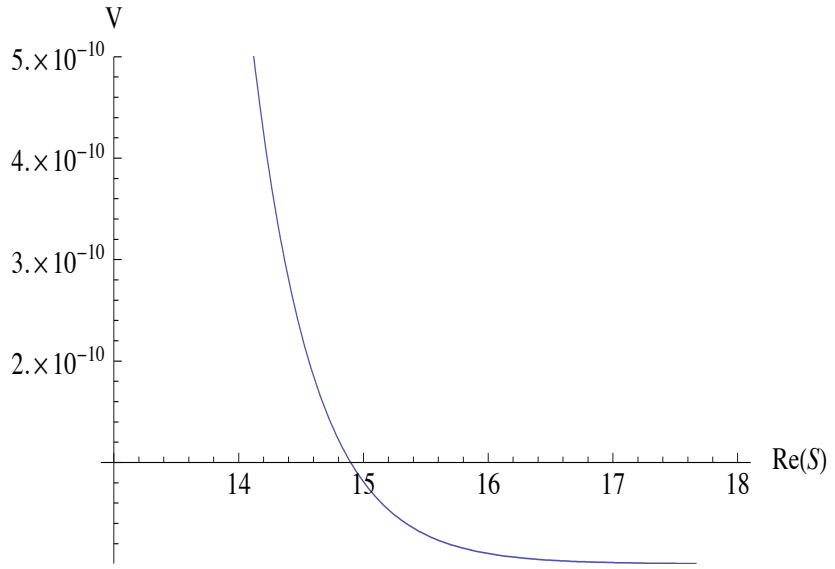

FIGURE 6.6: The scalar potential for model III as a function of $\mathrm{Re}\, S$.

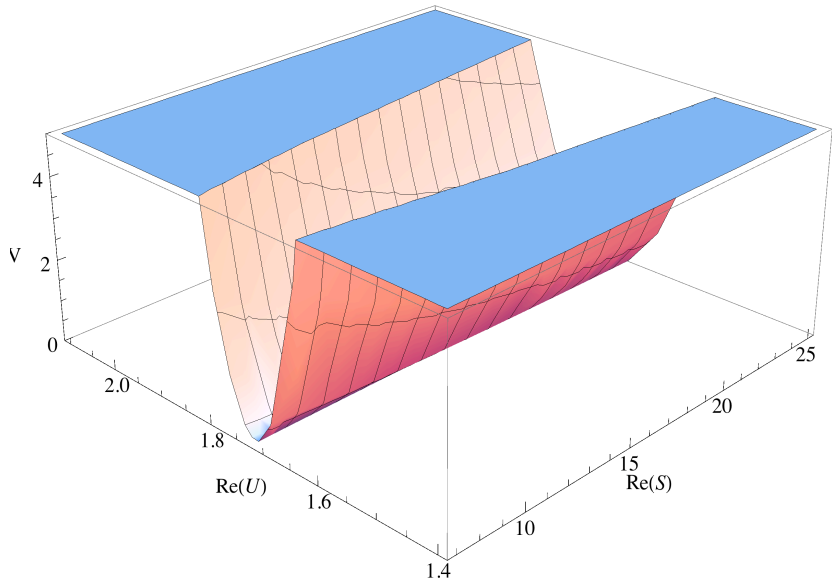

FIGURE 6.7: Stabilising potential for model III as a function of $\mathrm{Re}\, S$, $\mathrm{Re}\, U$.

So far we have analysed the numerical solutions of Löwen et al., and found that their choice of flux coefficients, particularly the case ($\alpha' = i\alpha, \quad \delta' = -i\delta$), does not give rise to a Minkowski minimum in all directions. In the next section, we look at an alternative choice of flux parameters to see whether it gives rise to a Minkowski vacuum.

6.4.2 Alternative solutions

As discussed in the previous section, the stationary point condition reads $\mathrm{Re}\,\xi = 0$. We choose the same value of $\mathrm{Im}\,S$, $S = s - i\pi/2$, and we also take the fields U to be all real ($U = u$). The solutions for s, ξ and u are given by Eqs.(6.76, 6.77, 6.84, 6.97) respectively. For the choice of the flux coefficients, we require α, δ, A and D to be real while α' and δ' to be imaginary. However, the special case $\{\alpha' = i\ \alpha, \quad \delta' = -i\delta\}$ is no longer considered in what follows.

For all the equations to be consistent, we require $D = 0$. Our numerical choice of flux coefficients is given as:

$$\alpha = -2,\ \delta = 45,\ \alpha' = -3\ i,\ \delta' = 135.70656\ i,\ A = 5$$

The flux parameter δ' is tuned in order to get a Minkowski minimum since there is only one value of δ' that satisfies the equation $\langle V \rangle = 0$, which is one of the conditions required for finding a stationary point where Supersymmetry breaks in Minkowski space [64]. The above choice of the flux parameters, together with a value of μ of order 1 gives the following values of the relevant moduli fields at the minimum:

$$\mathrm{Re}\,S = 1.25, \quad \mathrm{Re}\,U = 0.747, \quad \mathrm{Im}\,\xi = 0.314.$$

To see whether these solutions correspond to a minimum, the scalar potential is plotted as a function of $\mathrm{Re}\,S$ as shown in Fig.(6.8). Now, we can clearly see a minimum along the S direction, which appears to be around $\mathrm{Re}\,S = 1.25$. We can also see a minimum in the complex U plane as presented in Fig.(6.9).

We showed how changing the flux parameters, for model III, gives rise to a viable minimum along the directions $T_1 - T_2, S$ and U. However, this model is not free of flat directions ($T_1 + T_2, T_3$) just like the DKP models. In order to have a phenomenologically attractive model, we need to ensure the stabilisation of all moduli. This can be achieved by uplifting the flat directions, following the same

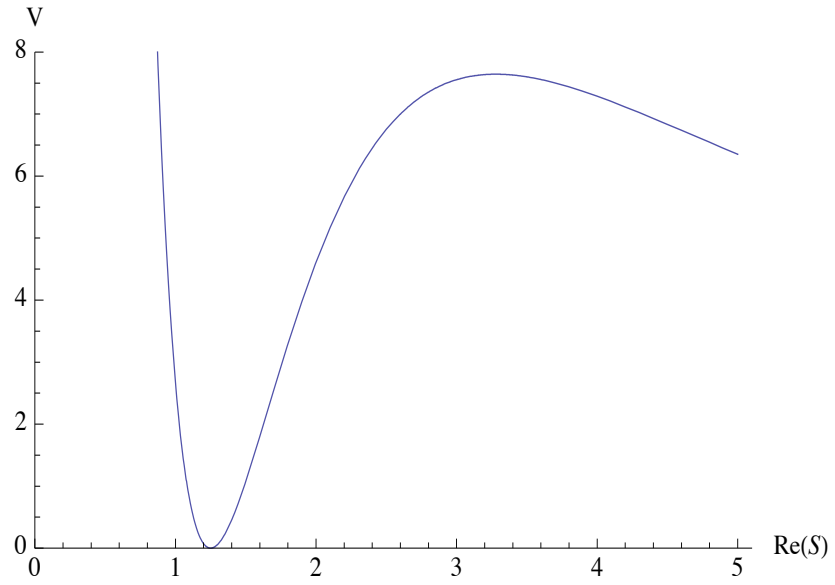

FIGURE 6.8: The scalar potential, for model III, as a function of $\mathrm{Re}\, S$. All the other minima are fixed at their minimum values

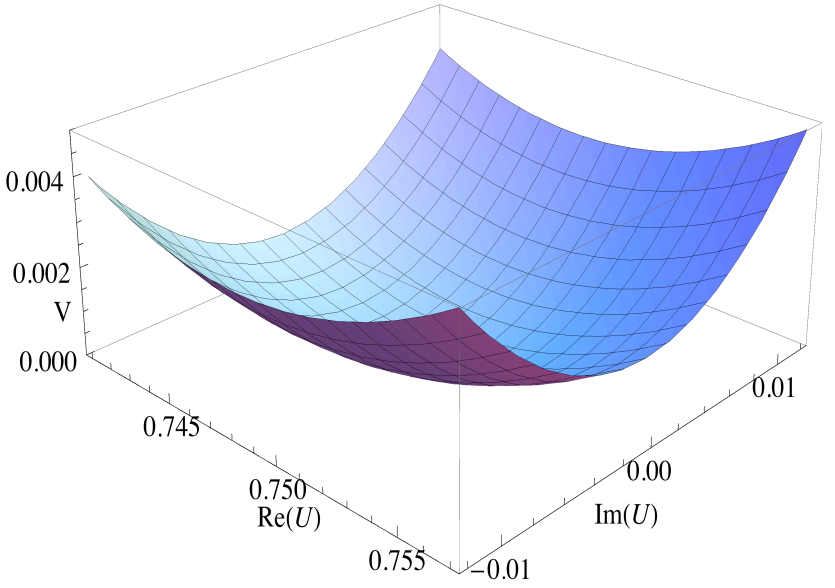

FIGURE 6.9: The scalar potential, for model III, as a function of $\mathrm{Re}\, U$, $\mathrm{Im}\, U$. All the other minima are fixed at their minimum values

procedure as described in Section 6.2.2, which was also discussed in [65]. Fig.(6.10) shows a plot of the stabilising potential for the modulus T_1, after uplifting the flat directions, displayed in the complex plane.

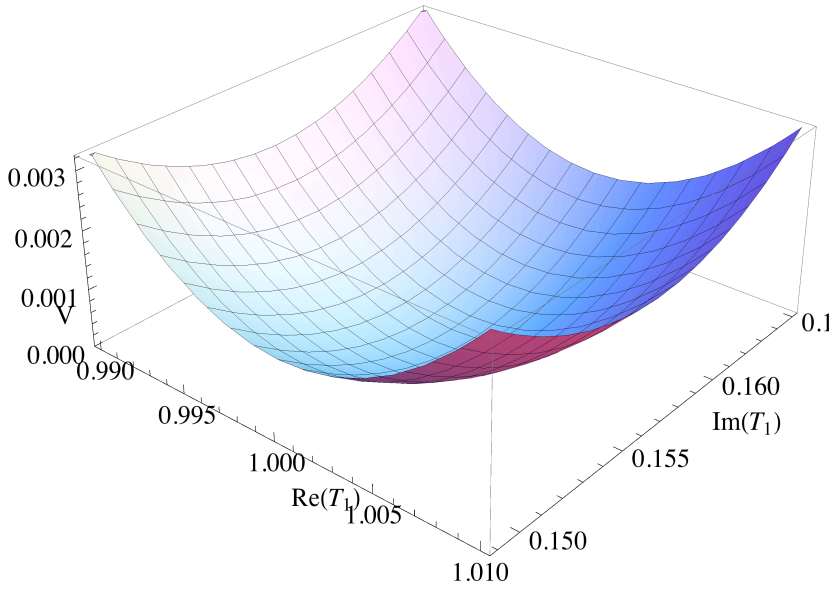

FIGURE 6.10: The scalar potential, derived for model III after uplifting the flat directions, as a function of $\mathrm{Re}\, T_1$, $\mathrm{Im}\, T_1$.

Similar to the models presented earlier in this chapter, the calculation of the Hessian matrix is very important for identifying the existence of the Minkowski minimum for this model. Evaluating the Hessian matrix, we found that our solutions correspond to a Minkowski minimum in all directions as presented in Appendix C.

6.5 Summary

In this chapter, we studied moduli stabilisation analytically and numerically in three different models originating from heterotic and type IIA string compactifications on $T^6/Z_2 \times Z_2$ orientifolds. We analysed the Supersymmetry breaking conditions proposed by Derendinger et al. which involve two categories of moduli. One of them breaks Supersymmetry while the other moduli preserve it. Then, we presented the problematic aspects of models II and III, which were first analysed by Derendinger et al. and Löwen et al. respectively, and gave ways of resolving them, essentially, by choosing different values of the flux parameters present in each model. These models can only be phenomenologically viable if all the moduli

fields are stabilised. To achieve this, we also presented a way of uplifting the flat directions in these models by introducing a correction to the Kähler potential.

Moduli stabilisation plays an important role in cosmological inflation. Each of the moduli fields present in a particular four dimensional theory can play the role of an inflaton and their dynamics may give rise to successful inflationary scenarios upon the fulfilment of some conditions. To see how this idea applies to the models studied so far, we will proceed in the next chapter by looking at the dynamics of the moduli fields, for each model, and commenting on their evolutions and on whether they can be good inflaton candidates.

Chapter 7

Inflation

Due to the advancement in observational cosmology, it is of great importance to develop our theoretical models in order to understand the current astronomical data and their implications. One promising field, which is the dominant theory for the origin of structure of our universe, is cosmological inflation [68, 69, 70]. Inflation refers to a period in the history of the universe where there was an exponential expansion with an accelerating scale $a(t)$. It solves many problems, including the horizon problem, which refers to the difficulty in understanding the large-scale of homogeneity observed in our universe. Inflation gives rise to definite predictions, not only for the uniformity of the universe, but also for possible deviations from this uniformity. It also solves the flatness problem, which is concerned with the ratio, Ω, of the actual density of the universe and the critical density being close to one. The critical density is defined as the density that causes our universe to be spatially flat. Another problem that can be solved by Inflation is that of magnetic monopoles. These are extremely massive particles which would outweigh everything in the universe. In recent years, there has been many attempts to realise inflation within string theory. In this chapter, we look at inflationary scenarios in the framework of the models discussed in Chapter 6.

7.1 Inflation in string theory

There has been steady progress in the constructions of inflationary models originating from string theory in the context of flux compactifications and moduli stabilisation. This is realised at the level of $\mathcal{N} = 1$ Supergravity, where moduli

are complex scalar fields. As stated in Chapter 6, for any realistic model, Supersymmetry must be broken and the stabilisation of all moduli fields at the right scale must be achieved. Models of inflation include brane inflation [71, 72]. this is a class of models where the inflaton field is associated with the scalar fields describing relative positions of branes in the compactified space. This particular type of models does not fall within the scope of this thesis, however, and hence will not be discussed further in this thesis.

Modular inflation is realised with one (or several) moduli fields, which result from string compactifications, playing the role of the inflaton field. These models are conceptually simpler than brane inflation models and do not require the existence of brane dynamics. In some models of modular inflation, the inflaton field may be associated with many scalar fields which mark the end of inflation when rolling down to their minimum values. There are many successful models of modular inflation such as racetrack inflation [73, 74, 75] and large volume Kähler inflation [76]. In these models, it is possible to achieve either Minkowski or de Sitter (dS) vacua.

In general, inflation occurs in a complicated multi-dimensional space as it is the case with string models. The models considered in this thesis fall into this category, where the evolution is not necessarily driven by one inflaton field. In some cases, it is possible to study multi-dimensional models as those with one single inflaton field by choosing one moduli direction and freezing the remaining fields at their minima. Despite the success of the inflationary models proposed to date, it is still very hard to establish inflationary scenarios in controlled compactifications without facing problems. Particularly the problem of runaway moduli, which occurs mainly due to the steepness of the scalar potential. In addition to this, there is the initial conditions problem. It is very important to find regions in parameter space which, starting the inflaton field at them, lead to successful periods of inflation with at least 60 e-foldings. In string theory models, the problem of initial conditions becomes more complicated particularly in cases where there are more than one inflaton field driving inflation.

Among the models proposed so far is eternal inflation [77]. This is defined, simply, as a period of inflation that never ends. Eternal inflation involves a false vacuum (metastable vacuum) decaying exponentially in a particular moduli direction, just like the decay of a radioactive substance. This decay causes the inflaton field to move up its potential, to the top of a barrier existing between such a vacuum and

another minimum. As this vacuum expands exponentially, its volume continues to grow with time.

The idea of eternally inflating universes was seen as an oddity for many years. This picture, however, has greatly changed after realising that string compactifications give rise to hundreds of metastable vacua with varying four dimensional physics. All of these vacua exist without the presence of any mechanism that favours one over the other. The study of eternal inflation may provide such a mechanism of vacuum selection and may, eventually, help in understanding the vast landscape of string vacua. However, despite the progress made so far in this field, more work is needed in order to fully understand the conditions and predictions of eternal inflation.

7.1.1 Slow roll inflation

Slow-roll inflation involves a scalar field which slowly rolls down a flat potential. It may also involve more than one scalar field, in which case, the fields that are not driving inflation may be fixed at their minimum values in order to remain stable during the inflationary period. For slow-roll inflation to be successful, two conditions must be satisfied which are given as,

$$\epsilon = \frac{M_p^2}{2}\left(\frac{V'}{V}\right)^2, \tag{7.1}$$

$$\eta = M_p^2\frac{V''}{V}, \tag{7.2}$$

where M_p is the Planck mass. The derivatives of the potential V are with respect to the inflaton field (ϕ). Both of these parameters are required to be very small ($|\eta|, \epsilon \ll 1$) for inflation to occur. From now on, we will refer to ϵ and η as slow-roll parameters.

In string theory, there are many scalar fields and therefore the inflaton represents one real component of some complex scalar field (Φ). It is useful to express these parameters in complex field basis $\{\Phi^a\} = (\Phi^i, \overline{\Phi}^{\bar{j}})$ [75],

$$\epsilon = \left(\frac{K^{i\bar{j}}\,\partial_i V \partial_{\bar{j}} V}{V^2}\right), \tag{7.3}$$

$$N^a{}_b = \begin{pmatrix} N^i{}_j & N^i{}_{\bar{j}} \\ N^{\bar{i}}{}_j & N^{\bar{i}}{}_{\bar{j}} \end{pmatrix}, \tag{7.4}$$

where

$$N^{i}{}_{k} = \frac{K^{i\bar{j}}\partial_{\bar{j}}\partial_{k}V}{V}\,, \qquad N^{k}{}_{\bar{i}} = \frac{K^{k\bar{j}}(\partial_{\bar{i}}\partial_{\bar{j}}V - K^{l\bar{n}}\partial_{\bar{i}}\partial_{\bar{j}}\partial_{l}K\,\partial_{\bar{n}}V)}{V}\,. \tag{7.5}$$

$N^{\bar{i}}{}_{\bar{j}}$ and $N^{\bar{k}}{}_{i}$ can be obtained from the above equations of $N^{i}{}_{k}$ and $N^{k}{}_{\bar{i}}$ by complex conjugation. In this basis, the η parameter is the smallest negative eigenvalue of the matrix $N^{a}{}_{b}$. To have a successful inflationary scenario, it is also required that the number of e-folds N_e is more than 60. N_e can be written in terms of the values of the scale factor at the start and end of inflation as,

$$N_e = \ln\left(\frac{a(t_f)}{a(t_i)}\right). \tag{7.6}$$

In general, it is difficult to achieve a small value of the parameter η in models originating from string theory. This is known as the η problem. To see why this parameter is not small enough we consider the expression for the F-term scalar potential which is given as,

$$V_F = e^{K}(K^{ij}D_iW D_{\bar{j}}\overline{W} - 3|W|^2). \tag{7.7}$$

If we now write an expression for the η parameter using the above scalar potential, we find that it is proportional to the second derivative of the Kähler potential due to the presence of the e^K factor in the potential. Considering a simple Kähler potential, for example $K = \phi\overline{\phi}$ where ϕ is a complex field, we can easily see that the parameter η becomes of order one if we take the real part of ϕ, for example as an inflaton candidate.

There are some mechanisms which have been studied in order to alleviate this situation, for instance choosing a Kähler potential which does not contain the inflaton field. In other words, if the Kähler potential is given as $K = \ln(\phi + \overline{\phi})$ for example, we can see that only the real part of the complex field ϕ is present in K (for the Kähler potential $K = \phi + \overline{\phi}$, both of the real and imaginary parts of ϕ are present), and therefore the imaginary part can be a good inflaton candidate. This applies to the models studied in this thesis as we will see in later sections. To ensure both slow-roll parameters are sufficiently small, it might be necessary to fine-tune some of the relevant parameters present in the model studied. Some models have a potential which has a saddle point near its minimum, this gives rise to a successful inflationary scenario since the condition $\epsilon = 0$ can be easily satisfied

at the saddle point with a bit of tuning to ensure η is small enough [73, 75]. These are models of topological inflation [78, 79].

In addition to satisfying the conditions imposed on the slow-roll parameters and finding an inflaton candidate, we are usually faced with the issue of initial conditions for the inflaton field. As discussed earlier, it is important to identify regions of parameter space that give rise to more than 60 e-folds. This problem becomes largely irrelevant when considering models of eternal inflation.

7.1.2 Equations of motion

We consider models that are described by a four dimensional $\mathcal{N} = 1$ effective Supergravity theory with the lagrangian,

$$\mathcal{L}_\Phi = K_{i\bar{\jmath}}\partial_\mu\Phi^i\partial^\mu\overline{\Phi}^{\bar{\jmath}} - V. \tag{7.8}$$

$K_{i\bar{\jmath}} = \partial^2 K/\partial\Phi^i\partial\overline{\Phi}^{\bar{\jmath}}$ is the Kähler metric and V is the scalar potential.

The form of the Kähler potential K, considered for the models presented in the previous chapter, is a function of the real parts of the fields only and takes the following form,

$$K = -\sum_i \ln(\Phi^i + \overline{\Phi}^{\bar{i}}), \tag{7.9}$$

where the sum is understood over all moduli Φ^i.

Considering homogeneous fields evolving in a spatially flat Friedmann-Robertson-Walker spacetime background, the equations of motion for fields ϕ^i can be written as,

$$\ddot{\phi}^i + 3H\dot{\phi}^i + \Gamma^i_{jk}\dot{\phi}^j\dot{\phi}^k + \frac{1}{2}K^{i\bar{\jmath}}\partial_j V, \tag{7.10}$$

where $\partial_j V$ is the partial derivative of the potential V with respect to the field ϕ^j, Γ^i_{jk} is the connection on the Kähler manifold and has the form,

$$\Gamma^i_{jk} = K^{i\bar{l}}\frac{\partial K_{j\bar{l}}}{\partial\Phi^k}. \tag{7.11}$$

The Hubble rate $H \equiv \dot{a}/a$, where $a(t)$ is the scale factor of the Universe, is given by the Friedmann equation

$$3H^2 = \kappa_P^2(K_{i\bar{\jmath}}\dot{\Phi}^i\dot{\bar{\Phi}}^{\bar{\jmath}} + V), \tag{7.12}$$

where $\kappa_P^2 = 8\pi G$ and G is the 4-dimensional Newton constant. Here, we set $\kappa_P^2 = 1$. The scale factor can be defined as,

$$a(t) = e^{N_e}. \tag{7.13}$$

Since we are considering complex scalar fields, it is very useful to write the equations of motions for both real and imaginary parts of the complex fields as [80]:

$$\ddot{\Phi}^i_R + 3H\dot{\Phi}^i_R + \Gamma^i_{jk}(\dot{\Phi}^j_R\dot{\Phi}^k_R - \dot{\Phi}^j_I\dot{\Phi}^k_I) + \frac{1}{2}K^{i\bar{j}}\partial_{j_R}V = 0, \tag{7.14}$$

$$\ddot{\Phi}^i_I + 3H\dot{\Phi}^i_I + \Gamma^i_{jk}(\dot{\Phi}^j_I\dot{\Phi}^k_R + \dot{\Phi}^j_R\dot{\Phi}^k_I) + \frac{1}{2}K^{i\bar{j}}\partial_{j_I}V = 0, \tag{7.15}$$

where Φ^i_R (Φ^i_I) refers to the real (imaginary) part of the scalar fields, $\dot{\Phi}^i_R$ ($\dot{\Phi}^i_I$) is the partial derivative of Φ^i_R (Φ^i_I) with respect to time and $\partial_{j_R}V$ ($\partial_{j_I}V$) is the partial derivative of the potential with respect to Φ^j_R (Φ^j_I).

7.2 Inflaton candidates

In this section, we study the evolution of the moduli fields present in models I and III which are described in Chapter.6. We shall consider different moduli directions for each model in order to find those that give rise to successful inflationary scenarios. As we shall see, in most of the cases considered, the initial values of the inflaton fields are considerably larger than the Planck scale (M_p). This is known as Large-field inflation and can be realised in certain string compactifications. Recent work on axion inflation shows that a natural mechanism known as axion monodromy, which occurs in a variety of string compactifications including Calabi-Yau orientifold compactifications of type II theories, gives rise to large-field inflation [81, 82]. This mechanism can manage corrections to the potential over Super-Plankian values. In order to check for the presence of Axion monodromy in our numerical models, it suffices to see whether the scalar potential is not periodic under a shift in the values of the axion fields; this is indeed satisfied in all the cases that we shall consider below.

7.2.1 Model I

For this model, we have seven complex fields including the dilaton field, complex structure and Kähler moduli. This means that there is a total of 14 possible directions for inflation. We will consider the evolution in all of these directions to see which ones give rise to a successful period of inflation and for which set of initial conditions.

We start by considering the evolution of the imaginary parts of the fields S, U_2, U_1 and T_3. We found that evolving these directions in pairs (for example evolving $\mathrm{Im}\, S$ together with $\mathrm{Im}\, U_1$) gives rise to successful inflationary scenarios. Inflation can also be achieved successfully by evolving each of the imaginary directions on its own and fixing the remaining ones at their minimum values. For all these moduli directions, successful periods of inflation were achieved with initial conditions within substantial regions of parameter space. Let us define the initial shift, $\delta\phi^i$, which represents the difference between the initial values of the the moduli fields and their corresponding minimum values. Looking at the case where $\mathrm{Im}\, S$ is evolved on its own, we found that 60 e-folds can be achieved for initial shift of $\delta S \geq 34$ as can be seen in Fig.(7.1).

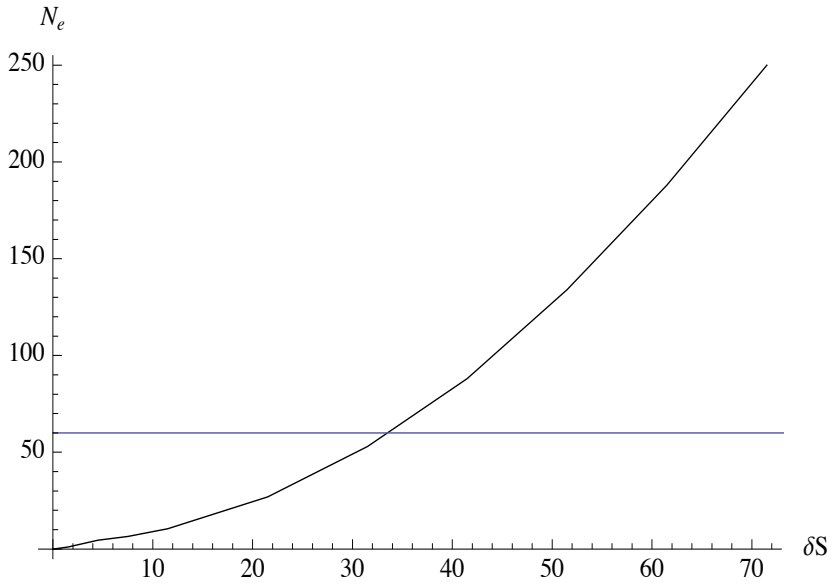

FIGURE 7.1: Total number of e-folds of inflation as a function of initial conditions of $\mathrm{Im}\, S$ with respect to its value at the minimum. The straight line indicates the 60 e-folds needed for inflation to be successful.

In similar fashion to the case of $\mathrm{Im}\, S$, the $\mathrm{Im}\, U_2$ direction can give rise to successful periods of inflation if evolved while keeping all the other fields fixed at their minima. The region of initial conditions that give successful inflationary scenarios, in this case, is $\delta U_2 \geq 12$. We can see that for the case $\mathrm{Im}\, U_2$, the region of restricted initial values is, to some extent, smaller than that of $\mathrm{Im}\, S$. By restricted initial values, we mean the region that gives less than 60 e-folds of inflation. The two remaining directions $\mathrm{Im}\, U_1$ and $\mathrm{Im}\, T_3$ behave in the exact same way when it comes to their evolution since they have the same extremisation condition and the same minimum value ($\mathrm{Im}\, U_1 = \mathrm{Im}\, T_3 = 2$) as presented in the previous chapter. When evolved each on its own, they both require an initial shift of $\delta U_1, \delta T_3 \geq 45$, for inflation to successfully occur. The above analysis shows that $\mathrm{Im}\, S$, $\mathrm{Im}\, U_2$, $\mathrm{Im}\, U_1$ and $\mathrm{Im}\, T_3$ are all good inflaton candidates. In cases where more than one direction is considered, the region of allowed initial conditions may vary depending on the fields considered. For instance, if we consider the case of evolving $\mathrm{Im}\, U_1$, $\mathrm{Im}\, S$ together, we may fix $\mathrm{Im}\, S$ at a value very close to its minimum, at $\mathrm{Im}\, S = -2$, where the minimum value in this direction is given by $\mathrm{Im}\, S = -\pi/2$. Setting $\mathrm{Im}\, U_1$ at any value within the region $\delta U_1 \geq 45$ will, in fact, result in successful periods of inflation. We will discuss this situation in more detail shortly.

7.2.1.1 Evolution along $\mathrm{Im}\, S$, $\mathrm{Im}\, U_2$

Here, we study the evolution along the two directions: $\mathrm{Im}\, S$ and $\mathrm{Im}\, U_2$, while freezing the remaining moduli at their minimum values. The results in this case also depend on the initial conditions, and inflationary scenarios with more than 60 e-foldings can be achieved for extended regions of initial values. For instance, setting $\mathrm{Im}\, U_2$ at a value not very far from the minimum ($(\mathrm{Im}\, U_2)_{min} = \pi$) at an initial value of 10 while we fix $\mathrm{Im}\, S$ initially at 32, we get more than 60 e-folds of inflation as shown in Fig.(7.2). This figure shows that the $\mathrm{Im}\, U_2$ and $\mathrm{Im}\, S$ directions settle at their minima near the end of the inflationary scenario. The slow roll parameters ϵ and η, given by Eqs.(7.1-7.5), were evaluated around 60 e-folds from the end of the inflationary period and the results were found to be very small as required ($\eta \sim 10^{-2}$ and $\epsilon \sim 3 \times 10^{-2}$).

In order to better understand the choice of initial conditions, let us examine the structure of the scalar potential along these two directions. A plot of this potential shows a number of degenerate minima with the same value of the potential $V \approx 10^{-17}$. Fig.(7.3) shows a contour plot along $\mathrm{Im}\, S$, $\mathrm{Im}\, U_2$ where we can see three of these degenerate minima aligned diagonally. The global minimum, studied in the

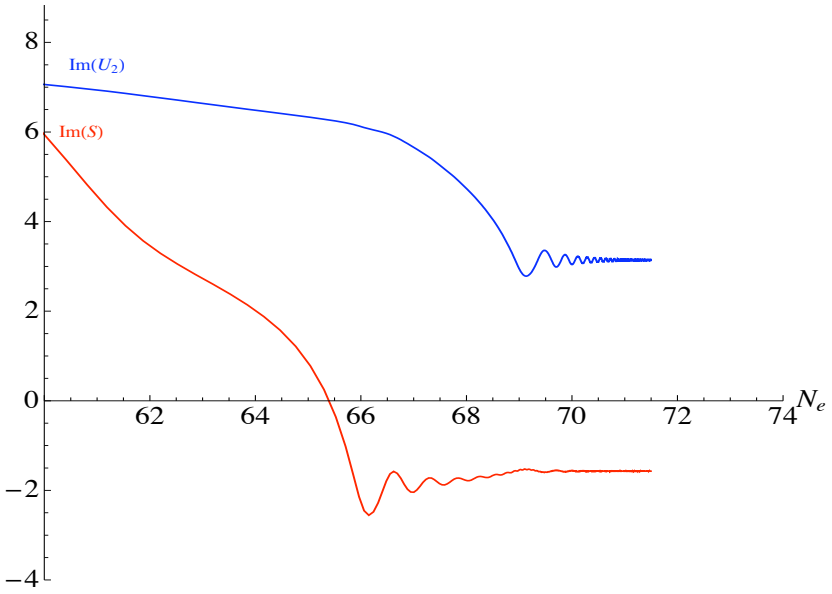

FIGURE 7.2: Cosmological evolution of $\mathrm{Im}\, S$ and $\mathrm{Im}\, U_2$ as a function of the number of e-folds, N_e, for model I. In this case, both fields evolve to the global minimum at $\mathrm{Im}\, S = -\pi/2$, $\mathrm{Im}\, U_2 = \pi$.

previous chapter, is the middle one and corresponds to the values $\mathrm{Im}\, S = -\pi/2$ and $\mathrm{Im}\, U_2 = \pi$. The other two minima are found at ($\mathrm{Im}\, S \approx 4.712$, $\mathrm{Im}\, U_2 \approx -9.424$) and ($\mathrm{Im}\, S \approx -7.853$, $\mathrm{Im}\, U_2 \approx 15.708$) respectively.

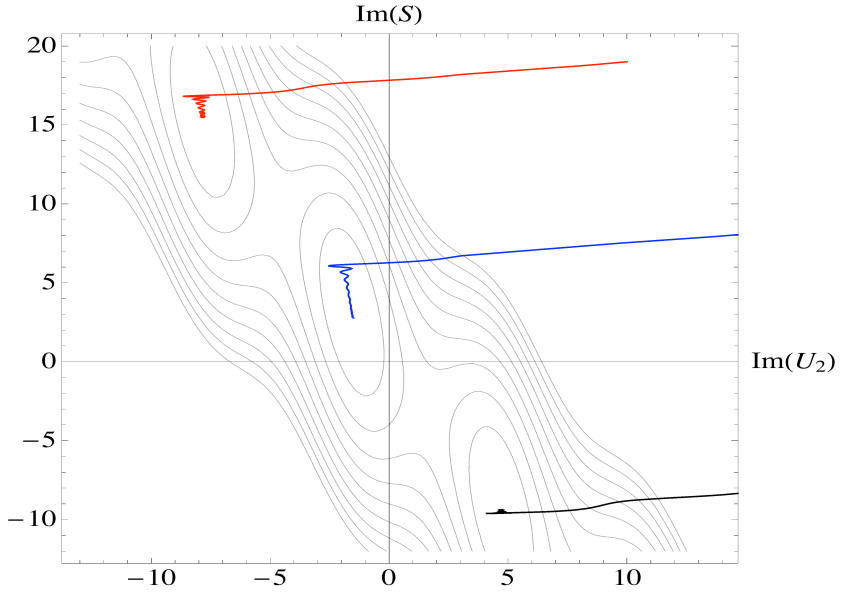

FIGURE 7.3: Contour plot of $\mathrm{Im}\, S$, $\mathrm{Im}\, U_2$ trajectories, for model I, which shows the global minimum together with two local minima.

The presence of these degenerate minima along $\mathrm{Im}\, S$, $\mathrm{Im}\, U_2$ means that the inflaton field can, in principle, evolve and settle at any one of them, depending on the initial conditions. For example, if we set $\mathrm{Im}\, U_2$ at -5 and $\mathrm{Im}\, S$ at 40, we find that both fields evolve to the minimum corresponding to $\mathrm{Im}\, S \approx 4.712$, $\mathrm{Im}\, U_2 \approx -9.424$. This minimum is the bottom one shown in Fig.(7.3). From Figs.(7.4,7.5), we can see that this evolution also lasts for more than 60 e-folds as required phenomenologically. We can also find scenarios where the two fields evolve to other vacua of the potential, which exist for larger values of the two moduli, depending on the chosen initial conditions. Since all of these minima are degenerate in energy with a value $V \approx 0$, they can all be considered as global minima. We also evaluated the slow roll parameters for the initial conditions $\mathrm{Im}\, S = 40$, $\mathrm{Im}\, U_2 = -5$ and the results were found to be $\epsilon \sim 10^{-2}, \eta \sim 5 \times 10^{-3}$.

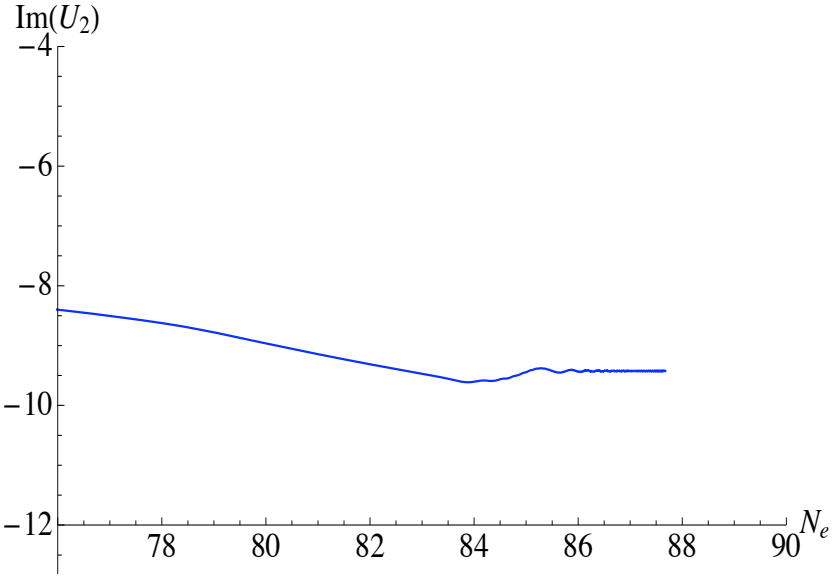

FIGURE 7.4: Cosmological evolution of $\mathrm{Im}\, U_2$ as a function of the number of e-folds, N_e, for model I. This is achieved when evolving $\mathrm{Im}\, S$, $\mathrm{Im}\, U_2$.

7.2.1.2 Evolution along $\mathrm{Im}\, S$, $\mathrm{Im}\, U_1$

After looking at the evolution along the directions $\mathrm{Im}\, S$, $\mathrm{Im}\, U_2$, we now look at the evolution along the $\mathrm{Im}\, S$, $\mathrm{Im}\, U_1$ directions while fixing the remaining moduli, including $\mathrm{Im}\, S$, at their minimum values. Comparably to the previous case, we can find successful inflationary scenarios simply by taking the fields away from their minima. Fig.(7.6) shows one of these scenarios where the inflaton fields $\mathrm{Im}\, S$, $\mathrm{Im}\, U_1$ were initially fixed at -2, 45 respectively.

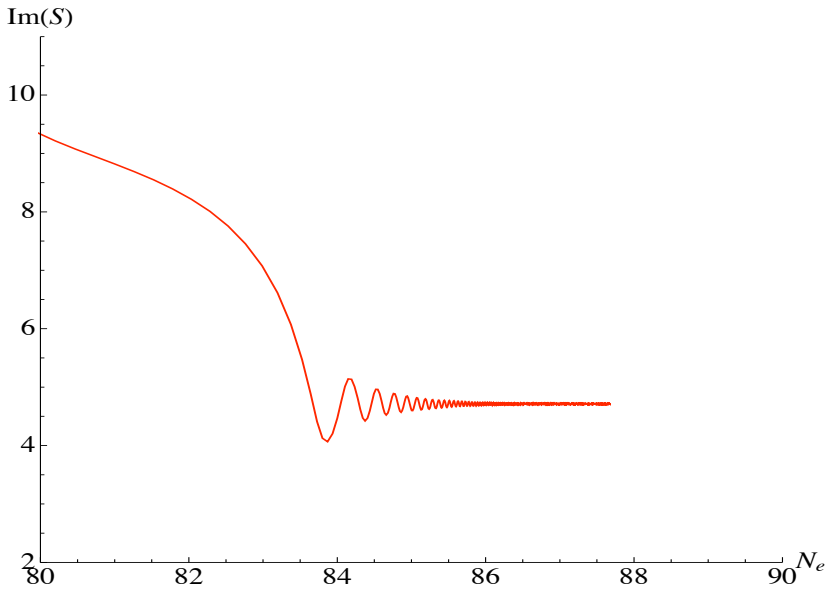

FIGURE 7.5: Cosmological evolution of $\mathrm{Im}\, U_2$ as a function of the number of e-folds, N_e, for model I. As indicated in Fig.(7.4). Both fields evolve to a minimum found at $\mathrm{Im}\, S \approx 4.712$, $\mathrm{Im}\, U_2 \approx -9.424$.

The structure of the scalar potential along these two directions is not simple since it exhibits many local minima scattered around the global one, found at $\mathrm{Im}\, S = -\pi/2$, $\mathrm{Im}\, U_1 = 0$, as shown in Fig.(7.7). The presence of these local minima is the main reason why the initial value for $\mathrm{Im}\, S$ was chosen to be very close to its minimum value ($\mathrm{Im}\, S = -2$) in the previous scenario. The small initial shift in the $\mathrm{Im}\, S$ direction ensures that inflation ends exactly at the global vacuum. Setting $\mathrm{Im}\, S$ to any other value, less than -4 for instance, while keeping the initial condition for $\mathrm{Im}\, U_1$ the same, changes the inflationary trajectories and we can see both fields evolving to a nearby local minimum instead. Fig.(7.7) shows a contour plot of the potential along these two directions where at least three local minima are apparent. Two of them are found to the left and right hand sides of the global minimum at ($\mathrm{Im}\, S \approx -10.169$, $\mathrm{Im}\, U_1 \approx -3.770$) and ($\mathrm{Im}\, S \approx 7.027$, $\mathrm{Im}\, U_1 \approx 3.770$) respectively. They are both degenerate in energy with a value of the potential given as ($V \approx 18.335$).

The presence of these local minima around the global vacuum affects the inflationary scenarios greatly. To see how these two fields evolve to one of these local minima, for example the one found at $\mathrm{Im}\, S \approx 7.027$, $\mathrm{Im}\, U_1 \approx 3.770$, we set $\mathrm{Im}\, S$, $\mathrm{Im}\, U_1$ at initial values of 8 and 15 respectively and the results are as shown in Figs.(7.8, 7.9). From these figures, we see that both fields evolve to the local minimum and settle their for a large number of e-folds without rolling down to

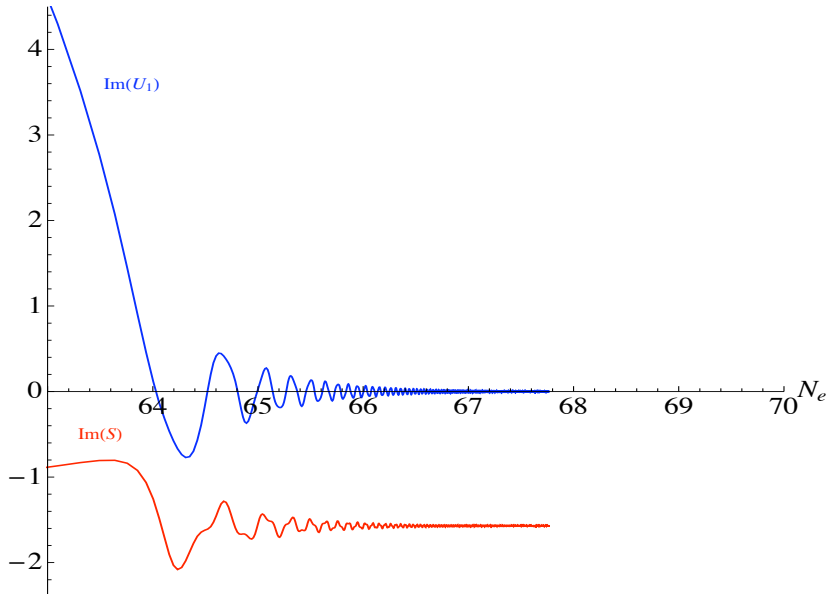

FIGURE 7.6: Cosmological evolution of $\mathrm{Im}\, S$ and $\mathrm{Im}\, U_1$ as a function of the number of e-folds, N_e, for model I. Both fields evolve to the global minimum at $(\mathrm{Im}\, S = -\pi/2,\ \ \mathrm{Im}\, U_1 = 0)$.

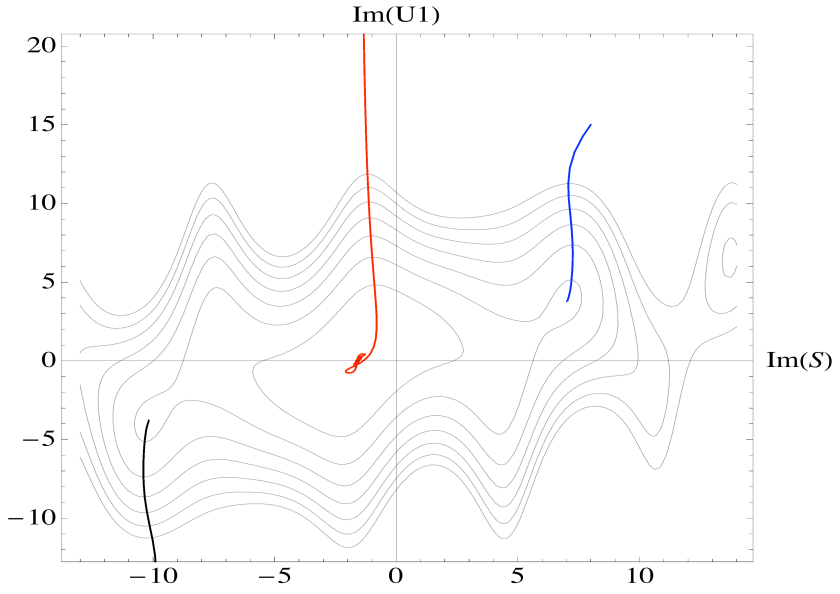

FIGURE 7.7: Contour plot of $\mathrm{Im}\, S$, $\mathrm{Im}\, U_1$ trajectories, for model I

their global minimum. This is what is known as eternal inflation. In the next section, we shall come back to this scenario again to study the probability of tunneling from the local vacuum. We evaluated the slow roll parameters ϵ and η, in this case, and the results were found to be about 2×10^{-2} and 3×10^{-2} respectively around 60 e-folds before the end of inflation.

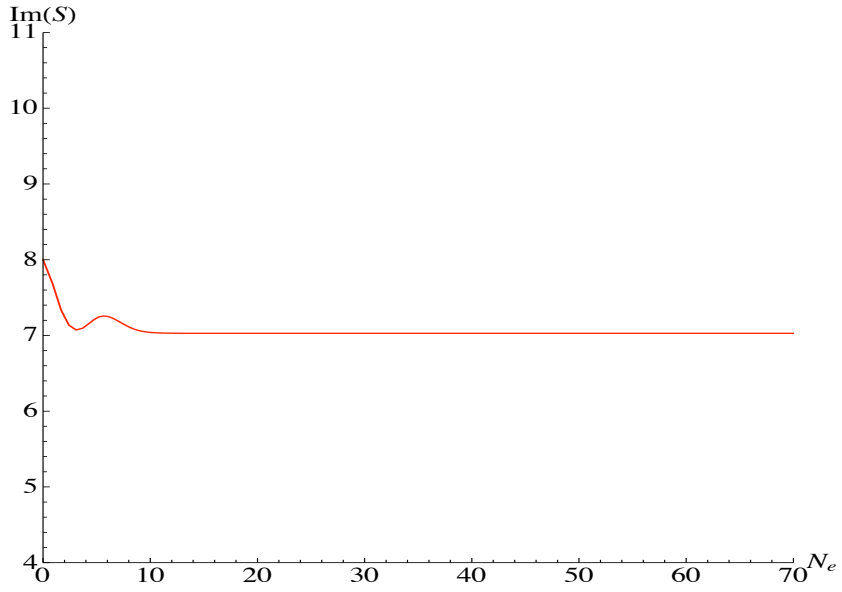

FIGURE 7.8: Cosmological evolution of $\mathrm{Im}\, S$ as a function of the number of e-folds, N_e, for model I.

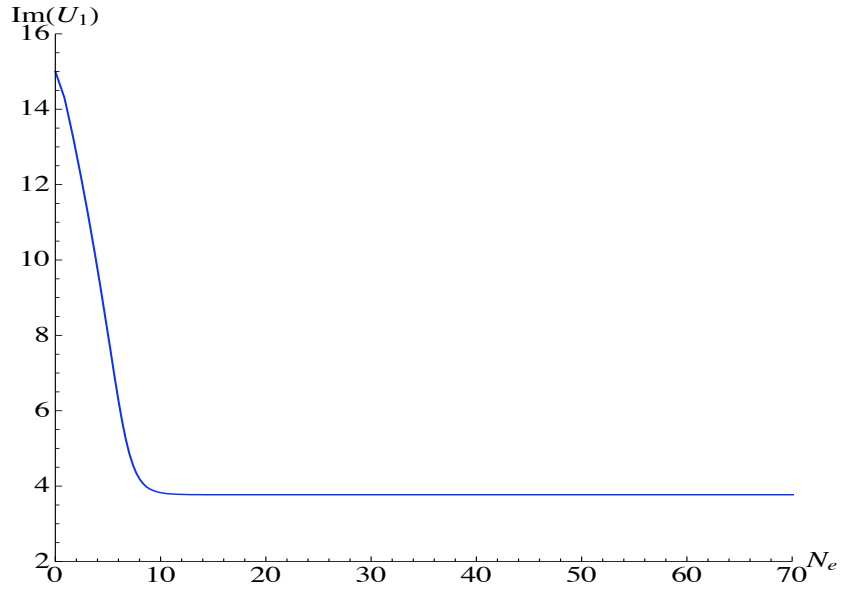

FIGURE 7.9: Cosmological evolution of $\mathrm{Im}\, U_1$ as a function of the number of e-folds, N_e, for model I. From this figure and Fig.(7.8), we see that both fields, $\mathrm{Im}\, S$, $\mathrm{Im}\, U_1$, evolve to a local minimum at ($\mathrm{Im}\, S =\approx 7.027$, $\mathrm{Im}\, U_1 \approx 3.770$).

Looking at the structure of the scalar potential along the directions $\mathrm{Im}\, S$, $\mathrm{Im}\, T_3$, we see that it is exactly the same as the case of $\mathrm{Im}\, S$, $\mathrm{Im}\, U_1$ in terms of both positions and values of the local minima as well as the global one. This is due to the fact that both U_1 and T_3 have the same extremisation equations and minimum values as mentioned earlier. For this reason, the inflationary scenarios in the $\mathrm{Im}\, S$, $\mathrm{Im}\, T_3$ directions are exactly the same as those in $\mathrm{Im}\, S$, $\mathrm{Im}\, U_1$ directions as expected.

7.2.1.3 Evolution along the remaining directions

So far, we have mainly looked at inflation along the imaginary parts of the fields S, U_1, U_2 and U_3, that is the axionic directions of the moduli fields. We found that successful inflationary periods are possible depending on the initial conditions of the relevant fields. Contrary to the imaginary parts, the real parts of these four moduli fields are not good inflaton candidates since inflationary scenarios, along them, last for just few e-folds (about 4 to 6 e-folds) whether evolved each on its own or all together. This situation is achieved regardless of the values of initial conditions. The only cases that show a successful inflationary scenario are the ones where the real part of one of these moduli fields is evolved together with the imaginary part. However, even in these cases, the real field reaches its minimum quickly before the end of inflation and therefore decouples from the inflationary dynamics. The fact that only the axionic directions are good condidates for inflation is probably due to their absence in the Kähler potential.

The remaining three fields which are namely: T_1, T_2 and U_3 are also, like the real parts of S, U_2, U_1 and T_3, not very good candidates for inflation both along their real and imaginary parts. This is not to do with the structure of the Kähler potential but is rather due to the process of uplifting the flat directions performed in the previous chapter. Uplifting the flat directions along U_3 and T_1+T_2 was local. This resulted in many singularities around the global minimum which restricts the choice of initial conditions along these directions.

7.2.2 Model III

This model contains five fields, and these are S, T_1, T_2, T_3 and U. Since only the imaginary parts of the moduli fields gave successful periods of inflation for the previous model, we start by looking at these directions first.

The structure of the scalar potential along $\mathrm{Im}\, S$, $\mathrm{Im}\, U$ directions is very similar to the case of $\mathrm{Im}\, S$, $\mathrm{Im}\, U_2$ in model I with the presence of degenerate minima which are all positioned at $\mathrm{Im}\, U = 0$ in this case as can be seen in Fig.(7.10). Similarly to the axions in the previous model, these two fields can evolve to either of these minima depending on their initial values particularly the initial value of $\mathrm{Im}\, S$. Since all the minima are positioned at $\mathrm{Im}\, U = 0$, the choice of initial conditions along this direction does not really affect the chances of the field evolving to any of these minima. Successful periods of inflation can be easily achieved by taking the fields away from their minimum values. Initial shifts of 3 and 18 for $\mathrm{Im}\, S$ and $\mathrm{Im}\, U$ respectively give more than 60 e-folds as shown in Fig.(7.11). Fig.(7.12) shows another scenario where the fields evolve to another minimum found at ($\mathrm{Im}\, S \approx 11$, $\mathrm{Im}\, U = 0$). In Fig.(7.12), we only show the evolution along the $\mathrm{Im}\, S$ direction since $\mathrm{Im}\, U$ evolves to same minimum value as the previous case ($\mathrm{Im}\, U = 0$).

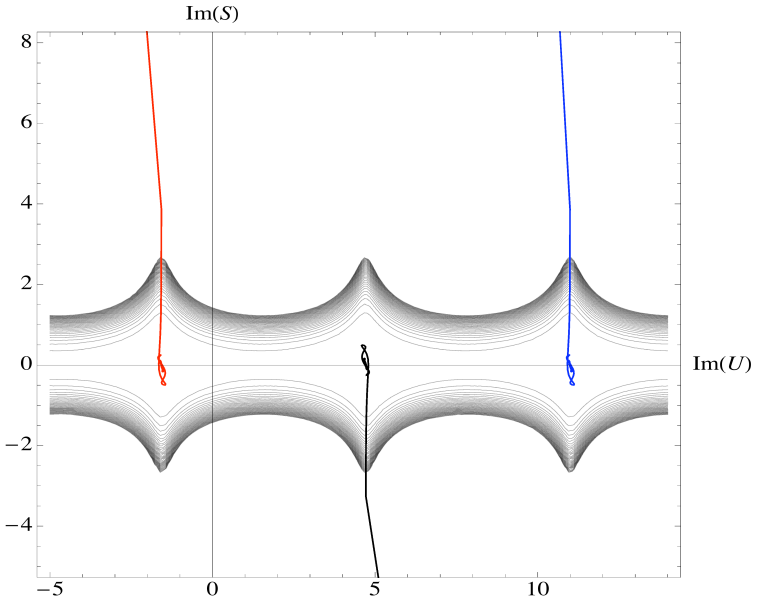

FIGURE 7.10: Contour plot of $\mathrm{Im}\, S$, $\mathrm{Im}\, U$ trajectories for model III

The real parts of the fields S and U are not good candidates for inflation, analogously to the previous model. The presence of a runaway direction along $\mathrm{Re}\, S$ prevents inflation from lasting more than 2 or 3 e-foldings. For $\mathrm{Re}\, U$, inflation only lasts up to 10 or 15 e-folds, even for large values of initial conditions. The case with the uplifted directions $T_1 + T_2$ and T_3 is similar to the previous model. The local uplifting affects the evolution in these directions and as a result, we can only choose initial conditions which are very close to the minimum values.

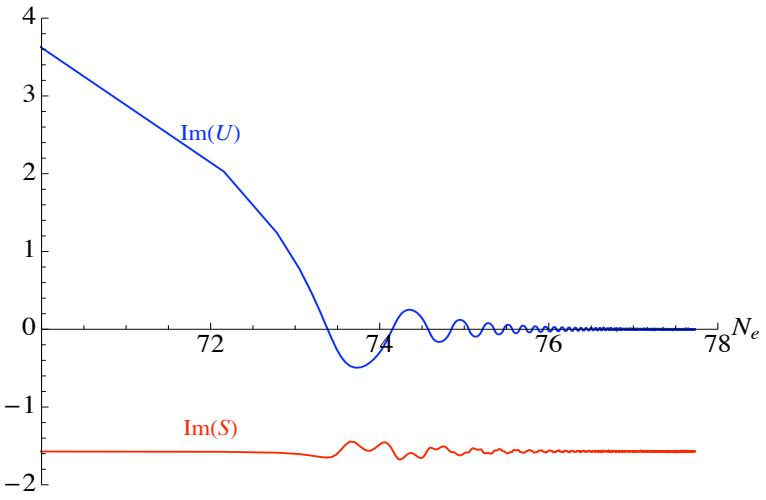

FIGURE 7.11: Cosmological evolution of $\mathrm{Im}\, S$ and $\mathrm{Im}\, U_1$ as a function of the number of e-folds, N_e, for model I. Here, both fields evolve to the global minimum at ($\mathrm{Im}\, S = -\pi/2,\ \mathrm{Im}\, U = 0$).

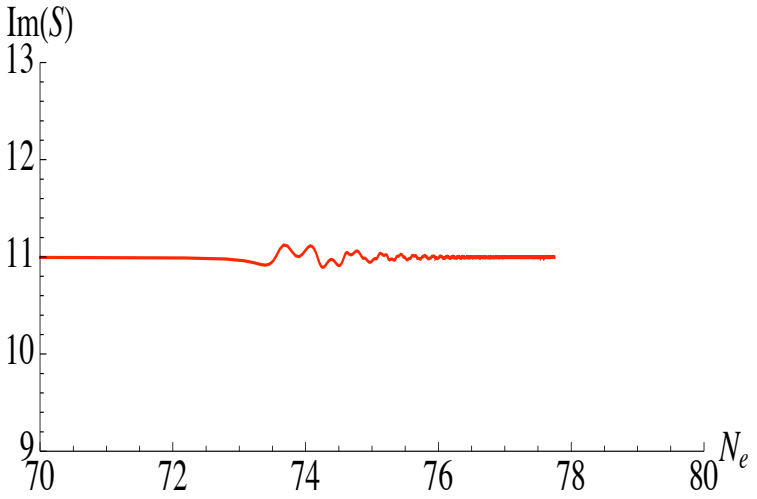

FIGURE 7.12: Cosmological evolution of $\mathrm{Im}\, S$ as a function of the number of e-folds, N_e, for model I. This is achieved when evolving $\mathrm{Im}\, S$ and $\mathrm{Im}\, U$ together and they both settle at the vacuum $\mathrm{Im}\, S = \approx 11$, $\mathrm{Im}\, U = 0$.

After studying the evolution of the moduli fields present in both models, we found that the results are very similar except for the case of local minima. These minima, found along $\mathrm{Im}\, S$, $\mathrm{Im}\, U_1$ directions in model I, do not appear in this model. To understand this effect, we shall analyse another model originating from type IIA theory compactifications (presented in [64]) in the next section.

7.2.3 Introducing model IV

To understand the difference in the structure of the scalar potential between model I and model III, we look at another DKP model (model IV) originating from IIA string compactifications with a superpotential given as,

$$W = (T_1 - T_2)(U_1 + U_2 + bU_3 + gU_1U_2(U_3 - i\pi) - 2bS) + (U_1U_2 - L)\omega(S) \quad (7.16)$$

where $\omega = \mu^3 e^{-S}$ and $\xi = T_1 - T_2$ as presented in Chapter 6. Most of the moduli fields are present in this model with two flat directions along T_3 and $T_1 + T_2$. Without repeating the procedure of stabilisation along these moduli fields, we list minimum values in Table.7.1, which represent one choice of solutions for the minimisation equations of these fields. From the minimisation conditions, we choose $\mathrm{Im}\, U_3 = \pi$ and $\mathrm{Im}\, S = \pi/2$. We also take both moduli U_1 and U_2 to be real ($\mathrm{Im}\, U_2 = \mathrm{Im}\, U_1 = 0$). The value of the scalar potential at this minimum is $V_{min} \approx 9.683 \times 10^{-17}$.

Parameter/ Moduli	L	g	b	μ	$\mathrm{Re}\, U_1$	$\mathrm{Re}\, U_2$	$\mathrm{Re}\, U_3$	$\mathrm{Re}\, S$	$\mathrm{Im}\, \xi$
Values	3.57	-3	2	1	4	4	0.033	1.618	0.806

TABLE 7.1: One particular choice of numerical solutions to model IV.

We will not comment further on this minimum since we are more interested in the structure of the scalar potential along some directions of the moduli fields, particularly S, U_1 and U_2. The reason for choosing these fields is mainly due to the fact that they enter the superpotential, given by Eq.(7.16), in the same way as the fields S, U_1 and T_3 did in model I, along which we found the local minima. A contour plot of the scalar potential derived for this model and plotted as a function of $\mathrm{Im}\, S$ and $\mathrm{Im}\, U_1$ is presented in Fig.(7.13).

As can be seen from Fig.(7.13), the scalar potential of this model appears to have local minima. Two of them are found at $\mathrm{Im}\, S \sim 16$, $\mathrm{Im}\, U_1 \sim 28$ and

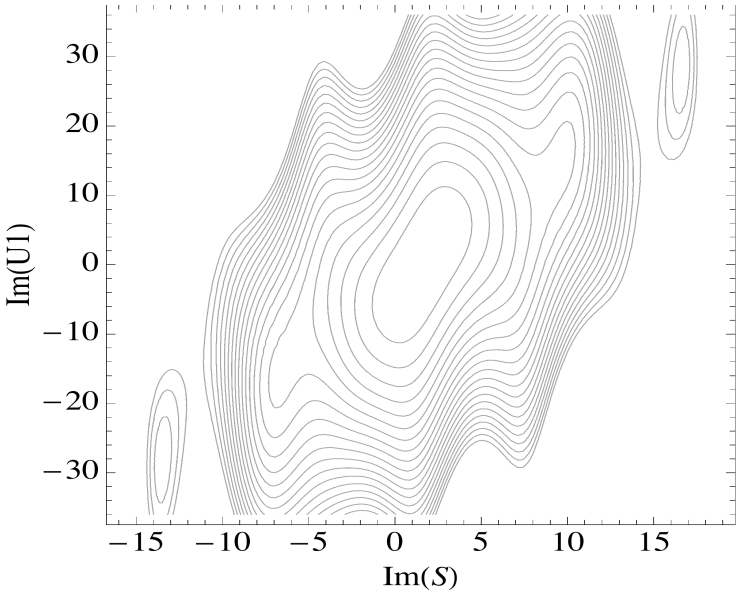

FIGURE 7.13: Contour plot of the scalar potential, for model IV, along the directions $\mathrm{Im}\, S$, $\mathrm{Im}\, U_1$.

$\mathrm{Im}\, S \sim -14$, $\mathrm{Im}\, U_1 \sim -28$. The above structure also shows two saddle points found at ($\mathrm{Im}\, S \sim 9.58$, $\mathrm{Im}\, U_1 \sim 14.73$) and ($\mathrm{Im}\, S \sim -6.45$, $\mathrm{Im}\, U_1 \sim -14.73$) respectively . The two local minima, shown in Fig.(7.13), are both degenerate in energy with a potential value of about $V \sim 200$. Clearly, more local minima can be found if we consider a larger range of values for $\mathrm{Im}\, S$ and $\mathrm{Im}\, U_1$. The structure of the potential along the directions $\mathrm{Im}\, S$, $\mathrm{Im}\, U_2$ for this model is exactly the same as the one shown in Fig.(7.13) as expected, since both U_1 and U_2 have the same extremisation equations and minimum values.

So far, we found that local minima exist for both the above model as well as model I in contrast to model III where none were found. We argue that the main reason for the different structures of the scalar potential is, not only the presence of the condensate term in model I, but also the presence of a linear term in S. On the other hand, the modulus S enters the superpotential of model III only through the condensate term. It also seems that the moduli fields which are related to the condensate term (for example $(U_1T_3 - L)\omega(S)$ in the case of model I) exhibit this structure when studied alongside S. This explains why this structure is not observed when plotting the scalar potential as a function of $\mathrm{Im}\, U_2$ and $\mathrm{Im}\, S$ in model I for example.

7.3 Tunneling from false vacuum

Moduli fields can be frozen at local minima of a multidimensional potential. Although this configuration can be classically stable, many of these vacua will tunnel to a region of lower energy density. This process, first analysed by Coleman and de Luccia (CDL) [83], involves materialisation of bubbles of a lower energy phase, which then expand eating up the original vacuum. If the spacing between true and false vacua is small, then the transition between them can be made much smaller than the bubble radius; this is known as "thin-wall" approximation.

Another approach to false vacuum decay was investigated by Hawking and Moss [84]. Hawking-Moss tunneling is dominant when the barrier between the true and false minima is broad, making gravitational effects important. To find the decay rate in this case, we consider a potential with a single scalar field $V(\phi)$, which has a true vacuum V_T at ϕ_T, a false vaccum V_F at ϕ_F and a potential barrier between the minima V_B at ϕ_B as shown in Fig.(7.14). It was shown that the probability of tunneling to the true vacuum is given by

$$P \sim \exp\left(-\frac{24\pi^2}{V(\phi_F)} + \frac{24\pi^2}{V(\phi_B)}\right), \tag{7.17}$$

which is related to the values of the potential at the top barrier as well as the false vacuum. This scenario can be realised properly in the stochastic approach to inflation [85, 86].

CDL formalism applies if [87],

$$|V''(\phi_B)|^{1/2} > 2H(\phi_B), \tag{7.18}$$

where $V''(\phi_B)$ is the second derivative of the potential evaluated at ϕ_B.

For our model, we choose to look at one of the local minima in the $\mathrm{Im}\, S$, $\mathrm{Im}\, U_1$ directions to study the probability of tunnelling to the true minimum. This local minimum is found at $\mathrm{Im}\, S \approx 7.02757$, $\mathrm{Im}\, U_1 \approx 3.77092$ with $V = 18.3352$ as can be seen in Fig.(7.15) where we denote the true vacuum with a letter B and the false minimum with A. In order to get an aligned picture of both the local and true minimum, we introduce two new directions $\mathrm{Im}\, S'$, $\mathrm{Im}\, U_1'$, which are given in

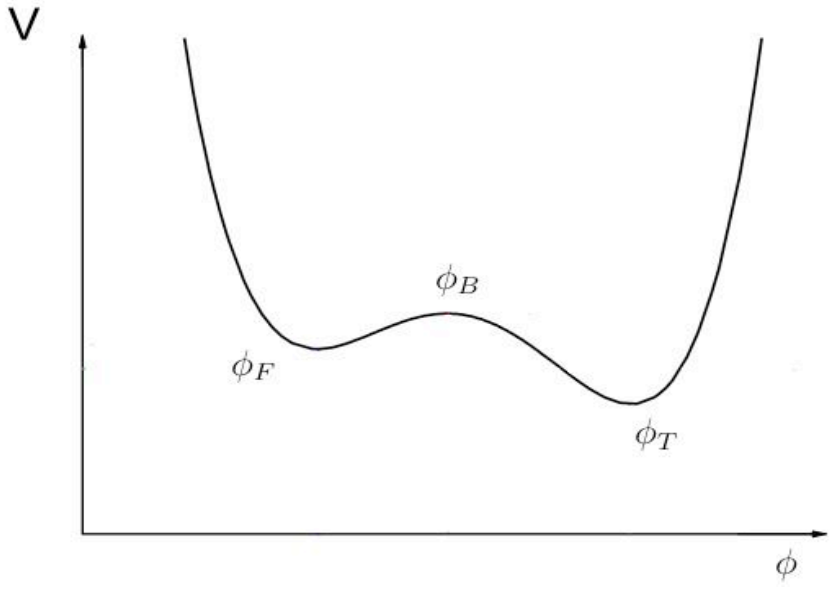

FIGURE 7.14: Potential with a true vacuum at ϕ_T and a false minimum at ϕ_F.

terms of $\mathrm{Im}\, S$ and $\mathrm{Im}\, U_1$ as:

$$\mathrm{Im}\, S' = -\frac{2.8}{\pi}\ \mathrm{Im}\, S + 4.312\ \mathrm{Im}\, U_1 \tag{7.19}$$

$$\mathrm{Im}\, U_1' = -\frac{2}{\pi}\ \mathrm{Im}\, S + 1.45\ \mathrm{Im}\, U_1 \tag{7.20}$$

Fig.(7.16) shows a plot of the scalar potential as a function of $\mathrm{Im}\, S'$ where U_i' is fixed at $\mathrm{Im}\, U_1' = 1$. The local and true minima in the $\mathrm{Im}\, S'$ direction lie at $\mathrm{Im}\, S' = 10$, $\mathrm{Im}\, S' = 1.4$ respectively. For our numerical case, the condition, given by Eq.(7.18), is not satisfied which suggests that this case is HM.

Using Eq.(7.17), the probability of tunneling to the true vacuum was estimated to be about 0.16 where values of the potential at the false minimum and top barrier are given by $V(\phi_F) \approx 18.3$ and $V(\phi_B) \approx 21.3$ respectively.

In general, a metastable de Sitter (dS) vacuum decays within a time which is exponentially smaller than the recurrence time of dS space, $t_r = e^{S(\phi)}$, where $S(\phi) = 24\pi^2/V(\phi)$ is the entropy of dS space with vacuum energy density $V(\phi)$ [54, 88]. In the case of Hawking-Moss tunneling, the decay time can be written as

$$t_{decay} = t_r \exp\left(-\frac{24\pi^2}{V_B}\right), \tag{7.21}$$

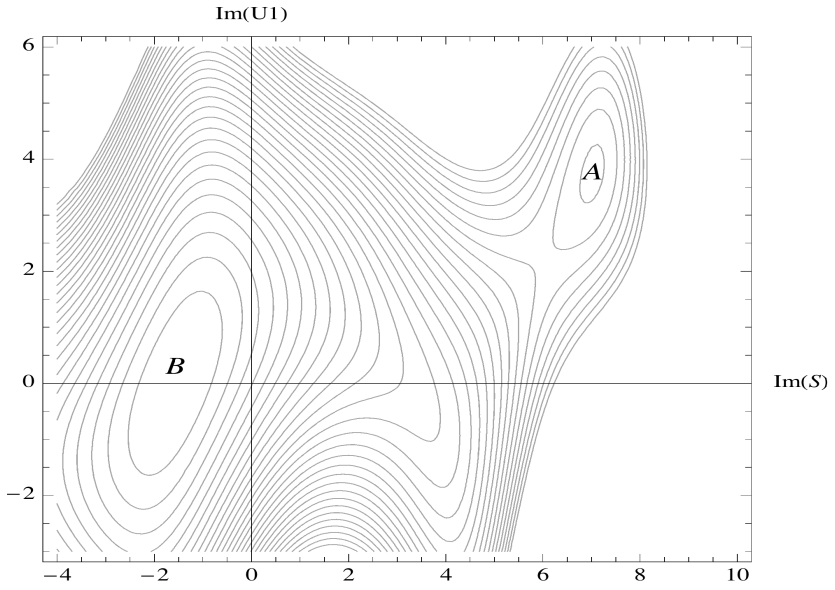

FIGURE 7.15: A contour plot along the directions $\mathrm{Im}\, S$, $\mathrm{Im}\, U_1$ for model I. The false vacuum is represented by the letter A and the true one by B.

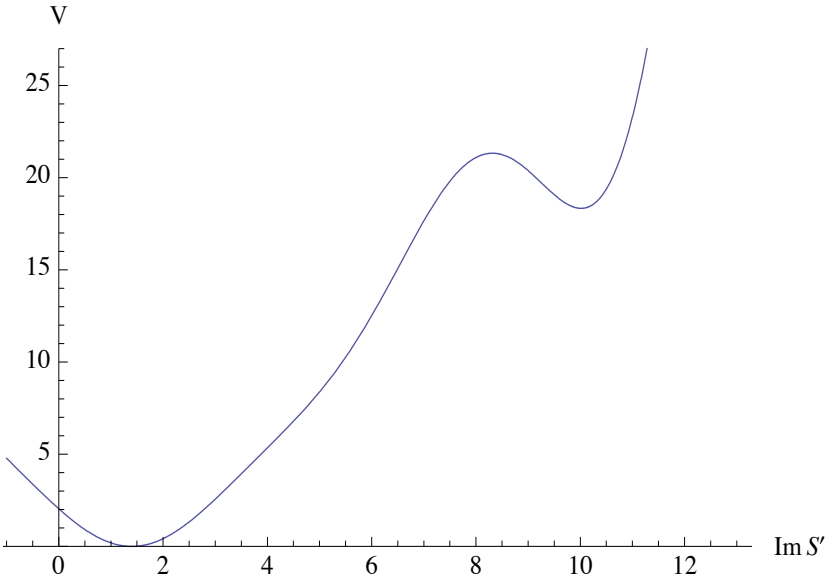

FIGURE 7.16: A plot of the potential, for model I, along the direction $\mathrm{Im}\, S'$.

where V_B is the value of the potential at the barrier between the dS minimum and the Minkowski minimum. In our numerical example, the value of the potential at the barrier between the true and false vacua is $V_B \sim 21.3$ and therefore we get:

$$t_{decay} = (1.48 \times 10^{-5}) t_r. \tag{7.22}$$

7.4 Summary

By looking at string theory based models, we aim to find those which give rise to successful inflationary scenarios and identify their predictions. In this chapter, we studied two models presented in Chapter 6, which are: model I and model III. For model I, we found that all the axionic directions of the moduli fields U_1, U_2, S, T_3 are good inflaton candidate. These gave successful inflationary scenarios with initial conditions within substantial regions of parameter space. The same result was found for model III, where we achieved successful periods of inflation along the axionic directions of the moduli U, S.

One feature, which was only observed in model I, was the presence of local minima when evolving the axionic directions of U_1 and S together. To see why this structure was only observed in model I, we introduced another DKP model (model IV) and looked at the structure of its potential along the axionic directions. We found that the same structure appears along the two directions which are related to the condensate term (in this case U_1, U_2, $(U_1U_2 - L)\omega(S)$). We concluded that this structure is only observed if the dilaton S enters the superpotential not only through the condensate term but also a linear one. We also argued that this behaviour is mainly observed along the axionic directions of those moduli which are related to the condensate term.

Finally, we studied the probability of tunneling, from the false vacuum, for one of the local minima along $\mathrm{Im}\, U_1$, $\mathrm{Im}\, S$ directions for model I. Following the Hawking-Moss procedure, the probability of tunneling was calculated and found to be quite large (about 0.16).

Chapter 8

Conclusions

This thesis concerns two aspects of physics beyond the Standard Model. The first one is studying models of neutrino mass and mixing which is presented in Part I. The second aspect is the search for viable four dimensional string inspired models and their connections with the theory of cosmological inflation as outlined in Part II.

In Chapter 2, neutrino mixing and the see-saw mechanism were briefly reviewed. We then presented a set of sum rules that result from GUT motivated models with charged lepton corrections. In Chapter 3, we reviewed the process of relating high energy see-saw parameters to low energy neutrino parameters, which we used to derive analytic expressions for the neutrino mixing angles in SD involving NLO and NNLO corrections. We also evaluated the analytic formulae, using two GUT inspired numerical models, in the cases of CSD and PCSD. As expected, the numerical results in CSD, for the neutrino mixing angles, showed small deviations from their TB values and this clearly justified why pure CSD does not give exact tri-bimaximal mixing. In PCSD with non-zero 1-1 Yukawa coupling, we found that the reactor angle, θ_{13}, was much larger than zero while the solar and atmospheric angles remained close to their TB values. This result is in good agreement with the predictions of TBR in the absence or smallness of charged lepton corrections, RG effects and canonical normalisation corrections. It also clearly agrees with the most recent experimental data [12].

In Chapter 4, we analysed the effects of Cabibbo-like charged lepton corrections and RG running on a variety of sum rules, for models where TB mixing is accurately achieved at high energy. This involved studying the RG running of various sum rules, presented in Chapter 2, for two GUT-flavour motivated models with

LSD as well as HSD. We showed that sum rules, for both models, are subject to only mild RG corrections (less than one degree for all the cases studied). With future high precision neutrino oscillation experiments, these results, although small, would be very important in testing the predictions of the underlying theories.

The mild RG corrections to neutrino mixing parameters, evaluated in this thesis, are mainly in the case of hierarchical neutrino masses. In general, for partially degenerate and degenerate neurtino masses, in the see-saw framework with sequential dominance, the RG corrections can be significant as discussed in[16, 89]. In the case of SM, only corrections to the neutrino mixing angles were found to be small while the running of neutrino masses can be slightly larger. For the MSSM model without sequential dominance, the RG corrections can be large especially for the case of large $\tan(\beta)$ [90].

For the case of more general charged lepton corrections, we found that most sum rules showed larger deviations at low energy due to the presence of θ_{23}^{E} with the exception of σ_1 which seemed to be insensitive to this angle. We also looked at RG running in the case of LSD with non-zero Majorana phases. We found that these phases can significantly alter the running of the TB mixing deviation parameters as well as the sum rules, particularly σ_2 [37].

Part II of this thesis concerns the study of four dimensional models originating from heterotic and type IIA string theories. In Chapter 5, we gave a brief overview of string and flux compactification. We also presented the four dimensional content of $T^6/(Z_2 \times Z_2)$ orientifold constructions which give rise to the main models considered in this part. In Chapter 6, we presented three different models: two of them were first studied by Derendinger et al. [64] and one of them by Löwen et al, [65]. We outlined the main problems that some of their solutions suffer from and suggested alternative ones which give rise to viable minima in most directions of models I and III. We also uplifted the flat directions by considering a correction to the Kähler potential.

Chapter 7 involves the study of inflation within the framework of models I and III presented in the previous chapter. After briefly reviewing the conditions of slow roll inflation, We looked at possible inflaton candidates along all the real and imaginary directions of the complex moduli. We found that the axionic directions of the moduli S, U_1, U_2, T_3 give rise to successful inflationary scenarios, for model I, with initial conditions within extended regions in parameter space. Similar results were achieved for the axionic directions in model III.

Back to the analysis of model I, we found that the case of evolving $\mathrm{Im}\, S$ and $\mathrm{Im}\, U_1$ together was quite interesting since the structure of the potential along these two directions involved a global minimum with a set of local minima displayed around it as presented in Fig.(7.7). Inflation, in this case, could be achieved for certain initial conditions where the inflaton fields roll down to the global minimum. It could be equally achieved at other sets of initial values, where the fields evolve to one of the local minima, and this may give rise to eternal inflation. We argued that this particular structure of the potential is mainly due to the way the dilaton is presented in the superpotential. For model I, the S modulus appears in the flux term as well as the gaugino condensate term as,

$$W = 2S + (U_1 T_3 - L)\mu^3 e^{-S} + \cdots , \tag{8.1}$$

It seems that this structure only appears along the axionic directions that are connected to the gaugino condensate term when evolved together with $\mathrm{Im}\, S$ (in this case we have U_1 and T_3). This clearly confirms that the property of local minima only appears in type IIA where the superpotential have similar structure to that of models I and IV. This result is very important as it suggests a background of unbounded potentials for the realisation of eternal inflation.

Appendix A

Diagonalisation of left-handed neutrino matrix

In this Appendix, we will briefly review the procedure of diagonalising the neutrino mass matrix following [40] closely. We start by writing the left-handed neutrino mass matrix as,

$$m_{LL} = \begin{pmatrix} m_{11} & m_{12} & m_{13} \\ m_{12} & m_{22} & m_{23} \\ m_{13} & m_{23} & m_{33} \end{pmatrix} \equiv \begin{pmatrix} |m_{11}|e^{i\phi_{11}} & |m_{12}|e^{i\phi_{12}} & |m_{13}|e^{i\phi_{13}} \\ |m_{12}|e^{i\phi_{12}} & |m_{22}|e^{i\phi_{22}} & |m_{23}|e^{i\phi_{23}} \\ |m_{13}|e^{i\phi_{13}} & |m_{23}|e^{i\phi_{23}} & |m_{33}|e^{i\phi_{33}} \end{pmatrix} \tag{A.1}$$

In general, we diagonalise a complex, hierarchical, neutrino matrix by following a sequence of transformations [40],

$$P_3^{\nu_L *} {R_{12}}^T P_1^{\nu_L *} R_{13}^{\nu_L T} R_{23}^{\nu_L T} P_2^{\nu_L *} m_{LL}^{\nu} P_2^{\nu_L} R_{23}^{\nu_L} R_{13}^{\nu_L} P_1^{\nu_L} R_{12}^{\nu_L} P_3^{\nu_L} = \begin{pmatrix} m_1 & 0 & 0 \\ 0 & m_2 & 0 \\ 0 & 0 & m_3 \end{pmatrix}, \tag{A.2}$$

where the resulting matrix includes the three different neutrino masses m_1, m_2 and m_3. $R_{ij},\ i,j = \{1,2,3\}$ are a set of real rotations, involving the Euler angles θ_{ij},

which can be written as,

$$R_{23} = \begin{pmatrix} 1 & 0 & 0 \\ 0 & c_{23} & s_{23} \\ 0 & -s_{23} & c_{23} \end{pmatrix} \tag{A.3}$$

$$R_{13} = \begin{pmatrix} c_{13} & 0 & s_{13} \\ 0 & 1 & 0 \\ -s_{13} & 0 & c_{13} \end{pmatrix} \tag{A.4}$$

$$R_{12} = \begin{pmatrix} c_{12} & s_{12} & 0 \\ -s_{12} & c_{12} & 0 \\ 0 & 0 & 1 \end{pmatrix}. \tag{A.5}$$

The matrices P_i in Eq.(A.2) are the phase matrices, involving the phases ϕ_2, ϕ_3, χ and ω_i, which we write as,

$$P_1 = \begin{pmatrix} 1 & 0 & 0 \\ 0 & e^{i\chi} & 0 \\ 0 & 0 & 1 \end{pmatrix} \tag{A.6}$$

$$P_2 = \begin{pmatrix} 1 & 0 & 0 \\ 0 & e^{i\phi_2} & 0 \\ 0 & 0 & e^{i\phi_3} \end{pmatrix} \tag{A.7}$$

$$P_3 = \begin{pmatrix} e^{i\omega_1} & 0 & 0 \\ 0 & e^{i\omega_2} & 0 \\ 0 & 0 & e^{i\omega_3} \end{pmatrix} \tag{A.8}$$

We briefly summarise the different steps of diagonalisation following [40]. We start by multiplying the mass matrix, given by Eq.(A.1), by the inner phase matrix $P_2^{\nu_L}$. This process modifies the phases of the matrix as follows,

$$m_{LL} = \begin{pmatrix} |m_{11}|e^{i\phi_{11}} & |m_{12}|e^{i(\phi_{12}-\phi_2)} & |m_{13}|e^{i(\phi_{13}-\phi_3)} \\ |m_{12}|e^{i(\phi_{12}-\phi_2)} & |m_{22}|e^{i(\phi_{22}-2\phi_2)} & |m_{23}|e^{i(\phi_{23}-\phi_2-\phi_3)} \\ |m_{13}|e^{i(\phi_{13}-\phi_3)} & |m_{23}|e^{i(\phi_{23}-\phi_2-\phi_3)} & |m_{33}|e^{i(\phi_{33}-2\phi_3)} \end{pmatrix} \tag{A.9}$$

After re-phasing the matrix, we proceed by applying the real rotation R_{23}, defined in Eq. (A.3). This step modifies the lower 23 block of the mass matrix by putting

zeroes in the 23, 32 elements of the matrix [40],

$$\begin{pmatrix} \tilde{m}_{22} & 0 \\ 0 & m'_3 \end{pmatrix} \equiv R_{23}^{\nu_L T} \begin{pmatrix} |m_{22}|e^{i(\phi_{22}-2\phi_2)} & |m_{23}|e^{i(\phi_{23}-\phi_2-\phi_3)} \\ |m_{23}|e^{i(\phi_{23}-\phi_2-\phi_3)} & |m_{33}|e^{i(\phi_{33}-2\phi_3)} \end{pmatrix} R_{23}^{\nu_L} \quad \text{(A.10)}$$

This diagonalisation not only modifies the masses m_{22} and m_{33} but also all the other mass entries except m_{11}. The next step, as shown in Eq.(A.2), is to apply the rotation R_{13} which diagonalises the outer 13 block. Similar to the previous step, this rotation modifies the matrix by putting zeros in the 13, 31 entries.

After applying the 13 rotation, the neutrino mass matrix can be written as,

$$R_{13}^{\nu_L T} R_{23}^{\nu_L T} P_2^{\nu_L *} m_{LL} P_2^{\nu_L} R_{23}^{\nu_L} R_{13}^{\nu_L} = \begin{pmatrix} \tilde{m}_{11} & \tilde{m}_{12} & 0 \\ \tilde{m}_{12} & \tilde{m}_{22} & 0 \\ 0 & 0 & m'_3 \end{pmatrix} \quad \text{(A.11)}$$

The last step of the diagonalisation involves modifying the upper 12 block of the matrix. To do this, we first multiply the result of the last step by $P_1^{\nu_L}$ which introduces the phase χ. We then apply the real rotation R_{12}. The neutrino mass matrix can then be written as follows,

$$R_{12}^{\nu\ T} \begin{pmatrix} \tilde{m}_{11} & \tilde{m}_{12} & 0 \\ \tilde{m}_{12} & \tilde{m}_{22} & 0 \\ 0 & 0 & m'_3 \end{pmatrix} R_{12}^{\nu} = \begin{pmatrix} m'_1 & 0 & 0 \\ 0 & m'_2 & 0 \\ 0 & 0 & m'_3 \end{pmatrix} \quad \text{(A.12)}$$

From Eq.(A.12), we can see that the neutrino matrix is successfully diagonalised, however, we still need to multiply the result by the phase matrix $P_3^{\nu_L}$ in order to make all the diagonal elements real. To proceed, we write the resulting mass matrix by substituting for the diagonal mass terms as $m'_i \equiv m_i e^{i\phi'_i},\ i = \{1, 2, 3\}$. We then apply the phase matrix and write the phases ω_i as $\omega_i = \phi'_i/2$. These phases cancel with the phases of the neutrino mass matrix which gives a real, diagonal, neutrino matrix as required.

Appendix B

Derivation of neutrino mass terms

In this Appendix, we present the derivations of the mass terms resulting from the diagonalisation of the mass matrix. After applying the rotation R_{23} A.3. We can derive expressions for the masses m_3' and $\tilde{m}_{22}$ which are necessary for deriving expressions for θ_{13} and $\tan(\theta_{12})$. To find these masses, we first take the trace of both sides of Eq.(A.10) which gives,

$$\begin{aligned} \tilde{m}_{22} + m_3' &\approx m_{22}e^{-i2\phi_2} + m_{33}e^{-i2\phi_3} \\ &\approx e^{i(2\phi_e - 2\phi_2)}\frac{|e|^2 + |f|^2}{Y}\left(1 + \epsilon_3(s_{23}^0)^2 + (c_{23}^0)^2(\epsilon_2 + \eta_1)\right), \end{aligned} \tag{B.1}$$

We can also express the determinant of both sides of Eq.(A.10). This reads,

$$\begin{aligned} \tilde{m}_{22}m_3' &= m_{22}e^{-2i\phi_2}m_{33}e^{-2i\phi_3} - (m_{23})^2e^{-2i(\phi_2+\phi_3)} \\ &= e^{-2i(\phi_2+\phi_3)}\left(\frac{c'^2}{X'}(\frac{b^2}{X} + \frac{e^2}{Y}) + \frac{(bf-ec)^2}{XY}\right) \end{aligned} \tag{B.2}$$

We take the mass term m_3' to have the following form,

$$m_3' \approx m_3'^0(1+\beta), \tag{B.3}$$

where the parameter β is given by Eq.(3.31) and the mass term $m_3'^0 \equiv m_3'|_{\epsilon_i=0,\eta_i=0}$ is given by,

$$m_3'^0 \approx e^{i(2\phi_e - 2\phi_2)}\frac{|e|^2 + |f|^2}{Y}, \tag{B.4}$$

Using Eqs.(B.1, B.2, B.4), $\tilde{m}_{22}$ can be written as,

$$\tilde{m}_{22} \approx \left(\tilde{m}^0_{22} + \eta_2 \left(\frac{b^2}{X} + \frac{e^2}{Y}\right)\right)(1-\beta), \tag{B.5}$$

where

$$\tilde{m}^0_{22} \equiv \tilde{m}_{22}|_{c'=0,\epsilon_i=0} \approx e^{-2i\phi_2}\frac{(bc^0_{23} - cs^0_{23}e^{i(\phi_e-\phi_f)})^2}{X}, \tag{B.6}$$

and the parameter η_2 is given by Eq.(3.40).

In addition to the derivation of the masses $\tilde{m}_{22}, m'_3$, applying the rotation R_{23}, modifies the masses m_{12}, m_{13}. These become $\tilde{m}_{12}, \tilde{m}_{13}$, after diagonalising the 23 block, and can be derived to leading order as follows

$$\begin{aligned}
\tilde{m}_{12} &= c_{23}m_{12}e^{-i\phi_2} - s_{23}m_{13}e^{-i\phi_3}, \\
&\approx \tilde{m}^0_{12}(1-\gamma(s^0_{23})^2) - e^{-i\phi_3}\gamma s^0_{23}(\frac{ac}{X} + \frac{df}{Y}),
\end{aligned} \tag{B.7}$$

$$\begin{aligned}
\tilde{m}_{13} &= s_{23}m_{12}e^{-i\phi_2} + c_{23}m_{13}e^{-i\phi_3} \\
&\approx \tilde{m}^0_{13}(1-\gamma(s^0_{23})^2) + e^{-i\phi_2}\gamma s^0_{23}(\frac{ab}{X} + \frac{de}{Y}),
\end{aligned} \tag{B.8}$$

where the parameter γ is given by Eq.(3.28), the masses $\tilde{m}^0_{12} \equiv \tilde{m}_{12}|_{c'=0,\epsilon_i=0}$ and $\tilde{m}^0_{13} \equiv \tilde{m}_{13}|_{c'=0,\epsilon_i=0}$ are given to leading order, as presented in [40], by

$$\tilde{m}^0_{12} \approx e^{-i\phi_2}\frac{a(c^0_{23}b - s^0_{23}ce^{i(\phi_e-\phi_f)})}{X}, \tag{B.9}$$

$$\tilde{m}^0_{13} \approx e^{-i\phi_2}\left(\frac{a}{X}(s^0_{23}b + c^0_{23}ce^{i(\phi_e-\phi_f)}) + e^{i\phi_e}\frac{d\sqrt{|e|^2+|f|^2}}{Y}\right). \tag{B.10}$$

After applying the R_{13} rotation, we obtain another mass term, $\tilde{m}_{11}$, which can be presented to leading order as

$$\begin{aligned}
\tilde{m}_{11} &\approx m_{11} - \frac{\tilde{m}^2_{13}}{m'_3} \\
&\approx \tilde{m}^0_{11}(1-2\gamma(s^0_{23})^2 - \beta) + \frac{a^2}{X}(2\gamma(s^0_{23})^2 + \beta) + \frac{d^2}{Y}(2\gamma(s^0_{23})^2 + \beta) \\
&- 2e^{-2i\phi_e}\epsilon_6(s^0_{23}b + c^0_{23}ce^{i(\phi_e-\phi_f)})\gamma s^0_{23}\left(\frac{ab}{X} + \frac{de}{Y}\right)
\end{aligned} \tag{B.11}$$

where the leading order form of $\tilde{m}^0_{11} \equiv \tilde{m}_{11}|_{\eta_i=0,\epsilon_i=0}$ is given in [40],

$$m^0_{11} \approx \frac{a^2}{X} - e^{-i\phi_e}\frac{2d}{\sqrt{|e|^2+|f|^2}}\frac{a(s^0_{23}b + c^0_{23}ce^{i(\phi_e-\phi_f)})}{X}, \tag{B.12}$$

The small parameter ϵ_6 is written as,

$$\epsilon_6 = \frac{a}{X}\left(\frac{|e|^2+|f|^2}{Y}\right)^{-1}.$$

Similar to the derivation of the masses $\tilde{m}_{22}, m'_3$, the neutrino masses m'_1 and m'_2 can be written using the trace and the determinant of the upper 12 block of Eq.(A.12). The real neutrino masses m_1, m_2 can then be written, in the SD cases, as

$$m_1 \approx \frac{|c'|^2}{6X'}\left(1 - \frac{Y}{X}\frac{|b|^2}{|e|^2} + \frac{2|d|}{|e|}\right)v_u^2, \tag{B.13}$$

$$m_2 \approx \left(\frac{3|b|^2}{X} + \frac{|c'|^2}{3X'}\left(1 - \frac{Y}{X}\frac{|b|^2}{|e|^2} - \frac{|d|}{|e|}\right)\cos(2\phi_{c'})\right)v_u^2, \tag{B.14}$$

The neutrino mass m_3 can be written in the SD cases, using Eqs.(B.3, B.4), as

$$m_3 \approx \left(\frac{2|e|^2}{Y} + \frac{|c'|^2}{X'}\cos(2\phi_{c'})\right)v_u^2. \tag{B.15}$$

Appendix C

Derivation of Hessian Matrices

Here, we write the derivation of the Hessian matrices for models I, III, presented in Chapter 6. The Hessian matrix for these models is a matrix of the second partial derivatives of the potential V in terms of the real fields.

As discussed in the previous chapters, model I consists of seven complex fields $(S, T_1, T_2, T_3, U_1, U_2, U_3)$, which means that there is a total of 14 real fields: the real parts, $s, t_1, t_2, t_3,\ u_1, u_2, u_3$ and the imaginary parts: $s_i, t_{1i}, t_{2i}, t_{3i}, u_{1i}, u_{2i}, u_{3i}$. The Hessian matrix in this case is a 14×14 matrix written as,

$$H = \begin{pmatrix} \frac{\partial^2 V}{\partial s^2} & \frac{\partial^2 V}{\partial s \partial t_1} & \cdots & \frac{\partial^2 V}{\partial s \partial u_{3i}} \\ \frac{\partial^2 V}{\partial t_1 \partial s} & \frac{\partial^2 V}{\partial t_1^2} & \cdots & \frac{\partial^2 V}{\partial t_1 \partial u_{3i}} \\ \vdots & \vdots & \ddots & \vdots \\ \frac{\partial^2 V}{\partial u_{3i} \partial s} & \frac{\partial^2 V}{\partial u_{3i} \partial t_1} & \cdots & \frac{\partial^2 V}{\partial u_{3i}^2} \end{pmatrix} \tag{C.1}$$

By calculating the Hessian, we can determine the type of a particular critical point. This critical point is a minimum only if all the eigenvalues of the Hessian matrix, evaluated at this point, are non-zero and positive. For model I, after uplifting, the extremum was found at the following values of the real fields,

$$\begin{aligned} &s = 1.618,\ t_1 = 1,\ t_2 = 1,\ t_3 = 2,\ u_1 = 2,\ u_2 = 0.763,\ u_3 = 0.5, \\ &s_i = -\pi/2,\ t_{1i} = 3.295,\ t_{2i} = 1,\ t_{3i} = 0,\ u_{1i} = 0,\ u_{2i} = \pi,\ u_{3i} = 0, \end{aligned} \tag{C.2}$$

Evaluating the eigenvalues of the Hessian, given by Eq.(C.1), we find the following values,

$$\begin{aligned} &5.986,\ 5.448,\ 0.81,\ 0.559,\ 0.254,\ 0.194,\ 0.155,\\ &0.155,\ 0.133,\ 0.086,\ 0.083,\ 0.077,\ 0.077,\ 0.045. \end{aligned} \tag{C.3}$$

All these values are positive which proves that the extremum found in Chapter 6 is indeed a minimum.

To prove that the extremum found for model III is a minimum, the same procedure can be followed and the Hessian can be written as shown in Eq.(C.1). In this case, however, we only have five complex fields (S, T_1, T_2, T_3, U). This means that we can write the Hessian in terms of ten real fields: $s, t_1, t_2, t_3, u, s_i, t_{1i}, t_{2i}, t_{3i}, u_i$. The extremum is presented in Chapter I and corresponds to the following values,

$$\begin{aligned} &s = 1.25,\ t_1 = 1,\ t_2 = 1,\ t_3 = 1,\ u = 0.747,\\ &s_i = -\pi/2,\ t_{1i} = 1.314,\ t_{2i} = 1,\ t_{3i} = 0,\ u_i = 0. \end{aligned} \tag{C.4}$$

The eigenvalues evaluated for this model are also found to be all non-zero and positive,

$$\begin{aligned} &116.314,\ 115.257,\ 57.173,\ 56.156,\ 3.551,\\ &0.984,\ 0.617,\ 0.617,\ 0.617,\ 0.617. \end{aligned} \tag{C.5}$$

Bibliography

[1] J. N. Bahcall, arXiv:physics/0406040.

[2] Y. Fukuda *et al.* [Super-Kamiokande Collaboration], Phys. Rev. Lett. **81**, 1562 (1998).

[3] K. Eguchi *et al.* [KamLAND Collaboration], Phys. Rev. Lett. **90** (2003) 021802 [arXiv:hep-ex/0212021].

[4] M. H. Ahn *et al.* [K2K Collaboration], Phys. Rev. D **74** (2006) 072003 [arXiv:hep-ex/0606032].

[5] P. F. Harrison, D. H. Perkins and W. G. Scott, Phys. Lett. B **530** (2002) 167 [arXiv:hep-ph/0202074];

[6] P. F. Harrison and W. G. Scott, Phys. Lett. B **557** (2003) 76 [arXiv:hep-ph/0302025]; see also

[7] S. F. King, JHEP **0508** (2005) 105 [arXiv:hep-ph/0506297].

[8] S. F. King and M. Malinsky, Phys. Lett. B **645** (2007) 351 [arXiv:hep-ph/0610250];

[9] P. H. Frampton, S. T. Petcov and W. Rodejohann, Nucl. Phys. B **687** (2004) 31 [arXiv:hep-ph/0401206];

[10] I. de Medeiros Varzielas and G. G. Ross, Nucl. Phys. B **733** (2006) 31 [arXiv:hep-ph/0507176];

[11] G. Altarelli and F. Feruglio, Nucl. Phys. B **741** (2006) 215 [arXiv:hep-ph/0512103];

[12] G. L. Fogli, E. Lisi, A. Marrone, A. Palazzo and A. M. Rotunno, arXiv:0905.3549 [hep-ph].

[13] V. F. Mukhanov, JETP Lett. **41**, 493 (1985).

[14] A. A. Starobinsky, Phys. Lett. B **117**, 175 (1982).

[15] E. Komatsu *et al.* [WMAP Collaboration], Astrophys. J. Suppl. **180** (2009) 330 [arXiv:0803.0547 [astro-ph]].

[16] S. Antusch, J. Kersten, M. Lindner, M. Ratz and M. A. Schmidt, JHEP **0503** (2005) 024 [arXiv:hep-ph/0501272].

[17] S. F. King, Rept. Prog. Phys. **67** (2004) 107 [arXiv:hep-ph/0310204].

[18] R. N. Mohapatra, arXiv:hep-ph/0306016.

[19] R. N. Mohapatra *et al.*, Rept. Prog. Phys. **70** (2007) 1757 [arXiv:hep-ph/0510213].

[20] R. N. Mohapatra and A. Y. Smirnov, Ann. Rev. Nucl. Part. Sci. **56** (2006) 569 [arXiv:hep-ph/0603118].

[21] S. F. King, arXiv:0712.1750 [hep-ph].

[22] M. E. Peskin and D. V. Schroeder, "An Introduction to Quantum Field Theory ,". Reading, USA: Addison-Wesley (1995).

[23] T. Yanagida in *Proc. of the Workshop on Unified Theory and Baryon Number of the Universe*, KEK, Japan, 1979; S.L.Glashow, Cargese Lectures (1979); M. Gell-Mann, P. Ramond and R. Slansky in Sanibel Talk, CALT-68-709, Feb 1979, and in *Supergravity* (North Holland, Amsterdam 1979);

[24] G. Lazarides, Q. Shafi and C. Wetterich, Nucl. Phys. B **181** (1981) 287.

[25] J. Maricic and J. G. Learned, Contemp. Phys. **46** (2005)

[26] M. Maltoni, T. Schwetz, M. A. Tortola and J. W. F. Valle, New J. Phys. **6** (2004) 122 [arXiv:hep-ph/0405172].

[27] T. Schwetz, AIP Conf. Proc. **981** (2008) 8 [arXiv:0710.5027 [hep-ph]].

[28] M. Maltoni, T. Schwetz, M. A. Tortola and J. W. F. Valle, Phys. Rev. D **68** (2003) 113010 [arXiv:hep-ph/0309130].

[29] S. F. King, Phys. Lett. B **659** (2008) 244 [arXiv:0710.0530 [hep-ph]].

[30] E. Ma and G. Rajasekaran, Phys. Rev. D **64** (2001) 113012 [arXiv:hep-ph/0106291].

[31] Z. z. Xing, Phys. Lett. B **533** (2002) 85 [arXiv:hep-ph/0204049].

[32] G. Altarelli, F. Feruglio and I. Masina, Nucl. Phys. B **689** (2004) 157, hep-ph/0402155;

[33] S. Antusch and S. F. King, Phys. Lett. B **591** (2004) 104, [arXiv:hep-ph/0403053].

[34] S. Antusch and S. F. King, Phys. Lett. B **659** (2008) 640 [arXiv:0709.0666 [hep-ph]].

[35] S. Antusch and S. F. King, Phys. Lett. B **631** (2005) 42 [arXiv:hep-ph/0508044];

[36] S. Antusch, P. Huber, S. F. King and T. Schwetz, JHEP **0704** (2007) 060 [arXiv:hep-ph/0702286].

[37] S. Antusch, S. F. King and M. Malinsky, arXiv:0711.4727 [hep-ph];

[38] S. Antusch, S. F. King and M. Malinsky, JHEP **0805** (2008) 066 [arXiv:0712.3759 [hep-ph]].

[39] S. Antusch, S. Boudjemaa and S. F. King, "Neutrino Mixing Angles in Sequential Dominance to NLO and NNLO."

[40] S. F. King, JHEP **0209** (2002) 011 [arXiv:hep-ph/0204360].

[41] S. F. King, Phys. Rev. D **67** (2003) 113010 [arXiv:hep-ph/0211228].

[42] S. F. King, Phys. Lett. B **439** (1998) 350 [arXiv:hep-ph/9806440];

[43] S. Antusch and S. F. King, New J. Phys. **6** (2004) 110 [arXiv:hep-ph/0405272];

[44] S. F. King, arXiv:0903.3199 [hep-ph].

[45] S. Boudjemaa and S. F. King, Phys. Rev. D **79** (2009) 033001 [arXiv:0808.2782 [hep-ph]].

[46] S. Antusch, J. Kersten, M. Lindner and M. Ratz, Phys. Lett. B **544** (2002) 1 [arXiv:hep-ph/0206078].

[47] G. L. Fogli, E. Lisi, A. Marrone, A. Palazzo and A. M. Rotunno, arXiv:0809.2936 [hep-ph].

[48] A. Grozin, arXiv:hep-ph/0508242.

[49] S. Antusch, P. Huber, J. Kersten, T. Schwetz, W. Winter [arXiv:hep-ph/0404268].

[50] A. Bandyopadhyay *et al.* [ISS Physics Working Group], arXiv:0710.4947 [hep-ph].

[51] B. R. Greene, arXiv:hep-th/9702155.

[52] E. Silverstein, arXiv:hep-th/0405068.

[53] M. Grana, Phys. Rept. **423** (2006) 91 [arXiv:hep-th/0509003].

[54] M. R. Douglas and S. Kachru, Rev. Mod. Phys. **79** (2007) 733 [arXiv:hep-th/0610102].

[55] R. Blumenhagen, B. Kors, D. Lust and S. Stieberger, Phys. Rept. **445** (2007) 1 [arXiv:hep-th/0610327].

[56] J. Polchinski, "String theory. Vol. 1: An introduction to the bosonic string, Vol. 2: Superstring Theory and Beyond,". Cambridge, UK: Univ. Pr. (1998) 402.

[57] C. P. Bachas, "Lectures on D-branes," arXiv:hep-th/9806199.

[58] J. Polchinski, "Lectures on D-branes," arXiv:hep-th/9611050.

[59] T. Kaluza, Sitzungsber. Preuss. Akad. Wiss. Berlin (Math. Phys.) **1921** (1921) 966.

[60] O. Klein, Z. Phys. **37** (1926) 895 [Surveys High Energ. Phys. **5** (1986) 241].

[61] L. Susskind, "The anthropic landscape of string theory," arXiv:hep-th/0302219.

[62] J.-P. Derendinger, C. Kounnas, P. M. Petropoulos, and F. Zwirner, *Nucl. Phys.* **B715** (2005) 211–233, `arXiv:hep-th/0411276`.

[63] J. P. Derendinger, C. Kounnas, P. M. Petropoulos, and F. Zwirner, *Fortsch. Phys.* **53** (2005) 926–935, `arXiv:hep-th/0503229`.

[64] J. P. Derendinger, C. Kounnas and P. M. Petropoulos, "Gaugino condensates and fluxes in N = 1 effective superpotentials," Nucl. Phys. B **747** (2006) 190 [arXiv:hep-th/0601005].

[65] V. Lowen, H. P. Nilles and A. Zanzi, arXiv:0804.3913 [hep-th].

[66] E. Cremmer, S. Ferrara, C. Kounnas, and D. V. Nanopoulos, *Phys. Lett.* **B133** (1983) 61.

[67] J. R. Ellis, C. Kounnas, and D. V. Nanopoulos, "No Scale Supersymmetric Guts," *Nucl. Phys.* **B247** (1984) 373–395.

[68] A. Linde, Cosmology," [arXiv:hep-th/0503203].

[69] E. W. Kolb and M. S. Turner, "The Early Universe."

[70] A. R. Liddle and D. H. Lyth, " Cosmological Inflation and Large-Scale Structure."

[71] F. Quevedo, Class. Quant. Grav. **19** (2002) 5721 [arXiv:hep-th/0210292].

[72] G. R. Dvali and S. H. H. Tye, Phys. Lett. B **450** (1999) 72 [arXiv:hep-ph/9812483].

[73] J. J. Blanco-Pillado *et al.*, JHEP **0411** (2004) 063 [arXiv:hep-th/0406230].

[74] Z. Lalak, G. G. Ross and S. Sarkar, Nucl. Phys. B **766** (2007) 1 [arXiv:hep-th/0503178].

[75] J. J. Blanco-Pillado *et al.*, JHEP **0609** (2006) 002 [arXiv:hep-th/0603129].

[76] J. P. Conlon and F. Quevedo, JHEP **0601** (2006) 146 [arXiv:hep-th/0509012].

[77] A. Vilenkin, Phys. Rev. D **27** (1983) 2848.

[78] A. Vilenkin, Phys. Rev. Lett. **72** (1994) 3137 [arXiv:hep-th/9402085].

[79] A. D. Linde, Phys. Lett. B **327** (1994) 208 [arXiv:astro-ph/9402031].

[80] T. Barreiro, B. de Carlos, E. Copeland and N. J. Nunes, Phys. Rev. D **72** (2005) 106004 [arXiv:hep-ph/0506045].

[81] D. Baumann and L. McAllister, Ann. Rev. Nucl. Part. Sci. **59** (2009) 67 [arXiv:0901.0265 [hep-th]].

[82] L. McAllister, E. Silverstein and A. Westphal, arXiv:0808.0706 [hep-th].

[83] S. R. Coleman and F. De Luccia, Phys. Rev. D **21**, 3305 (1980).

[84] S. W. Hawking and I. G. Moss, Phys. Lett. B **110**, 35 (1982).

[85] A. A. Starobinsky, "STOCHASTIC DE SITTER (INFLATIONARY) STAGE IN THE EARLY UNIVERSE."

[86] A. A. Starobinsky and J. Yokoyama, Phys. Rev. D **50**, 6357 (1994) [arXiv:astro-ph/9407016].

[87] J. J. Blanco-Pillado, D. Schwartz-Perlov and A. Vilenkin, arXiv:0904.3106 [hep-th].

[88] S. Kachru, R. Kallosh, A. D. Linde and S. P. Trivedi, Phys. Rev. D **68** (2003) 046005 [arXiv:hep-th/0301240].

[89] S. Antusch and S. F. King, Nucl. Phys. B **705** (2005) 239 [arXiv:hep-ph/0402121].

[90] S. Antusch, J. Kersten, M. Lindner and M. Ratz, Nucl. Phys. B **674** (2003) 401 [arXiv:hep-ph/0305273].